Direct visualisation of nucleation in colloidal model systems

Lars Kürten

PSL UNIVERSITÉ PARIS

THÈSE DE DOCTORAT
DE L'UNIVERSITÉ PSL

Préparée à l'ESPCI Paris – Gulliver Laboratory

Direct visualisation of nucleation in colloidal model systems

Visualisation directe de la nucléation dans des systèmes modèles colloïdaux

Soutenue par
Lars KÜRTEN
Le 07 janvier 2026

École doctorale n° 564
Physique en Île-de-France

Spécialité
Physique

Composition du jury :

Giulio, BIROLI	Professeur, ENS - PSL	*Président*
Thomas, PALBERG	Professeur, Johannes Gutenberg University	*Rapporteur*
Emanuela, ZACCARELLI	Professeure, La Sapienza University	*Rapporteuse*
Luca, CIPELLETTI	Professeur, University of Montpellier	*Examinateur*
David, RICHARD	CR, PMMH ESPCI - PSL	*Examinateur*
Rocio, SEMINO	Maître de conférences, Sorbonne University	*Examinatrice*
Stefano, AIME	Maître de conférences, C3M ESPCI - PSL	*Examinateur*
C. Patrick, ROYALL	DR, Gulliver ESPCI - PSL	*Directeur de thèse*

ESPCI PARIS | PSL

Abstract French

Comprendre la nucléation des cristaux est d'une importance profonde tant pour des raisons fondamentales que technologiques. Dans le matériau le plus simple connu pour s'auto-assembler afin de former un cristal, les sphères dures, les prédictions les plus avancées et les mesures expérimentales des taux de nucléation diffèrent de plus de dix ordres de grandeur. En plus de remettre en question notre compréhension de la cristallisation, cela complique les tentatives d'utiliser l'auto-assemblage pour réaliser de nouveaux matériaux. Nous proposons ici une approche combinant expérience et simulation informatique pour relever les défis liés à la nucléation et à la réalisation de structures cristallines dans les colloïdes. Nous abordons la divergence de nucléation grâce à deux développements, basés sur des études en espace réel de colloïdes par microscopie confocale.

Premièrement, nous considérons la barrière de nucléation en mesurant l'énergie libre de formation des noyaux pré-critiques, dont la fréquence d'apparition est suffisamment élevée pour être accessible expérimentalement grâce à la microscopie confocale. Deuxièmement, nous visons à cartographier les points d'état entre expérience et simulation avec une précision jusqu'ici inégalée. Pour ce faire, nous améliorons le suivi des particules avec des méthodes récemment développées intégrant l'apprentissage automatique et utilisons des fonctions de corrélation d'ordre supérieur, plus sensibles à la fraction volumique que les fonctions de corrélation par paires. Avec notre méthode, les barrières de nucléation présentent un accord raisonnable, ce qui conduit à la disparition de la divergence. De plus, à partir des données de microscopie confocale de prélèvements en sédimentation, nous avons constaté que les échelles de temps concurrentes de la sédimentation et de la cristallisation dans les expériences basées sur la méthode de Paulin-Ackerson, couramment utilisée pour déterminer le point d'état dans les expériences de diffusion de la lumière, pourraient conduire à une surestimation systématique de la fraction volumique et donc à l'apparition de la divergence.

Enfin, nous étudions la nucléation cristalline dans un autre système modèle, les colloïdes dipolaires, dans lesquels les interactions dipolaires sont induites par un champ électrique externe. Le champ

électrique peut être utilisé pour ajuster facilement l'intensité de l'interaction dipolaire, permettant l'étude de la sélection polymorphe et de la règle des étapes d'Ostwald. Ce qui est particulièrement intéressant ici est la formation d'un cristal métastable hexagonal compact (HCP). Celui-ci fond ensuite, après quoi un cristal BCT (la phase stable) se forme. Les mécanismes sous-jacents et la connexion avec la structure du fluide sont en cours d'investigation.

De plus, les possibilités d'optimisation de la nucléation cristalline dans les systèmes dipolaires sont analysées en appliquant différents protocoles pour l'intensité de l'interaction dipolaire. Nous constatons que certains protocoles favorisent un assemblage plus rapide de domaines cristallins plus larges.

Abstract English

Understanding crystal nucleation is of profound importance for both fundamental and technological reasons. In the simplest known material that self-assembles to form a crystal—hard spheres—the most advanced predictions and experimental measurements of nucleation rates differ by more than ten orders of magnitude. In addition to challenging our understanding of crystallization, this complicates efforts to use self-assembly to create new materials.

Here, we propose an approach combining experiment and computer simulation to address the challenges related to nucleation and the formation of crystalline structures in colloids. We address the nucleation discrepancy through two developments, based on real-space studies of colloids using confocal microscopy.

First, we consider the nucleation barrier by measuring the free energy of formation of pre-critical nuclei, whose occurrence frequency is high enough to be experimentally accessible using confocal microscopy. Second, we aim to map state points between experiment and simulation with previously unmatched precision. To do this, we improve particle tracking using recently developed methods integrating machine learning, and we employ higher-order correlation functions, which are more sensitive to volume fraction than pair correlation functions. With our method, the nucleation barriers show reasonable agreement, leading to the disappearance of the discrepancy. Moreover, from confocal microscopy data of sedimenting samples, we found that the competing time scales of sedimentation and crystallization in experiments based on the Paulin-Ackerson method-commonly used to determine the state point in light scattering experiments-could lead to a systematic overestimation of the volume fraction, and thus to the appearance of the discrepancy.

Finally, we study crystal nucleation in another model system: dipolar colloids, in which dipolar interactions are induced by an external electric field. The electric field can be used to easily tune the strength of the dipolar interaction, allowing the study of polymorph selection and Ostwald's

step rule. Particularly interesting here is the formation of a metastable hexagonal close-packed (HCP) crystal. This then melts, after which a BCT (the stable phase) crystal forms. The underlying mechanisms and the connection with the structure of the fluid are currently under investigation.

Additionally, the possibilities for optimizing crystal nucleation in dipolar systems are analysed by applying different protocols for the dipolar interaction strength. We find that certain protocols promote faster assembly of larger crystalline domains.

Acknowledgments

First and foremost, I would like to express my heartfelt gratitude to my supervisor, Paddy Royall, for giving me the opportunity to work on this project. I feel extremely fortunate to have learned so much under his guidance over the past three years. I am deeply grateful for his patience, support, and the many opportunities that have allowed me to grow, both scientifically and personally.

I would also like to thank Paddy Royall's group in Bristol, who supported me especially at the beginning of my project and taught me the foundations of my experimental work. Special thanks go to Rui Cheng for introducing me to confocal microscopy and sample preparation, Yushi Yang, Abdelwahab Kawafi, and Abraham Mauleon Amieva for their help with particle tracking, and Katherine Skipper for her assistance with the dipolar samples. Your advice and support made all the initial challenges much easier to overcome.

My sincere thanks also go to all the members of the Gulliver Laboratory. I have always found a sympathetic ear and received invaluable support during every phase of my project. Special thanks to Justine Laurent, who was always ready to help with experimental questions, and to Fée Sorrentino, for solving every problem that arose—or that I created myself—especially when navigating the complexities of the French system.

This project was carried out in close collaboration with Frank Smallenburg and Antoine Castagnède, and I would like to thank both of them for their tremendous support over the last three years. Through our close collaboration and the simulated data they provided, I was able to gain new insights into my experiments. Antoine, in particular, was an immense support during the more difficult and complicated phases of this work.

Many of the confocal microscopy measurements were carried out at the IPGG, and I would like to take this opportunity to thank Bertrand Cinquin and Taha Messlmani for their support during the

experiments and for their help in synthesising the Janus particles.

It has been a pleasure to discuss the challenges of the hard-sphere nucleation problem with Marjolein Dijkstra, Daan Frenkel, Peter Harrowell, Laura Filion, John Russo, and Thomas Speck. Their insights and perspectives have been truly inspiring and have greatly enriched my understanding of the topic. The author gratefully acknowledges the Agence Nationale de la Recherche grant DiViNew for financial support.

Beyond the many great experiences and joyful moments of successful experiments, there were also times when progress felt slow and challenges seemed insurmountable. In those moments, I could always count on my friends. Thank you for your visits, distractions, conversations, advice and simply being there. Your support made everything possible.

I am also deeply grateful to my parents and my sister for their love and encouragement—not only during the past three years but throughout my life. Their unconditional support has made it possible for me to pursue this path, and for that, I will always be thankful.

Finally, Sinje. Words cannot fully express my gratitude, so I will keep it short. The past few years would have been unthinkable without you. I am forever grateful to have you by my side. This has truly been a journey in every sense of the word, and without you, I would not have made it this far.

Contents

List of Figures

List of Symbols and Abbreviations

σ	hard-sphere diameter
σ_{eff}	effective diameter
ϕ	volume fraction
ϕ_{eff}	effective volume fraction
ρ	number density
P	pressure
η	solvent viscosity
β	$1/k_BT$
$u(r)$	pair interaction potential
κ	Debye length
D	diffusion coefficient
J	nucleation rate
ξ_g	gravitational length
Pe	Péclet number
v	velocity
$g(r)$	radial distribution function
s	polydispersity
TCC	topological cluster classification: identifies higher-order structures
PMMA	polymethyl methacrylate: the most commonly used experimental system for 3D hard spheres
PRS	particle-resolved studies
PHSA	polyhydroxystearic acid
ICEP	induced-charge electrophoresis

Chapter 1

Introduction

1.1 Objective and Thesis Outline

The overall goal of this work is to better understand the underlying mechanisms of nucleation and crystallisation processes. Although crystallisation surrounds us in our everyday lives, playing a fundamental role in many industrial processes, like cosmetic production, food production, and even contributing to huge inaccuracies in climate change predictions [1, 2], reliable predictions of this phenomenon remain an interdisciplinary challenge to this day. It is abundantly clear that there is widespread interest in gaining a deep understanding of crystallisation for a wide variety of systems [3]. This raises a key question: Why is it so difficult to study this phenomenon?

The question can be partially answered by considering a fundamental mechanism of crystallisation, nucleation. Probably the best-known phase transition is the freezing of water into ice. Everyone knows the phase boundary of this system, the only temperature at which water and ice are both stable, 0°C, at atmospheric pressure. Interestingly, ice melts immediately when heated above this temperature. In the opposite case, however, the situation is more difficult. Water can be cooled below 0°C without immediately crystallising. This phenomenon is called supercooling [4, 5]. In this state, minimal influences, such as mechanical stress or contact with the stable ice phase, can immediately trigger the freezing process. In other words, it seems as if some kind of barrier has to be overcome in order for the phase transition to begin. The spontaneous formation of a piece of ice in a supercooled water system is an example of nucleation. The time scale on which homogeneous nucleation occurs is determined by the nucleation rate. Now it becomes more obvious

what difficulties are involved in investigating nucleation and predicting nucleation rates: Nucleation is a rare event, microscopic on the time and length scale. In other words, for an experimentalist, this means that the crystallisation process can take place anywhere and at any time in the sample, making it very difficult to observe [6].

Furthermore, experimental measurements of homogeneous nucleation rates in water, for example, may be biased by limited size effects or effects of pressure [7, 8]. However, studies using computer simulations also fail to find good agreement. There are discrepancies between and among different methods used [9, 10], or due to inaccurate thermodynamic properties [11], and machine learning methods that can only determine phase boundaries with limited accuracy [12–14]. Of course, water as a molecular system is a particularly difficult example. Modelling the interactions between components is not straightforward, which leads to inaccuracies and inconsistencies.

So what is the situation for simpler systems, such as colloids, which are widely used in experiments and computer simulations due to their simple and classic interactions? The dominant time scale, due to their mesoscopic size, is much larger than that of atomic or molecular systems [15, 16], which makes the nucleation mechanisms easier to investigate and even allows particle-resolved studies, which are able to shed light on underlying processes [17–19]. Unfortunately, from the perspective of quantitative agreement, it does not look much better here. In the system of colloidal hard spheres, the simplest and most studied model system, there is a large discrepancy (Fig. 1.1) between experimentally measured nucleation rates and those from computer simulations [16, 20–22]. In the past, various approaches have been taken to resolve the discrepancy, essentially by attempting to mimic experimental properties, such as polydispersity [23, 24] or electrostatic [24] and hydrodynamic [25] interactions, in simulations. In addition, the influence of heterogeneous nucleation [26], sedimentation [27] and the role of nucleation and crystal growth in the experiments [28] was taken into account. However, it turns out that these approaches cannot explain the discrepancy or can only explain it in part.

Since the discrepancy can be seen for light scattering experiments and computer simulations, we will conduct new experiments using confocal microscopy and compare the free-energy of the formation of precritical nuclei from particle-resolved data with large-scale computer simulations. After very precise mapping of the experimental state point onto the computer simulations, we find good agreement, which leads to the disappearance of the discrepancy [41], but raises the question of whether there may be a systematic uncertainty in the measurement of the effective state point for the samples used for light scattering measurements.

Until recently [42], accurate determination of the state points for colloidal experiments was very

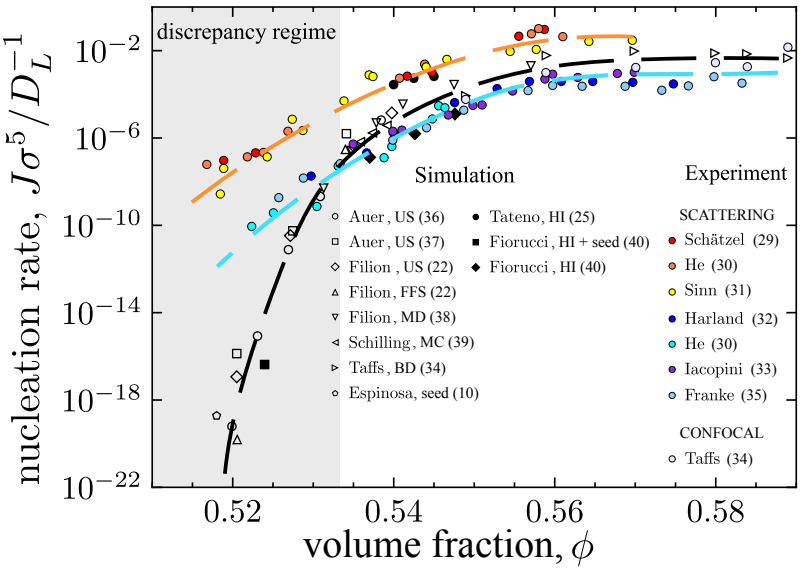

Figure 1.1: Reduced nucleation rates from experiments [29–35] and computer simulations[10, 22, 25, 34, 36–40].

difficult [23, 24]. However, even after the improvements made in recent years, using colloidal systems, compared to atomic systems in which, for example, the temperature can be determined with the highest accuracy, comes with a certain degree of uncertainty in the state point due to the finite sample size and the limited accuracy of weighing the components during sample preparation[16, 23]. In the light scattering experiments, the Paulin-Ackerson method, based on the phase behaviour of sedimenting systems, is mainly used to determine the state point and phase boundaries [43]. In this approach, however, the time scales of nucleation, phase separation and sedimentation compete, which can influence the calculation of the state point. We were able to quantify this influence and determine the bias that causes the discrepancy in comparing the nucleation rates.

In the world of colloidal systems, there are also more exotic models than hard spheres, for example with anisotropic interactions. One example are particles with dipole-dipole interactions induced by an external electric field [44–46]. Here, the direction of the dipole moment is constantly parallel to the electric field, in contrast to ferromagnetic particles, for example, which can be described using the Stockmayer model and in which the direction of the dipole moment follows the orientation of the particles [47]. Systems with dipolar interactions caused by an external electric field have attracted increasing interest. Their phase behaviour has been studied extensively in experiments [48–50] and computer simulations [51]. This model is particularly interesting because the interactions are tunable at will and because of the variety of crystal structures it self-assembles into [45, 51]. This makes the system particularly suitable for investigating multistage crystallisation processes and polymorph selection, in which a system can nucleate into different crystal structures [52]. We will

discuss an experiment in which dipolar colloids are used for direct observation of Ostwald's rule of stages, i.e. the phenomenon whereby a system does not crystallise directly into the most stable phase, but rather through a sequence of phases with increasingly lower free energy [53].

Furthermore, by tuning the interaction strength crystallisation is reversible for systems of dipolar colloids, which raises the question of optimisation. Can the self-assembly process be controlled and optimized by adjusting the interactions over time to achieve large crystal domains? A similar question has already been answered using computer simulations with a slightly different system, whereby a compromise was found between forcing the system to crystallise and the annealing of defects in the structure [54–56]. We will analyse various protocols in terms of interaction strength and attempt to optimise the self-assembly process towards the formation of larger crystal domains.

The final model system to be discussed is active colloids, in which energy is consumed at the level of the constituents [57–61]. They fall under the general term of active matter [60, 62, 63], for which there are numerous examples in nature, like bacterial colonies [64, 65], cell tissues [66, 67] or flocks of animals [68]. In the case of self-propelled Janus particles with dipolar interaction, which we will also investigate in this thesis, the diverse phase behaviour appears to be dominated by a compromise between activity, interaction strength and crowding effects [62, 69]. We want to improve the synthesis of these three-dimensional active colloids and characterise the activity of the particles.

This first part of the thesis serves as an introduction to the wide-ranging issues addressed by the investigation of the fundamental processes of nucleation. This thesis aims to make a significant contribution to answering these open questions and is structured as follows.

- **Chapter 1** We begin with explaining the role of colloidal systems in the world of soft matter, both as relevant material for industry and as model systems for fundamental physics. We discuss advantages such as their mesoscopic size, which makes them visible for optical microscopy, and their classical nature, which makes them easily accessible for computer simulations. Next, we introduce the three colloidal model systems that are the subject of this thesis. First, we explain what is perhaps the simplest and most studied colloidal system, that of hard spheres, paying particular attention to the interactions in real systems, the equilibrium phase diagram, and the influence of polydispersity on it. This is followed by a description of dipolar colloids and their phase behaviour, before explaining active colloids in 3D with dipolar interactions. Finally, we address nucleation as the overarching theme of this

thesis. We introduce the theoretical framework for classical nucleation theory, followed by an explanation of heterogeneous nucleation, which can play an important role, especially in experimental systems.

- **Chapter 2** This chapter provides an overview of the methods used. Both the hard spheres and the dipolar colloids are systems of PMMA particles dispersed in a solvent mixture with matched density and refractive index. Here we explain protocols for preparing these samples, which serve as the basis for creating systems with arbitrary state points. From this basis, sedimenting samples can also be created, whose mixture can be systematically adjusted to achieve different degrees of sedimentation. This is followed by a description of how confocal microscopy works and how particle coordinates can be extracted from the experimental images. We explain various computer simulation techniques and how the structural properties of experimental and simulation data can be analysed. In doing so, we discuss the widely used radial distribution function and how we can identify higher-order clusters. Finally, we briefly describe how nucleation rates can be measured using light scattering experiments.

- **Chapter 3** We present "Colloidoscope", a deep learning–based particle tracking pipeline that employs a 3D residual U-net trained on simulated colloidal configurations convolved with realistic point spread functions and noise to mimic experimental conditions. We will show that compared to conventional methods, "Colloidoscope" is able to track a higher fraction of particles, with reduced localisation uncertainty, particularly for dense systems and low-contrast images, while avoiding false positives. We then validate the output with simulated data, experimental measurements, and higher-order structural analysis to demonstrate that "Colloidoscope" produces high-quality particle coordinates with less parameter tuning, compared to conventional methods, enabling more reliable particle-resolved studies of colloidal systems.

- **Chapter 4** In this chapter, we revisit this long-standing discrepancy between hard sphere nucleation rates extracted from computer simulations and those calculated from light scattering experiments using particle-resolved confocal microscopy and a deep learning tracking routine ("Colloidoscope") to determine experimental state points with unprecedented precision. By analysing pre-critical nuclei and comparing their free-energy barriers with large-scale simulations, we find good agreement between experiment and computer simulation across the coexistence regime.

- **Chapter 5** We investigate the origin of the long-standing discrepancy between hard sphere nucleation rates measured in light scattering experiments and those obtained from com-

puter simulations of hard sphere systems. Using confocal microscopy, we reproduce the Paulin–Ackerson method for determining effective volume fractions and extend it with particle-resolved analysis. Multiscale imaging combined with a deep learning segmentation model reveals crystalline structures present in the sedimenting liquid, which systematically bias the determination of volume fraction, leading to the discrepancy.

- **Chapter 6** We investigate Ostwald's rule of stages in colloidal systems of dipolar particles using particle-resolved confocal microscopy. Some state points where body-centred tetragonal (BCT) is the stable phase, we observe heterogeneous nucleation of a metastable hexagonal close-packed (HCP) crystal, which subsequently melts and is replaced by BCT. Analysis of the fluid surrounding the HCP crystal shows a drop in the volume fraction, which destabilise the HCP nuclei while enabling BCT growth. Higher-order structural analysis reveals that dipolar interactions promote clusters compatible with BCT.

- **Chapter 7** We investigate the optimisation of self-assembly in dipolar colloidal systems by systematically varying protocols of the dipolar interaction strength. Using confocal microscopy and particle-resolved analysis, we compare protocols of different shape at different state points. The quality of the crystallisation process was quantified via crystal population and domain size. We find that crystallisation is characterised by a balance between strong dipolar forces, which promote order but limits mobility, and weaker forces, which enhance rearrangements and defect annealing. Optimal assembly occurs near the liquid–BCT phase boundary, with square-wall protocols between moderate and high field strengths producing the largest crystal domains.

- **Chapter 8** We present a three-dimensional model system of active colloids based on Janus particles that are self-propelled by induced-charge electrophoresis under an alternating electric field. In addition to activity in the plane perpendicular to the field, the particles interact via dipolar interactions, leading to rich phase behaviour ranging from active gases and liquids to travelling strings, dynamic labyrinths, and active crystals. We describe in detail the synthesis of Janus particles, sample preparation, and show activity of our particles by particle-resolved confocal microscopy. We successfully synthesised active particles and, for the first time, accurately measured the thickness of the deposition layer, which is responsible for the degree of activity in the systems.

1.2 Colloids as Model Systems

The scientific field of soft matter physics covers a wide range of different systems. The systems under investigation all have in common that they are easily deformable by thermal fluctuations (energy scale comparable to k_BT), weak external forces or other changes in the environment. Important systems include polymers, liquid crystals, foams, gels and biological matter, all of which have an intermediate length scale between molecular and macroscopic (Fig. 1.2) [70].

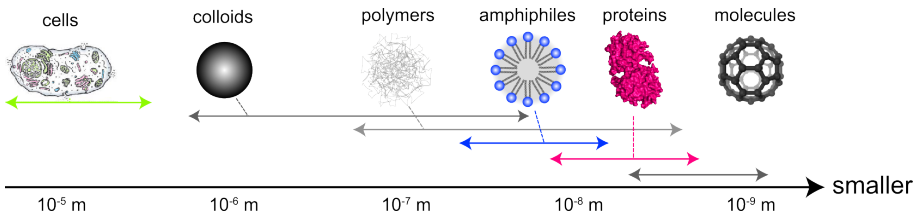

Figure 1.2: Colloids in the World of Soft Matter. Overview of length scales covered by soft matter physics. Reproduced from [71]

Colloids play a particularly important role in the field of soft matter for two reasons. Firstly, colloids themselves represent an important system in industry. In the food production and cosmetics sectors, colloids are used in a wide variety of ways. Secondly, and more importantly for us, they can be seen as model systems of atomic or molecular systems [72]. Colloid science experienced an upswing thanks to breakthroughs in the synthesis of new colloidal systems mainly driven by industrial interests, especially in the decades shortly before the turn of the millennium [73, 74].

Colloids are a dispersed system in which mesoscopic particles, with a typical length scale of a few nanometres to micrometres, are dispersed in a continuous medium, in our case a liquid. The mesoscopic size means that they are large in relation to molecules or atoms and that quantum effects can be neglected, but their movement is nevertheless dominated by Brownian motion (thermal energy), whereby sedimentation only plays a minor role [44]. The famous Péclet number compares the two motions and is defined as

$$\mathrm{Pe} = \frac{\tau_B}{\tau_g}, \tag{1.1}$$

where τ_B, τ_g describe the time it takes for an isolated sphere to diffuse (τ_B) or sediment (τ_g) its own radius. For colloidal systems in which diffusion dominates, $\mathrm{Pe} < 1$ is valid.

The advantages of working with colloidal systems are manifold. Firstly, interactions in colloidal systems can be described using classical physics, which makes them easily accessible for studies

using computer simulations. Furthermore, they are slow and visible under a microscope. The observable lengths and time scales, due to their mesoscopic size, make them ideal test subjects for phenomena such as crystallisation, melting or phase separation, which would occur too quickly in atomic systems. Furthermore, they can be analysed directly using optical microscopy, or scattering. In this work, we will mainly investigate particles in the size range of a few micrometres using 3D confocal microscopy. The coordinates of the particles can be extracted from the images, on the basis of which a detailed investigation of the structure of the samples during interesting phase behaviour can be carried out, so-called particle-resolved studies (PRS) [44].

Many years ago, Charles Frank postulated the idea that the underlying processes of freezing and crystallisation are influenced by the aggregation of particles into higher-order clusters with five-fold symmetry that suppress crystallisation and play an important role, for example, in the glass transition [75]. With our experiments we want to help understand the essential relationship between the structure of a liquid on a particle-resolved basis and its macroscopic properties.

Further reasons are tunability and control. Colloids exist in a variety of particle sizes, shapes and with different interaction potentials. From experimental realisations of nearly perfect hard spheres, the simplest and most studied colloid model, to long-range attractive or repulsive interactions, to patchy particles in which anisotropic interactions are realised with surface treatment and DNA coating, colloids exhibit rich phase behaviour that can be studied to provide insights into the theory of freezing and self-assembly [76].

The simplest model system of hard spheres, for example, exists in fluid, crystalline and even glassy states. The phase diagram shows a coexistence regime between fluid and crystal, with phase transitions driven solely by entropy, making it an ideal subject for the study of aggregation, stability and other collective phenomena [16, 77]. Unlike atoms in a metal, which have strong, stiff bonds (eV scale), colloidal hard spheres interact solely through volume exclusion, with energy scales comparable to k_BT. That is why, although the name suggests otherwise, they are regarded as systems within the world of soft matter. The phase diagram will be discussed in detail in Chapter 1.3.2.

In the following sections, we want to introduce colloidal model systems used in this thesis. We start with the simplest system of hard spheres, introduce a system with anisotropic dipolar interactions [78] and finally describe systems of active colloids that show interesting phase behaviour [61], in detail.

1.3 Colloidal Hard Spheres

Here we want to introduce the system of colloidal hard spheres, which has received enormous attention in recent decades because it can be used as a model for simple liquids. It follows the same rules of statistical physics, can be described classically and are therefore easily accessible for computer simulations and theoretical predictions. The system exhibits an entropically driven phase transition from fluid to crystal and has become easily controllable due to technical advances in the synthesis of particles in recent years [16].

We want to discuss how the particles interact in experiments, how they can be investigated with computer simulations and how their phase behaviour is predicted. A detailed discussion of the synthesis of these particles is beyond the scope of this work and can be found in other publications. As there are no perfect hard spheres in experiments [23, 24], we want to discuss in detail how far their behaviour deviates from perfect hard spheres in computer simulations.

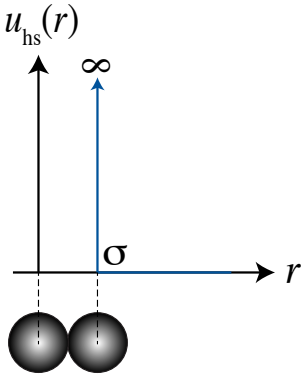

Figure 1.3: Hard sphere pair interaction potential as a function of inter-particle distance r. Reproduced from [16]

The interaction potential of true hard spheres is easily explained. There is no interaction for distances greater than the particle diameter ($r > \sigma$) and the particles are not allowed to overlap (see Fig. 1.3). Despite this simple interaction potential, systems of hard spheres exhibit an interesting variety of different phases. As the particles undergo thermal motion, they explore the phase space and self-assemble into different structures, such as gases, liquids, crystals and even glasses. They are of particular interest in the field of colloidal science because they combine many properties that simplify the investigation of the system. Colloidal hard spheres are large in size, which means that they can be studied with a microscope in real space. Such particle-resolved studies are useful because they allow the fundamental processes of nucleation to be investigated. Samples consisting of smaller particles can be studied using light scattering experiments. This brings us to the second

advantage, which is directly related to size, namely that their dynamics also lie within a range that is easily accessible for experiments and computer simulations. Colloidal hard spheres diffuse the distance of their own radius on the order of seconds. The characteristic time scale is defined by the Brownian time, the time it takes an isolated sphere to diffuse by its own radius

$$\tau_B = \frac{(\sigma/2)^2}{D_0} = \frac{3\pi\eta\sigma^3}{4k_BT}, \tag{1.2}$$

where D_0 is the diffusion coefficient, η is the solvent viscosity, k_B is Boltzmann's constant and T is the temperature [16].

This allows interesting processes associated with phase behaviour to be investigated in real time. Another advantage is that this phase behaviour is determined by a single control parameter, the volume fraction. It is defined by:

$$\phi = N\frac{\pi\sigma^3}{6V} \tag{1.3}$$

where V is the volume of the entire system, σ is the diameter of a single particle and N describes the total number of particles. Unfortunately the interaction potential of experimental hard spheres is not accurately described by Fig. 1.3, because in real systems the interaction potential always has a degree of softness due to electrostatics, the stabilisation layer, or other sources. Then, the hard sphere diameter for experimental particles becomes an effective diameter that includes the soft part of the potential and allows a mapping of the experimental system to perfect hard sphere systems in computer simulations [16]. A detailed explanation will be given in Chapter 4.3.

The final advantage, already mentioned above, lies in the classical nature of the interaction. The properties of the system can be described using the tools of classical physics, which makes them easily accessible for computer simulations and theoretical studies.

1.3.1 Colloidal Hard Spheres in Experiments

Over the last few years, a variety of model systems for colloidal hard spheres have been developed and characterised. These include sterically stabilised silica particles, aqueous electrostatically stabilised polystyrene systems, microgels and, of particular interest to us, sterically stabilised polymethyl methacrylate (PMMA) particles. Only the latter will be investigated in the further course of this thesis. Our PMMA particles are sterically stabilised by a polyhydroxystearic acid (PHSA) layer and labelled with a fluorescent dye, which makes them ideal for 3D investigations using confocal

microscopy. For this purpose, they are typically suspended in a solution matched to their refractive index and density. The exact composition is described in more detail in Chapter 2.1.1. Like all experimental colloidal model systems, PMMA particles synthesised in the lab are characterised by a specific distribution of particle diameters, quantified by the polydispersity s. The polydispersity may be defined as the standard deviation of the particle diameters by the average diameter in percent. Typical values for PMMA systems are $s \lesssim 5$, i.e. crystallisation proceeds in a manner comparable to that in the monodisperse case [16]. Details of the influence of polydispersity on the phase behaviour of colloidal hard spheres will be discussed in Chapter 1.3.2.

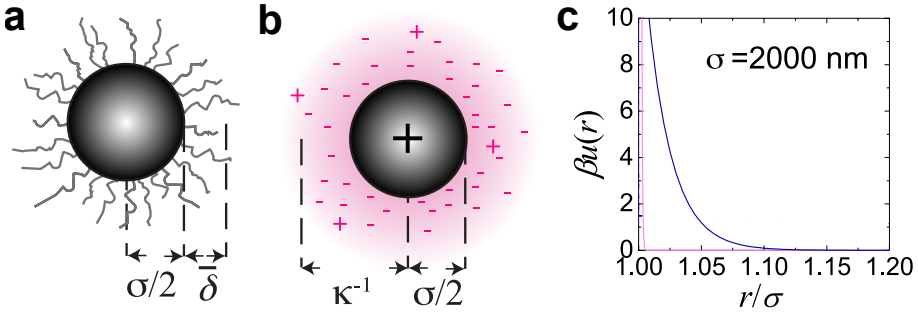

Figure 1.4: Sketch of real hard spheres in experiments (a) A sterically stabilised particle with hard core diameter σ and averaged stabilising layer thickness δ. (b) Charge distribution of a charged hard sphere due to residual charges on the surface of the particle, introducing an effective diameter σ_{eff}. (c) Example of effective interaction potential. Reproduced from [16].

The only control parameter in systems of hard spheres is the volume fraction mentioned above. However, since in the real world the particles do not interact with the perfect hard spheres interaction potential, the effective volume fraction is often used to describe the state point of experimental samples. In the past, a great deal of effort was made to reliably determine the effective volume fraction taking into account different interactions existing exclusively in real systems. Figure 1.4 shows the complexity of determining an effective diameter. Looking at the sketch of a sterically stabilised sphere, determining the diameter appears to be highly non-trivial. There are definitions for the diameter of the hard core, σ in Fig. 1.4(a) and the diameter of the core including the stabilising layer $\sigma + 2\delta$ [16].

Another definition can be derived from the dynamics of the particles, which can be calculated from Eq. 1.2. The diffusion constant is measured and used to determine the hydrodynamic diameter of an imaginary sphere moving according to the same laws [16].

For our purpose, the most accurate description of a hard sphere in experiments takes into account that experimental hard spheres always carry an amount of charge Fig. 1.4(b). Residual charges on the surface of the particles lead to a softening of the interaction potential, which must be

carefully considered in experiments. To be able to reliably simulate such systems one needs a precise description of the interaction.

The effective interaction potential $u(r)$ can be divided into different contributions.

$$u(r) = u_s(r) + u_{\mathrm{vdW}}(r) + u_{\mathrm{Yuk}}(r), \tag{1.4}$$

where u_s is the interaction potential of sterically stabilised particles, which can be described by an inverse power-law potential with energy scale ϵ_{ipl},

$$u_s(r) \approx \epsilon \left(\frac{\sigma}{r}\right)^n, \tag{1.5}$$

where σ describes the particle diameter and r denotes the inter-particle distance. A representation of the interaction potential of a 2000 nm particle with $n = 1800$ is shown in Fig. 1.4(c) (pink line).

The particles in this work are, to image them with 3D confocal microscopy, index matched to the solvent, which decreases the vdW interaction. Also, the particles are well separated due to the sterically stabilisation and therefore the $u_{\mathrm{vdW}}(r)$ can be neglected.

As mentioned above in real hard sphere systems the particles always carry some amount of charge, leading to a softening of the interaction potential. The contribution of the softening, which in linearised Poisson-Boltzmann theory has a Yukawa form,

$$u_{\mathrm{Yuk}}(r) = \epsilon_{\mathrm{Yuk}} \frac{\exp\left[-\kappa(r-\sigma)\right]}{r/\sigma}, \tag{1.6}$$

where $\kappa = \sqrt{4\pi\lambda_B\rho_{\mathrm{ion}}}$ denotes the inverse Debye screening length, with ρ_{ion} the number density of monovalent counterions, and $\beta\epsilon_{\mathrm{Yuk}}$ describes the contact value of the Yukawa interaction,

$$\beta\epsilon_{\mathrm{Yuk}} = \frac{Z_e^2}{(1+\kappa\sigma/2)^2}\frac{\lambda_B}{\sigma}. \tag{1.7}$$

Here Z_e is the number of residual charges on the colloid and λ_B the Bjerrum length,

$$\lambda_B = \frac{e^2}{4\pi\epsilon_0\epsilon_r k_B T}, \tag{1.8}$$

where e is the electronic elementary charge, ϵ_0 is defined as the permittivity of the vacuum and ϵ_r describes the relative dielectric constant. The Bjerrum length describes the distance between two elementary charges, where the interaction energy equals k_BT [16].

In our case, we use solvent mixtures consisting of either cis-Decalin and cyclohexyl bromide (CHB), or Decalin, Tetralin and CHB. The solution has a high dielectric constant of approximately $\epsilon_r = 5.4$. To shield the strong electrical charge of the particles, we add tetrabutyl ammonium bromide (TBAB) salt to the solution. A more detailed and technical description of the synthesis of the samples follows in Chapter 2.1. For our system we determine $Z_e \approx 500$ and a corresponding Debye length of around $\kappa^{-1} \approx 100$ nm. The interaction potential is shown in Fig. 1.4(c) (blue line). Compared to the interaction potential of a perfect hard sphere that can only be realised in computer simulations, we see that particles in experiments always interact with some degree of softness to their interaction potential. We are therefore interested in a definition of the effective diameter of experimental hard spheres that allows us to map the state point of the experimental samples onto the predictions of the simulations [16].

1.3.2 Phase Behaviour of Colloidal Hard Spheres

We now want to examine the equilibrium phase behaviour of hard spheres. As described above, perfect hard spheres only exist in computer simulations, but not in experiments. Hard spheres in experiments always interact with a certain degree of softness in the interaction potential due to residual charges on the surface. Furthermore, in experiments, the particles always have slightly different diameters, i.e. they show polydispersity. Monodisperse systems can only be realised in computer simulations [24]. However, as we will show in the next chapter, a polydispersity of $s < 0.05$ has only a very small influence on the phase behaviour [79]. We will first explain the equilibrium behaviour of monodisperse hard spheres and then give a brief explanation of the influence of polydispersity on the phase diagram.

For the reasons mentioned above, the first attempts to determine phase behaviour were studies using computer simulations [80, 81]. Since this thesis also investigates the phase behaviour of other systems with, for example, dipole interactions in addition to investigating hard spheres, various computer simulation techniques are described in Chapter 2.3.

Monodisperse Hard Spheres

The only control parameter for phase behaviour in hard sphere systems is the volume fraction ϕ, which acts like an inverse temperature. The particles only interact when they come into contact, which means that the Helmholtz free energy is defined solely by entropic contributions.

For small ϕ, the system is in a fluid state, and for high ϕ, it is in a crystalline state. In this work we want to focus on 3D systems, where a coexistence regime between the two states in which both fluid and crystal are stable, exists. If the volume fraction of the fluid phase is increased above a critical value, the system undergoes entropically driven phase transition. The arrangement of particles in ordered patterns is entropically favourable because the particles have more free volume to move around. This behaviour has been confirmed numerically and the volume fractions for freezing $\phi_f = 0.4917$ and melting $\phi_m = 0.5431$ have been determined with increasing accuracy in recent years [16]. These values were in reasonable agreement with experimental estimates from Pusey and van Megen [82]. A representation of the different phases with confocal images of PMMA particles with $\sigma = 2\mu$m are shown in Fig. 1.5.

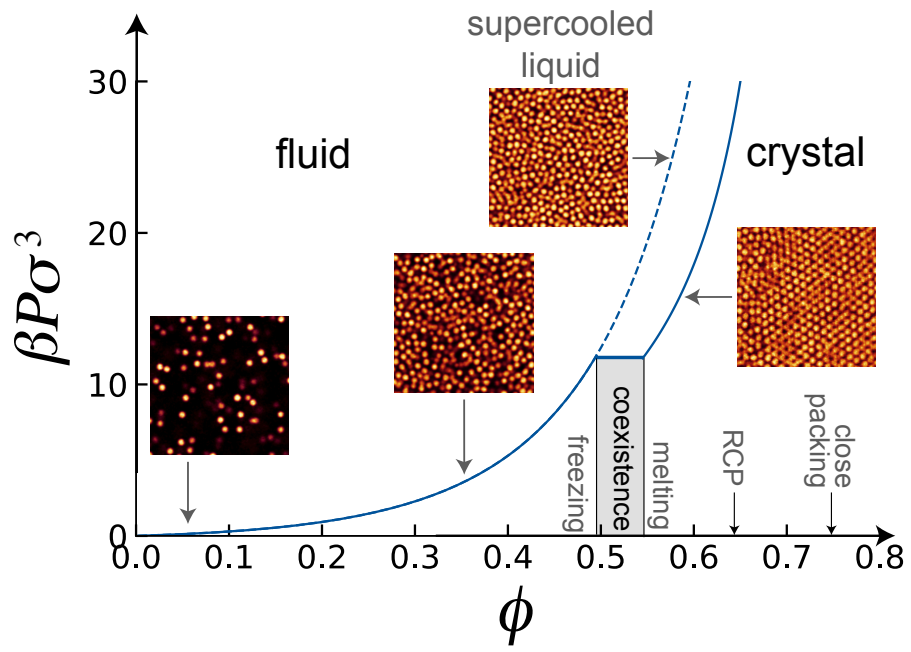

Figure 1.5: Equation of state and phase diagram of hard spheres with freezing volume fraction $\phi_f = 0.4917$, melting volume fraction $\phi_m = 0.5431$, random-close packing $\phi_{\mathrm{rcp}} \approx 0.64$ and crystal close packing $\phi_{\mathrm{cp}} = \pi/3\sqrt{2} = 0.740...$. The pressure $\beta P\sigma^3$ as a function of volume fraction ϕ is shown as the solid line and can be approximated for the fluid by the Carnahan-Starling expression [83]. For the crystal it is approximately given by the approximation of Hall [84]. The dashed line represents the metastable regime, where the hard-sphere liquid is supercooled and the glass transition can be found. Reproduced from [16]

With the advent of sterically stabilised PMMA particles as model systems for hard spheres, experimental systems became easier to control and new comparisons could be made. However, it turns out that simply mapping the state points between experiments and computer simulations is associated with certain difficulties. It is important to note that inaccuracy in determining the effective volume fraction is accompanied by inaccuracy in determining the phase boundaries for experimental systems [16].

Polydisperse Hard Spheres

In experimental systems, the particles are always characterised by a certain diameter distribution. We now want to consider the influence of polydispersity on the equilibrium phase behaviour of hard spheres. A representation of the phase diagram for different degrees of polydispersity can be seen in Fig.1.6.

For small values $s < 5\%$, no significant influence on the phase boundaries can be detected [85]. For larger values, however, the boundaries shift to higher volume fractions and crystallization is suppressed. Studies using computer simulations in this regime have found that the systems favour crystallization into multiple crystal domains, which differ in particle size [86].

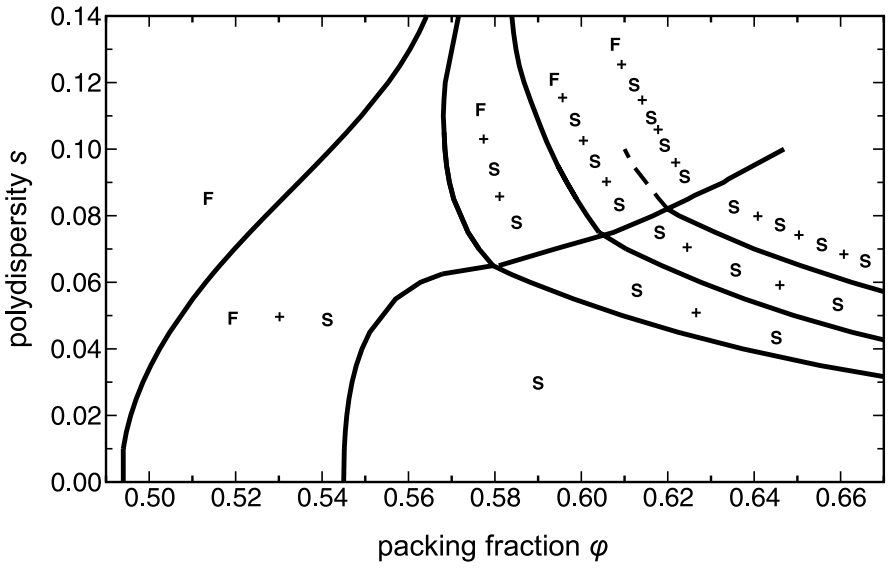

Figure 1.6: Equilibrium phase diagram of polydisperse hard spheres. Phase diagram shows shift of the boundaries for small and coexistence regimes for intermediate and large values of s. Systems form different crystal domains with large and small particles. Reproduced from [87]

1.3.3 Sedimenting Colloidal Hard Spheres

Here we would like to introduce the phase behaviour of out-of-equilibrium systems of hard spheres. There are two reasons for this: Firstly, the Paulin-Ackerson method [43] for determining phase boundaries using sedimenting samples is still widely used and will be introduced in Chapter 3. It is important for the further course of this thesis to understand where possible inconsistencies exist that could bias the determination.

On the other hand, there is no perfect density matching in experimental systems (on Earth), and

therefore there could be some influence from sedimentation on the nucleation process, even if only minor. In order to quantify this influence on phase behaviour, we will briefly explain how one can quantify the sedimentation process in the system. Chapter 2.1.1 provides a more technical description of the density matching protocol used to prepare the samples analysed in this work.

If a non-density-matched sample is allowed to settle in a gravitational field until equilibrium is reached, the equation of state can be determined from the density profile [88]. We will attempt to describe how this equilibrium state arises between the force field that pulls the particles downward and entropy that favours a homogeneous mixture of the system. To this end, we introduce a quantity that describes the relationship between Brownian motion and sedimentation, known as the Péclet number. It is defined as

$$\mathrm{Pe} = \frac{\tau_B}{\tau_g} = \frac{\sigma/2}{\xi_g} = \frac{\pi\sigma^4\delta\rho g}{12k_BT}, \tag{1.9}$$

where τ_B is the Brownian time and τ_g is the gravitational time, i.e., the time it takes for an isolated particle to sediment its own radius σ. The ratio therefore indicates how strongly the particles sediment compared to their Brownian motion. Another quantity that is frequently used in this context is the so-called gravitational length $\xi_g = k_BT/mg$, where mg is the buoyant mass, which can be determined from the density difference $\delta\rho$ between the solvent and the particle [16].

For highly diluted systems, the gravitational length can be derived from the equilibrium density profile. For systems with a high volume fraction and slow sedimentation (Pe$\ll 1$) on the other hand, sedimentation can be described as a batch settling process. It is assumed that the density profile over time can be described by a set of coupled equations. In this picture, sedimentation is slowed down due to the high volume fraction. Over time a crystal sediment forms at the bottom of the system, with a clear interface to the liquid. However, crystallisation in the sedimenting liquid is neglected [89]. Further description of sedimenting systems can be found in Chapter 5.

1.4 Dipolar Colloids

Now that we have explained the simplest system of hard spheres, we want to describe a slightly more complex interaction potential. Colloids with dipolar interactions have attracted considerable interest in recent years. In contrast to hard spheres, the phase diagram is determined by two control parameters: the known volume fraction and the strength of the dipolar interaction. In the following,

we will describe the nature of this interaction and the phase behaviour of dipolar colloids.

1.4.1 Induced Dipolar Interaction

Colloids in an external electric field interact with a dipole-dipole particle interaction, which can be written as

$$\frac{u_{\mathrm{dip}}(r,\theta)}{k_B T} = \frac{\gamma}{2}\left(\frac{\sigma}{r}\right)^3 \left(1 - 3\cos^2\theta\right), \tag{1.10}$$

where u_{dip} is the dipolar interaction, $k_B T$ is the thermal energy, and θ is the angle between r and the z-axis (see Fig. 1.7(a)). The vector r lies between the centres of two colloids.

For experiments, $\gamma = \gamma_{\mathrm{exp}}$ applies and can be written as

$$\gamma_{\mathrm{exp}} = \frac{\mathbf{p}^2}{2\pi\epsilon_s\epsilon_0\sigma^3 k_B T} \tag{1.11}$$

where ϵ_s is the dielectric constant of the solvent and $\mathbf{p}$ describes the dipole moment

$$\mathbf{p} = \frac{\pi}{2}\alpha\epsilon_s\epsilon_0\sigma^3\mathbf{E}_{\mathrm{loc}}. \tag{1.12}$$

We define the ratio of the dielectric constants of particles ϵ_p and solvent ϵ_s as

$$\alpha = \frac{\epsilon_p - \epsilon_s}{\epsilon_p + 2\epsilon_s}. \tag{1.13}$$

To define the local electric field $\mathbf{E}_{\mathrm{loc}}$, we refer to previous work on such systems [90] and define

$$\mathbf{E}_{\mathrm{loc}} = \frac{\mathbf{E}}{1 - \alpha\pi/6} \tag{1.14}$$

which holds under the assumption of a cubic crystal. The total interaction u_{total} for the particles can then be expressed as the sum of the interaction of hard spheres u_{hs} and the dipole-dipole interaction u_{dip}

$$u_{\mathrm{total}}(r,\theta) = u_{\mathrm{hs}}(r) + u_{\mathrm{dip}}(r,\theta). \tag{1.15}$$

Figure 1.7(a) shows a schematic representation of the forces in the system of dipolar colloids. The particles attract each other parallel to the electric field and repel each other perpendicular to it [51].

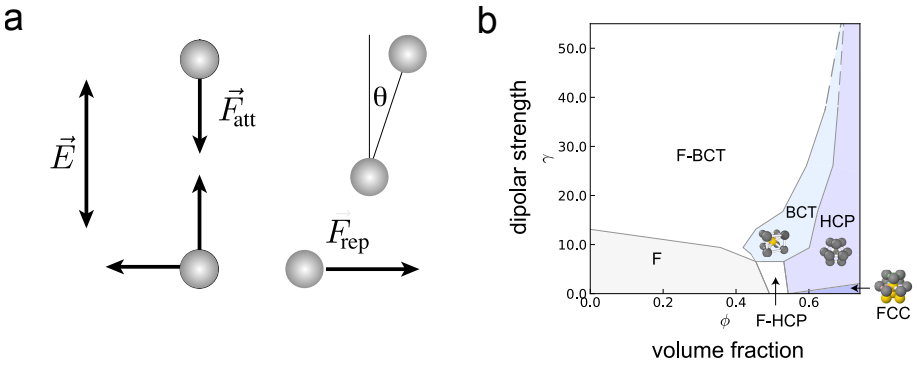

Figure 1.7: Schematic representation of dipolar interaction and phase diagram. (a) Dipolar interactions in a colloidal model system. Here an AC electric field $\vec{E}$ is applied in the z-direction, inducing dipolar interactions on the colloids. (b) Phase diagram for the colloidal dipolar system. Phase boundaries are taken from Hynninen and Dijkstra [51].

1.4.2 Phase Behaviour of Dipolar Colloids

Systems with such an interaction potential exhibit rich phase behaviour. Figure 1.7(b) shows the phase diagram extracted from computer simulations [51]. For small volume fractions and low dipole strength, the system is in the fluid phase. If the strength of the electric field and thus the dipolar interaction is increased, the system enters a string fluid phase in which the particles form chains parallel to the electric field, which form body-centred tetragonal crystals as the volume fraction is increased. There also exists a coexistence regime for intermediate volume fractions, where string fluid and BCT are both stable. For even higher volume fractions, the system spontaneously crystallises into hexagonal close-packed (HCP) and for very low dipolar strengths, similar to hard sphere systems, into face-centred cubic (FCC) crystal structures [51].

In Chapter 6, we will take a closer look at the nucleation processes of this model system and attempt to link the phenomenon of polymorph selection with the properties of the fluid. The realisation of dipolar colloids in experiments will also be explained in detail there.

1.5 Active Colloids

An emerging field of soft matter physics is the science of active colloids as a model system of active matter. Compared to passive systems like colloidal hard spheres or particles with dipolar interaction, in active matter, the systems are constantly out-of-equilibrium. In our case the particles are self-propelled units [91]. Examples of active matter and collective behaviour in nature include schools of fish [92], insects [93], or cell clusters [58].

Here we would like to give a brief introduction to active colloids. We will first describe the phenomenon of active Brownian motion and then explain how Janus particles can be self-propelled by induced charge electrophoresis. Finally, we will explain the phase behaviour of active Janus particles with dipolar interaction in 3D and compare it to the case of passive colloids with a similar interaction potential.

1.5.1 Active Brownian Motion

Active Brownian motion (ABM) is a widely used model for describing the motion of active colloids. In contrast to passive Brownian motion, in which particles move because they collide with solvent molecules, particles that perform ABM are self-propelled by consuming energy. The model assumes that the particles have a dominant axis of motion whose direction is fixed relative to the particle. In this direction, the particle is self-propelled at an approximately constant velocity v. However, the particles undergo rotational diffusion, which means that their orientation changes randomly over time. For short time scales, the particles perform persistent motion and random motion on a long time scale [94, 95]. Figure 1.8 shows a schematic representation of active Brownian motion with velocity v and particle orientation φ.

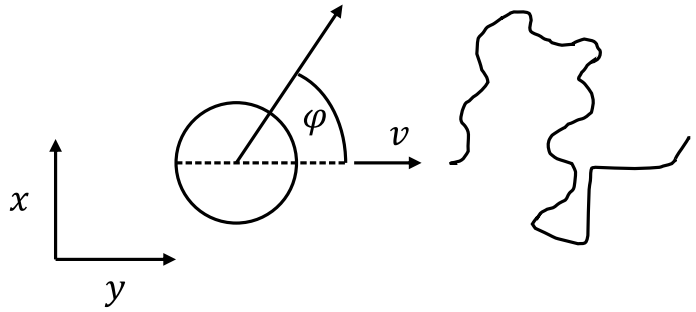

Figure 1.8: Sketch of active Brownian motion with particle velocity v and orientation φ

In our 3D model system, the particles are active in the xy plane but diffuse with passive Brownian motion in the z direction. The Langevin equations can then be defined as:

$$\dot{x}(t) = v\cos\varphi(t) \; + \; \sqrt{2D_{xy}}\,\xi_x(t), \tag{1.16}$$

$$\dot{y}(t) = v\sin\varphi(t) \; + \; \sqrt{2D_{xy}}\,\xi_y(t), \tag{1.17}$$

$$\dot{z}(t) = \sqrt{2D_z}\,\xi_z(t), \tag{1.18}$$

$$\dot{\varphi}(t) = \sqrt{2D_r}\,\xi_\varphi(t), \tag{1.19}$$

where v describes the self-propulsion velocity in-plane, D_{xy} describes the translational diffusion in x, y, D_z describes the translational diffusion along z and D_r describes the rotational diffusion, which can be expressed as Stokes-Einstein rotational diffusion coefficient

$$D_r = \frac{k_B T}{8\pi\eta a^3}. \tag{1.20}$$

The rotation decorrelates with time scale $\tau_r = 1/D_r$. The mean squared displacement (MSD) can be calculated and is given by

$$\langle r^2 \rangle = 4D_t t + \frac{2}{3}\tau_r^2 v^2 \left(\frac{t}{\tau_r} + \exp\left(-\tfrac{2t}{\tau_r}\right) - 1 \right). \tag{1.21}$$

Various domains can be identified based on the MSD [96]. For short time scales compared to rotational diffusion ($t \ll \tau_r$), the orientation of the particles has not yet become random and the MSD grows quadratically with time (ballistic motion) in two dimensions. For intermediate time scales ($t \approx \tau_r$), the orientation begins to decorrelate and ballistic and diffusive motion become relevant. In the MSD, a transition between quadratic growth and linear growth can be observed. For long time scales ($t \gg \tau_r$), the orientation is completely decorrelated and the exponential term disappears. The motion of the particles resembles Brownian motion with enhanced diffusion. The MSD grows linearly with time [97].

1.5.2 Active Janus Particles

Janus particles are micro- or nanoscale particles with two hemispheres with different surface properties [98]. The name comes from the two-faced Roman god Janus, because the particles similarly show a “two-faced” architecture [99].

The particles first appeared in the work of Casagrande and Veyssié, who described glass beads with a hydrophilic and a hydrophobic hemisphere [100]. One of the first mentions can be found in Pierre-Gilles de Gennes’ Nobel lecture in 1991. He introduced the concept of Janus particles and promotes it as an interesting way to study interfaces and self-assembly [101]. Then the initial work on active Janus particle systems was carried out in the early 2000s [102]. In our case, we use particles with a two-faced architecture as model system for active matter.

There are various implementations of active Janus particles in experiments, but here we want to focus on systems of active Janus particles driven by induced-charge electrophoresis (ICEP) [102,

103].

1.5.3 Induced Charge Electrophoresis

In our systems, we want to drive the particles using an external electric field and the approach of electrokinetics. Electrokinetics describes the movement of a fluid or particles through the interaction of an electric field with charges in the system. A fundamental role plays The electric double layer on a surface, i.e. a thin layer of counterions that shield the charges on the surface. In this context, electroosmosis describes the movement of a fluid relative to the charged surface under an electric field. When charged particles move in a fluid due to an electric field, this is referred to as electrophoresis. The mechanism is used, for example, in the sequencing of DNA strands, where nucleic acid molecules are placed in a gel and forced to move towards the positively charged anode by an electric field. The molecules are then sorted according to their size, because this determines how fast they can move through the gel.

In induced charge electrophoresis, a polarizable particle in an electric field acquires an asymmetric charge distribution. The charge distribution interacts with the applied field and produces a flow around the particle (Fig. 1.9(a)). In the symmetric case, the flows cancel each other out and there is no net movement of the particle.

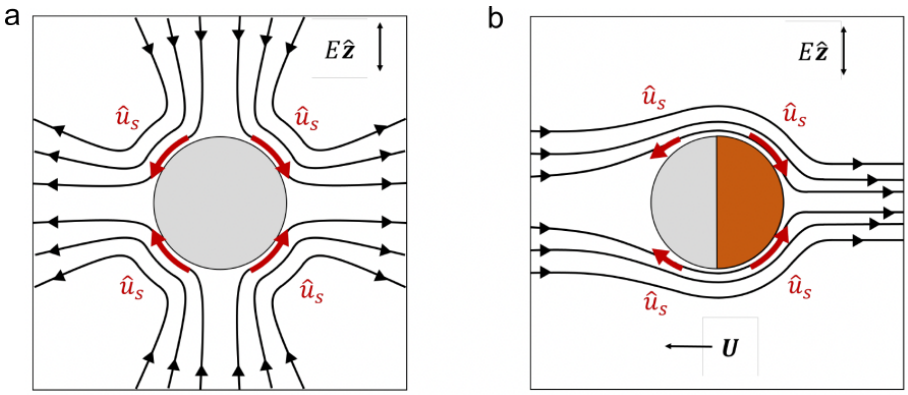

Figure 1.9: Sketch of fluid flows induced by induced-charge electrophoresis. (a) For a spherically symmetric conducting sphere. (b) For a spherical particle with one conducting and one dielectric hemisphere. Reprdoduced from [104]

However, if the symmetry of the system is broken, in our case by the different hemispheres (conducting and dielectric), the flows are no longer in balance and the particle moves (Fig. 1.9(b)). In other words, ICEP is the active motion of a particle in an electric field, caused by field-induced charges [102, 103].

1.5.4 Phase Behaviour of Active Colloids in 3D

In our experiments, we have the advantage of being able to bring many of these particles into a single system. These high-density systems of active particles exhibit a variety of interesting phenomena, from active self-assembly to active crystal structures. However, due to the electric field, the particles do not interact like self-propelled hard spheres, but rather with a dipolar interaction similar to that introduced in the previous chapter for passive colloids.

The phase behaviour of the system of the active colloids is thus defined by the competition between activity, volume fraction and the strength of the dipolar interaction. Figure 1.10 shows the phase diagram of the active (a) and passive (i) dipolar systems. For the active colloids the phase diagram shows different regions characterised by the dominant influences of activity, interaction and packing [105].

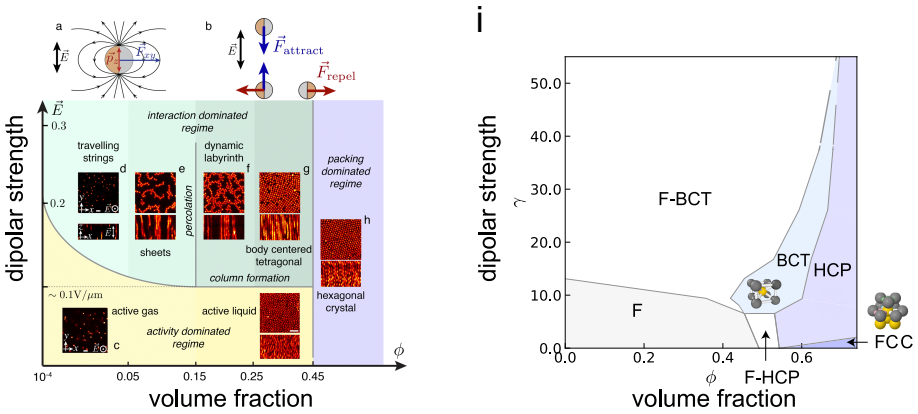

Figure 1.10: Comparison of phase diagram of active and passive dipolar colloids (a) Schematic representation of the dipole moment and active force of a Janus particle in an external electrical field. (b) dipolar interactions in the active system. (c-h) Phase diagram of active Janus particles with dipole interactions in 3D. (i) Phase diagram of passive dipolar colloids. Reproduced from [105].

For small volume fractions and low dipolar strength, the system is found in a state of 3D "active gas" (Fig. 1.10(c)), with activity in the plane perpendicular to the electric field (xy-plane) and diffusion in z-direction. For higher volume fractions but low field strength an active liquid can be observed. In this regime the system is dominated by the activity of the particles [105].

If the field strength is increased, the particles form parallel strings (Fig. 1.10(d)), which do not interact with each other at sufficiently low volume fractions. The strings can fill the entire height of the capillary and move as whole structures through the sample in xy-direction. Interestingly, the structures travel slower than individual particles, which can be explained by the different orientation of individual spheres in the strings and thus compensation of forces in different directions. Possibly,

for structures spanning the entire capillary, also friction or hydrodynamic effects close to the capillary wall play a role [106].

For slightly larger volume fractions of approximately $\phi \approx 0.01$, individual strings merge and form sheets (Fig. 1.10(e)) that exhibit interesting dynamic properties. If the volume fraction is increased to $\phi \approx 0.15$, the sheets can be observed to assemble into more complex structures. These assemblies bear similarities to an ever-changing labyrinth (Fig. 1.10(e)). New paths are constantly opening up and others are closing. It is important to note that these are 3D systems, but their structure can be described in quasi 2D. The symmetry is broken by the direction of the electric field, and strings, sheets and the walls that form the active labyrinth span over the height of the capillary in z-direction. Compared to the active gas and liquid for small dipole strengths and high activity, for strings, sheets and the active labyrinth the structure of the sample is dominated by the dipolar interaction between the particles [105].

With a further increase in the volume fraction, the packing dominated regime is entered. Here, it is favourable for the system to form structures with long-range order. The polymorph in which the sample nucleates depends on the volume fraction and the strength of the dipolar interaction. For $\phi \approx 0.3$ and strong dipolar interactions, body-centred tetragonal (BCT) crystal structures form spontaneously. This phase behaviour is observed and analysed for similar state points in field strength for passive systems in the previous chapters. For even larger volume fractions ($\phi \approx 0.45$), structures with hexagonal symmetry, consisting of FCC and HCP, crystallise, also consistent with observations of passive systems [48, 107].

1.6 Nucleation

One of the objectives of this thesis is to gain a better understanding of the underlying processes of crystal nucleation. To this end, we will provide a brief introduction to classical nucleation theory, Ostwald's rule of stages and heterogeneous nucleation. We will also briefly explain how nucleation rates can be measured using light scattering experiments.

In general, crystallisation can be defined as a process in which a solid with an ordered, repeating lattice structure forms from a disordered phase. This process can be divided into two main steps. First, nucleation, i.e. the initial formation of the new phase in the form of small nuclei, and then crystal growth, in which more units are added to a stable nucleus.

1.6.1 Classical Nucleation Theory

Classical nucleation theory is a widely used model for describing crystallisation processes, providing a framework for explaining how small nuclei of the new ordered phase form in the parent phase [108]. CNT links the change of the Gibbs free energy (ΔG) through the formation of a small nucleus with two terms representing interfacial free energy and bulk free energy.

$$\Delta G(r) = \Delta G_{\text{surface}} + \Delta G_{\text{volume}} \tag{1.22}$$

The contribution from the interfacial free energy (γ) has a positive sign and is the penalty for the formation of an interface between the liquid and solid phase. This term scales with the nucleus surface area (r^2). The other term favours the formation of the crystal phase because the growth of the bulk crystal phase reduces the free energy (the free energy of the crystal is lower than that of the disordered parent phase). It scales with the volume of the crystal nucleus (r^3). So the change in Gibbs free energy can be written as

$$\Delta G(r) = 4\pi r^2\gamma + \frac{4}{3}\pi r^3 \rho_s \Delta\mu, \tag{1.23}$$

where ρ_s is the number density of the bulk solid and

$$\Delta\mu = \mu_l - \mu_c \tag{1.24}$$

describes the difference between the chemical potentials of liquid and crystal μ_l, μ_c. Figure 1.11(a) shows a schematic representation of the free energy barrier that a newly formed nucleus must overcome in order to be stable and continue growing.

The associated size of a critical nucleus, which grows or shrinks with equal probability, is

$$r^* = \frac{2\gamma}{\rho_s|\Delta\mu|} \tag{1.25}$$

Then the maximum height of the free energy barrier (at r^*) is defined as

$$\Delta G^* = \frac{16\pi\gamma^3}{3(\rho_s|\Delta\mu|)^2}. \tag{1.26}$$

In other words, if due to thermal fluctuations in the system a crystal nucleus smaller than the critical nucleus $r < r^*$ forms, then the interfacial free energy term dominates and the nucleus

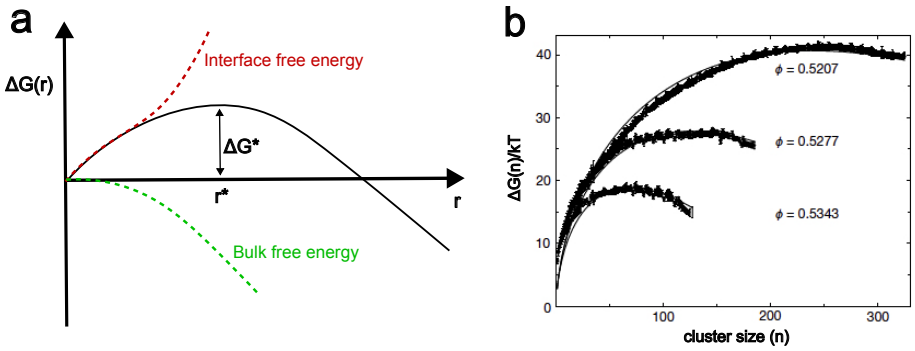

Figure 1.11: Free energy barriers. (a) Schematic representation of the nucleation barrier, that results from Interface free energy term and bulk free energy term. Critical nucleus size r^* with barrier height ΔG^*. (b) Free-energy barriers for hard sphere system as a function of the largest cluster size n from umbrella sampling simulations (data points) at different supersaturations. Solid were produced by fitting the data to CNT. Reproduced from [109].

shrinks. If a nucleus forms that is larger than the critical nucleus size $r > r^*$, the bulk free energy term dominates and the free energy decreases as the nucleus grows. It is stable. Figure 1.11(b) shows the free-energy barriers for a hard sphere system from umbrella sampling simulations at different supersaturations. Here we show the nucleation barrier as a function of n, the largest crystalline cluster size, in numbers of particles. The barrier heights increase strongly with decreasing volume fraction. The solid lines from fitting the CNT functional form to the simulation data show good agreement [109]. CNT thus provides an explanation for why nucleation processes are so rare in weakly supersaturated fluids. This approach can also be used to derive the nucleation rate J, i.e. the number of nuclei formed per unit volume and per unit time. It can be written as

$$J = \kappa \exp\left(-\frac{\Delta G^*}{k_B T}\right) = f^+ \rho_f Z \exp\left(-\frac{\Delta G^*}{k_B T}\right), \tag{1.27}$$

where κ is the attempt frequency which can be calculated from the single-particle attachment rate at the top of the barrier f^+, the number density of the fluid ρ_f and the Zeldovich factor Z which accounts for the probability that a critical nucleus will grow to become a macroscopic nucleus [110–113].

CNT is a powerful and simple model that can be used to describe nucleation events and predict crystallisation. However, it only applies under certain assumptions that must be analysed critically.

1.6.2 Challenging CNT

Here, we want to challenge some of the fundamental assumptions of CNT in detail. First, CNT assumes that the first-order phase transition can be described with a single order parameter [114, 115].

However, in the case of a liquid-to-crystal transition, both translational and orientational symmetries are broken, and the two features can change differently during the nucleation process [116]. Both experiments [29, 33] and computer simulations [39, 117, 118] have shown that in systems of hard spheres, for example, more than one order parameter is involved in the formation of precritical nuclei.

Furthermore, within the framework of CNT, it is assumed that the order parameter follows Markovian dynamics, i.e. it depends only on the present state and not on past history [119]. However, recent studies have shown that CNT is only a limiting case of a general theory that includes memory and out-of-equilibrium effects [120].

Another key assumption on which CNT is based is the capillarity approximation, i.e., the assumption that nucleation properties can be derived from the bulk properties of the amorphous liquid and the crystal. In a recent study, this assumption was questioned on the basis of polymorph selection. CNT predicts identical nucleation rates for crystal polymorphs when bulk and interfacial free energies are identical. Molecular simulations of a system with equal free energies across all polymorphs, however, reveal differences in nucleation behaviour. The authors argue that this discrepancy highlights CNT's key limitation: the neglect of structural fluctuations in the liquid phase [121].

On the other hand, it should be noted that even if the capillarity approximation is violated in the small nucleus regime, the theoretical framework can still be an effective tool for predicting nucleation processes in various systems if fundamental constants are renormalised. The interfacial energy depends on the curvature and surface structure of the small nuclei. There are therefore regimes in which CNT makes more or less reliable predictions. Particular caution is required when fitting to experimental data. A recent study has shown, for example, that data from computer simulations correspond well with predictions made by CNT when a curvature-corrected interfacial tension was used [122].

Experimental systems are vulnerable to heterogeneous crystallisation due to confinement by capillary walls or impurities.

1.6.3 Heterogeneous Nucleation

In heterogeneous nucleation, the nucleation barrier to be overcome is often reduced, resulting in increased nucleation. The term "non-favoured" in relation to crystal nucleation is related to the energy penalty that must be overcome to form an interface between the parent phase and the newly

formed crystal phase.

Constaining a system and bringing it into contact with a structure that dictates a certain geometry reduces this interfacial free energy contribution and thus lowers the nucleation barrier. The formation of a critical nucleus becomes more likely and the system crystallises on a smaller time scale. In experiments in particular, it is important to ascertain the role that heterogeneous nucleation plays in the process being observed [16].

1.6.4 Polymorphism and Ostwald's rule of stages

When a system can transition into different crystal structures, the most stable form with the lowest free energy is often not observed initially. Usually, a metastable structure with free energy closest to the parent phase forms first. This is state A in Fig. 1.12. Compared to the crystallisation of the final and stable crystal, this transition is characterised by a lower nucleation barrier [53, 123].

Instead of forming directly, the system passes through several metastable phases with decreasing free energy. These phases can be amorphous solids or different crystal forms. This explains the early formation of disordered, liquid-like precursors during nucleation, as seen in some biominerals such as calcium carbonate, for example [124].

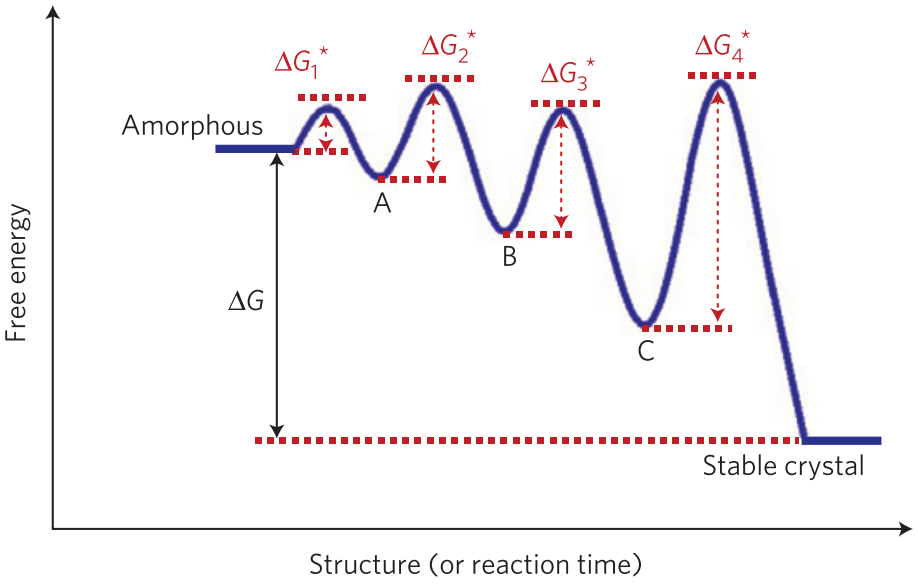

Figure 1.12: Schematic representation of Ostwald's rule of stages. A, B, and C correspond to metastable intermediate states, each associated with a local energy minimum. Every ΔG^* represents the activation barrier that must be overcome to transition to the subsequent phase. Reproduced from [123].

1.6.5 Measuring Nucleation Rates with Light Scattering Experiments

In addition to direct visualisation using light microscopy, there is another powerful approach for investigating the structure of colloidal systems: light scattering. We would like to provide a brief overview of the scattering technique to measure the nucleation rates in colloidal systems [29, 32, 125], because it is to this day the most commonly used method. Since Chapter 4 compares particle-resolved data obtained by confocal microscopy with predictions from light scattering experiments, we would like to establish a basis for analysing and interpreting scattering data.

In general, electromagnetic radiation is used in scattering experiments to investigate the structure of materials. The corresponding wavelength of this radiation for investigating colloids lies in the visible light range. In scattering experiments, the intensity of the scattered light $I(\mathbf{k}, t)$ manipulated by fluctuations in the refractive index in the scattering volume and its time correlation are recorded. Here $\mathbf{k}$ is the scattering vector defined as

$$\mathbf{k} = \mathbf{k}_s - \mathbf{k}_i, \tag{1.28}$$

where $\mathbf{k}_s, \mathbf{k}_i$ describe the wave vectors of the incident and scattered light. The two vectors define the scattering angle θ between them [126]. A schematic representation of a light scattering setup is shown in Fig. 1.13.

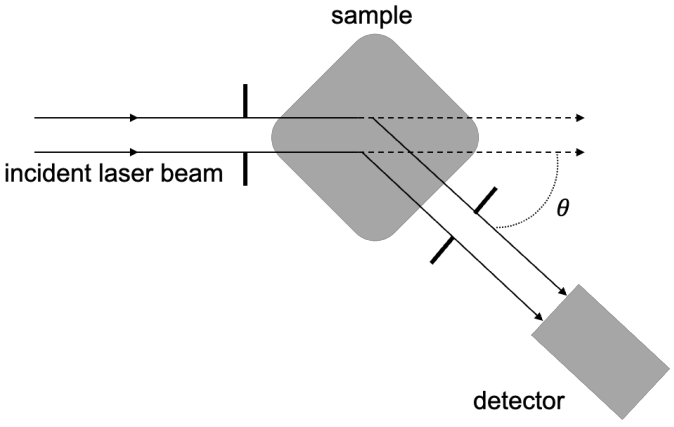

Figure 1.13: Schematic of a light-scattering setup with scattering angle θ defined by incident and scattered light.

With statistical light scattering (SLS), the recorded intensity is averaged over time and the structure factor can be measured.

$$S(\mathbf{k}) = \frac{1}{N} \sum_{j=1}^{N} \sum_{k=1}^{N} \langle \exp\left[-i\mathbf{k} \cdot (\mathbf{r}_j - \mathbf{r}_k)\right] \rangle \,, \tag{1.29}$$

where N is the total number of particles and $(\mathbf{r}_j - \mathbf{r}_k)$ is the relative separation vector between particles j and k. Also, the radial distribution function $g(r)$ can be calculated from $S(\mathbf{k})$ by Fourier transformation [126].

In order to extract nucleation rates from these measurements on colloidal systems, the structure factor is recorded over time and its change is measured. In a crystallising system, the structure factor can be broken down into the contributions from the crystal $S_{\mathrm{xtal}}(k)$ and fluid $S_{\mathrm{fluid}}(k)$.

$$S(k,t) = X(t)S_{\mathrm{xtal}}(k) + \big[1 - X(t)\big]S_{\mathrm{fluid}}(k), \tag{1.30}$$

where $X(t)$ is the crystal fraction. The average linear size can then be determined by

$$L_{\mathrm{nucl}}(t) = \frac{2\pi K}{w_q(t)}, \tag{1.31}$$

where $w_q(t)$ is the width of the peak at half maximum and K is the Scherrer constant, which is $K = 1.155$ for a cubic crystal [127]. The number density of averaged-sized crystals $n(t)$ can then be calculated from the crystal fraction $X(t)$ and the averaged linear size $L_{\mathrm{nucl}}(t)$ [32]

$$n(t) = \frac{X(t)}{L^3_{\mathrm{nucl}}(t)}. \tag{1.32}$$

From the time evolution of $n(t)$ a nucleation rate can be extracted.

Compared to confocal microscopy, this technique can be used to examine smaller particles, typically with a diameter of a few hundred nanometres, with good statistics. Using another method of scattering experiments, femtosecond X-ray diffraction, it is now even possible to investigate atomic and molecular systems. In the case of argon, for example, femtosecond X-ray diffraction was used to measure nucleation rates for the supercooled atomic liquid [128]. With a similar approach the structure of water in the regime of rapid ice crystallisation was analysed [129, 130].

The Brownian time for our colloidal particles scales with the particle diameter cubed. A particle that is 10 times larger therefore explores the phase space 1000 times slower [16]. With the light scattering experiments, nucleation events can therefore also be investigated in the range of small supersaturation. Comparisons of the measured nucleation rate for hard sphere systems with predictions by CNT have shown good agreement for this regime [29, 30, 125, 131]. In the higher supersaturation range, where the free energy barrier becomes smaller and nucleation is no longer an activated process, the situation is not as simple. Nucleation is no longer a rare-event there, and

crystallisation takes place simultaneously at many locations in the sample (spinodal limit).

Chapter 2

Methodology

2.1 Sample Preparation

In this thesis, we investigate various colloidal systems ranging from simple hard spheres to passive particles with a dipolar interaction and active colloids. The passive systems are very similar in terms of sample preparation. In both cases, micrometre-sized Polymethylmethacrylate (PMMA) particles are suspended in a solvent, which is designed to meet various requirements in terms of refractive index and density by varying the mixing ratios of the components. Accordingly, we provide a general description of the preparation of these colloidal systems. For the samples of active particles, the synthesis is described in detail in Chapter 8 as part of the thesis. We were able to make the production of Janus particles more robust and reproducible thanks to new measurement methods.

For our passive systems, we use PMMA particles, first developed by Yethiraj and van Blaaderen [48]. We use a mixture of Decalin, Tetralin and cyclohexyl bromide (CHB), whose composition is adjusted to achieve simultaneous refractive index and density matching between particles and solvent in order to image the particles with 3D confocal microscopy and minimise van der Waals forces [24]. In addition, the particles are sterically stabilised with short chains of poly-12-hydroxystearic acid (PHSA) [132]. However, electrostatic charges exist on the surface of the particles in the experimental systems, which lead to softness in the interaction potential. We use the salt tetrabutylammonium bromide (TBAB) to screen these charges and achieve an almost perfect hard sphere-like interaction [24]. As described above, the softness leads to a larger effective particle diameter σ_{eff}, which

must be carefully determined in order to calculate the effective volume fraction [23]. This applies equally to hard spheres and dipolar colloids, since we determine the volume fraction identically for dipolar systems that behave like systems of hard spheres without an electric field. The following describes how we prepare the solvent mixture and perform density matching in order to produce samples with a specific volume fraction.

2.1.1 Solvent Preparation

To introduce TBAB into the solvent, it is first dissolved in CHB. To do this, 14.9 mmol of the salt is added to 28.55 mmol of CHB, resulting in a supersaturated solution, which is placed in a water bath at 40 °C for approximately 5 days so that the salt can dissolve completely.

Now, an initial solvent mixture can be prepared that corresponds to the refractive index $n_{\mathrm{PMMA}} = 1.491$ and density $\rho_{\mathrm{PMMA}} = 1.180$ of PMMA. The PMMA particles are first dispersed in pure Decalin and centrifuged at 13,400 RPM for 10 minutes (relative centrifugal force $\approx 10^4$ g). The sediment then has a volume fraction of $\phi = 0.64$, which corresponds to that of a system with random close packing [24, 133]. If the supernatant is removed, the volume and weight fractions of particles and Decalin can be determined from the weight of the remaining pellet. From the properties of Decalin ($n_{\mathrm{Decalin}} = 1.474$, $\rho_{\mathrm{Decalin}} = 0.896$ g/mL), Tetralin ($n_{\mathrm{Tetralin}} = 1.541$, $\rho_{\mathrm{Tetralin}} = 0.973$ g/mL) and CHB ($n_{\mathrm{CHB}} = 1.495$, $\rho_{\mathrm{CHB}} = 1.324$ g/mL), the amount of each component in the mixture can be determined to match the properties of the PMMA particles.

The sample is then left to equilibrate for a week, during which time the particles absorb part of the solvent mixture and swell slightly, which affects the density matching. To ensure optimal composition and prevent sedimentation, the sample is centrifuged again at 13,400 rpm for approximately 15 minutes after this week. If the density of the solvent is too high and the particles have risen upwards, more Decalin must be added. If the solvent is not dense enough and the particles have sedimented downwards during centrifugation, more CHB must be added. This process is repeated until no sedimentation or creaming is visible in the sample after centrifugation at the same speed for 30 minutes. Previous studies have found that with this protocol the solvent composition can be tuned to match the particle density with a relative density error of less than 0.01% [23].

In the course of this work, sedimenting samples are also examined, targeting a specific Péclet number regime, where the sedimenting sample is dominated by Brownian motion ($\mathrm{Pe} \ll 1$). For this purpose, the necessary density difference $\delta\rho$ between particles and solvent can be calculated

from the desired Péclet number, which was introduced, together with the gravitational length, in Section 1.3.3.

$$\delta\rho = \frac{12 k_B T}{\pi \sigma^4 g} \mathrm{Pe}, \tag{2.1}$$

where σ is the particle diameter and g is the gravitational acceleration. After determination of the necessary density difference the solvent composition is changed accordingly. Since we assume that after density matching the particles and solvent have the same density, the amount of Decalin, with $\rho_{\mathrm{Decalin}} = 0.896$ g/mL, that needs to be added can be simply determined from the total volume and mass of the sample. To characterise sedimentation in the samples, the gravitational length can be measured by examining the equilibrium density profile of very dilute samples, which follows the barometric law.

The sample is now refractive index matched and the density has been adjusted as desired. Since we are primarily interested in nucleation processes, samples with a specific volume fraction must then be produced. To do this, the density matched systems are centrifuged for approximately 90 minutes at 13,400 rpm, during which time they are heated to 36°C. The density matching is broken and the particles settle to the bottom, forming a random close packed sediment with $\phi = 0.64$. For sedimenting samples, heating is, of course, not required. The supernatant is removed and the volume fractions of solvent and PMMA particles can be determined from the weight of the pellet. Then the required amount of previously removed solvent is added back to achieve the desired volume fraction.

We have found that this protocol is subject to a significant systematic error. Often, not all of the supernatant is removed and the volume fraction of the pellet is lower than previously thought. For this reason, test measurements were carried out before starting long series of measurements to determine the exact state point by mapping the volume fraction to computer simulations. A detailed description of this protocol is provided in Chapter 4. The samples were examined using confocal microscopy and particle coordinates are extracted. Then the structure was compared with configurations produced by computer simulations. By comparing the shape of the $g(r)$ and population of higher order clusters identified by the TCC we are able to determine the experimental volume fraction. The comparison of the structure provides a much more accurate estimate of the state point of the sample compared to weighing the components. From the characterised system, further systems can then be produced by adding or removing solvent.

2.1.2 Capillaries

For our experiments with confocal microscopy, samples with different volume fractions are loaded into glass capillaries of various sizes. The glass capillaries are made of borosilicate glass distributed by Vitrocom. Capillaries of different dimensions were used for different experiments in this thesis. For the density-matched hard sphere systems, we have high demands on image quality in order to obtain particle coordinates with high precision. For this purpose, we use square capillaries with the walls (100 μm) and an inner diameter of 200 μm. For macroscopically sedimenting samples, however, we use larger square capillaries with an inner diameter of 600 μm. The thickness of the glass wall is 120 μm. Using a confocal microscope with a suitable lens, it is still possible to image the centre of the capillary in order to avoid boundary effects in the recorded data.

For the dipolar and active systems, we produce the sample cells ourselves from two ITO cover slips, which induce the electric field in the sample as parallel electrodes. A detailed explanation of the sample structure is provided in Chapter 6.

After loading the capillaries, everything is sealed with Norland 63 and attached to a microscope slide. Before imaging, the samples are left to equilibrate for at least 20 minutes.

2.2 Confocal Microscopy

Here we explain how confocal microscopy works and what kind of techniques we used. Unlike atomic systems, colloids can be directly imaged with a confocal microscope if they are large enough. In contrast to widely used light scattering experiments, the coordinates of individual particles can be determined, allowing the underlying processes of for example, crystallisation, to be investigated at the particle level.

2.2.1 Working Principles

During this thesis, two different confocal microscopy techniques, laser scanning and spinning disk, were used. The laser scanning microscope was used to capture high-resolution 3D images of the hard spheres and dipolar colloids. The spinning disk microscope, mounted on a freely movable surface, was used to investigate the sedimenting samples.

Laser Scanning Confocal Microscopy

This imaging technique was developed in the 1970s [134–136], fuelled by the development of the first laser sources. Today, 3D images of samples can be taken *in situ* to analyse their structure in great detail. Figure 2.1 shows the principle of a confocal microscope in conventional epi-illumination mode. In general, the distribution of fluorescent dye used to label the particles in the sample is measured. The incident light passes through a dichroic mirror that reflects only the light returning from the sample onto the detector, so that the same lens serves as both objective and condenser. The condenser lens focuses the light onto a point in the sample. The fluorescent dye is excited and emits light that is focused through the objective lens onto the pinhole (P_2). Since the pinhole is positioned exactly in the conjugate focal plane, hence the name confocal microscopy, only light from the focal point in the sample reaches the detector. Beams from out-of-focus regions of the sample are shielded by the pinhole (dashed line in Fig. 2.1). In laser scanning confocal microscopy, piezoelectric elements in the microscope allow the incoming beam to be focused at any position in the sample and the intensity of the outgoing light to be measured individually. A 3D distribution of the fluorescent dye is determined voxel by voxel.

For imaging the density matched and dipolar samples we used a Leica SP8 confocal microscope in resonant mode. To analyse these samples, we need high-resolution 3D images and high recording speeds. In resonant mode, galvanometric mirror scanners are used, which oscillate at a specific frequency and thus scan the sample. This limits the control of position and speed, but higher scanning speeds are achievable. For our measurements, there is an optimum balance between frame duration Δt and resolution. In addition to averaging over individual lines in a frame, entire frames can also be averaged. However, the duration over which the averaging is performed must be significantly shorter than the Brownian time of the particles, because otherwise the movement between the individual recordings over which the averaging is performed is too large and the resolution is dramatically reduced. In our case, we only averaged over two lines in the scan for samples with very high volume fraction close to the freezing volume fraction of hard spheres ($\Delta t = 8$ s). In all other cases, we have avoided averaging in order to minimise the frame duration ($\Delta t = 4.5$ s). To be able to track particle coordinates from 3D images, the intensity distribution of individual particles must be as distinguishable from one another as possible. A small pixel size creates better resolution and thus fewer missed particles after the tracking process. We have chosen a pixel size of 200 nm/pixel for our 3D images, which corresponds to approximately 10 pixels per particle in the microscope image. Typically, we have recorded frames with dimensions of

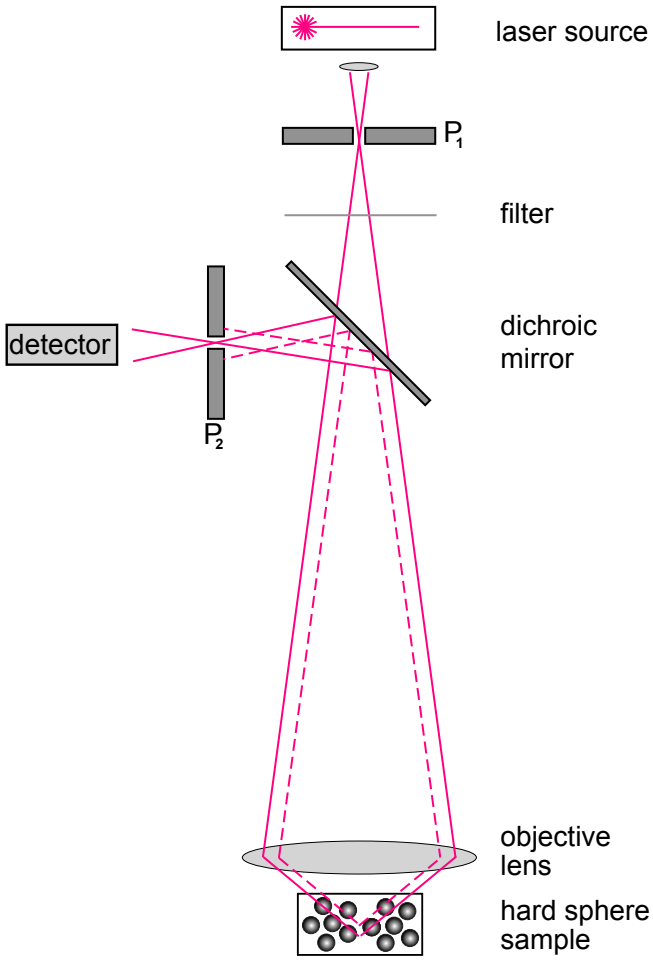

Figure 2.1: Sketch of the working principle of a confocal microscope [16]

$256 \times 256 \times 128$ pixels in the xyz-direction. Laser intensity and detector gain were adjusted so that photobleaching does not play a role during recording and the distribution of bright and dark pixels provides the best possible contrast. In addition, the gain was adjusted with the position in the sample during recording to compensate for the reduced intensity of the emitted light from deeper within the sample and to guarantee 3D images with homogeneous intensity distribution. Furthermore, the size of the pinhole was adjusted. For the dyed PMMA particles, an excitation wavelength of 552 nm was used and the pinhole size was determined in Airy units from the wavelength and the numerical aperture of the objective with 0.7 AU. Finally, the emission wavelength range can be adjusted. Acousto-optical elements make it possible to continuously adjust the target wavelengths and efficiently separate excitation from emission light. We selected a wavelength range of 565–625 nm for the emission.

Spinning Disk Confocal Microscopy

For the sedimenting hard sphere systems we used a different confocal microscope (Nikon Eclipse Ti). To be able to image the particles during the sedimentation process, we use a special setup, where the microscope as a whole can be rotated. Then the optical path is perpendicular to the direction of sedimentation and the sample can be imaged in the same position as it is stored. In contrast to the laser scanning approach, here a spinning disk confocal microscope is used. In this approach, instead of a single pinhole, thousands of pinholes are arranged in a spiral pattern on an opaque disc (Nipkow disk). During image capture, the Nipkow disc rotates with a high frequency and the light entering through the pinholes scans the sample in parallel. This allows for very fast image acquisition, but has the disadvantage of a slightly smaller resolution compared to the laser scanning approach [137].

For the measurements on the macroscopic sedimenting samples, 2D images of the centre of the capillary were taken and then stitched together to form multiscale images. One multiscale image consists of 15×100 individual images of 400×400 pixels (0.16 μm/pixel). The aim of these experiments is to distinguish crystalline from fluid regions. To this end, the imaging parameters are adjusted to enable rapid acquisition of individual images with high resolution.

In the microscopic image, particle centres are represented as intensity maxima, which must be identified in a sensible tracking process in the next step in order to determine the coordinates with sub-pixel resolution.

2.2.2 Particle Tracking

We want to perform a quantitative analysis of the structure of colloidal systems using confocal microscopy. To do this, the particles in the sample and their exact position must be determined very reliably. The process of particle tracking not only allows the structure of the systems to be analysed, but also enables trajectories to be extracted, consisting of linked positions and thus dynamic properties, such as the determination of the diffusion coefficient. In recent years, great progress has been made in this field. An ever-increasing proportion of particles, especially in dense samples, has been able to be analysed, and the accuracy of centre determination has also improved.

Here we would like to briefly introduce the conventional approach based on the work of Crocker and Grier [138]. Chapter 3 then describes a newly developed deep learning routine for tracking in

particularly dense colloidal systems.

We use the Python package "Trackpy" [139], which is a publicly available implementation of the Crocker Grier algorithm with many pre-programmed settings that allow users to customise tracking specifically to their sample and imaging properties.

The algorithm is developed around local maximum detection, whereby particle positions can be determined with sub-pixel resolution. To do this, the experimental image, in our case 3D, but similar in 2D, is filtered to remove background variations and noise. This is often done with a bandpass filter, which amplifies the bright regions with an approximate Gaussian shape of the particles and suppresses everything else. The algorithm then finds the brightest pixels and identifies them as possible particle centres if there are no brighter pixels in the vicinity within an adjustable size. With a further threshold for the minimum brightness of potential positions, false positive identifications can then be filtered out. Once potential particle centres have been identified, the next step is to determine the centre with sub-pixel resolution. To do this, Crocker and Grier uses a centroid calculation, which is an intensity-weighted average of the pixel coordinates of an intensity distribution for each pixel. This refines the position of the intensity maximum and determines the positions of particles with an inaccuracy of less than one-tenth of a pixel length [140]. The accuracy of the position determination in this method is highly dependent on the image properties and the tracking parameters used, which must be set manually [138].

2.3 Computer Simulations

Although this is a thesis with an experimental focus, the following chapters present results from computer simulations. These were mainly carried out by our collaborators. The author ran the Monte Carlo simulations of the Yukawa potential shown in Chapter 4. And used LAMMPS code to simulate the diluted systems of dipolar colloids in order to map the field strength between computer simulations and experiments in Chapter 7.

Computer simulations are a powerful tool in the investigation of colloidal systems. Studies that compare predictions from experiments with computer simulation data at the microscopic level are particularly important for investigating the fundamental mechanisms of collective behaviour of particles in physical systems [41, 52, 141].

We would like to present a few methods that were used in this thesis, namely molecular dynamics

(MD), event-driven (EDMD) and Monte Carlo simulations (MC). For the various colloid systems studied below, some methods are more suitable than others. More information about various techniques can be found here [142–144].

2.3.1 Molecular Dynamics Simulations

Molecular dynamics (MD) simulations offer a great way to analyse systems with continuous potentials. To do this, the time evolution of a system of interacting particles is predicted by solving Newton's equations of motion. In each time step, the equations are solved and the position of the particles is updated. This allows real-time dynamics to be investigated. We use a previously developed software package, LAMMPS [145].

Newton's equations of motion only considers the forces of the interaction potential, and the trajectories are deterministic. This approach is used for atoms, molecules, or dry granular media, i.e. systems without solvent. If Langevin dynamics are introduced, friction and random thermal noise are also added to Newton's law. Particles are in contact with a heat bath, the solvent, and the trajectories are stochastic. Colloidal systems can thus be simulated without taking any solvent molecules into account. In Langevin's overdamped limit (inertia is negligible), we speak of Brownian dynamics simulations (BD).

$$\frac{d\mathbf{r}(t)}{dt} = \frac{D_s}{k_B T}\,\mathbf{f}(t) \;+\; \sqrt{2D_s}\,\mathbf{R}(t), \tag{2.2}$$

where $\mathbf{r}(t)$ is the colloids positions at time t, D_s is the short-time self-diffusion coefficient, and $\mathbf{R}(t)$ is a Gaussian random noise. The movement is a balance between deterministic drift and random thermal noise. This enables direct simulation of the Brownian motion of colloids [142].

2.3.2 Event-Driven Simulations

A widely used method for investigating colloidal systems with a discontinuous potential, such as that of perfect hard spheres, is event-driven molecular dynamics. The simulation steps are not determined by a fixed time step, but rather by the occurrence of events in the form of collisions between the particles. In other words, instead of using small time steps, EDMD calculates when two particles will next collide. Between events, they move ballistically, i.e. in a straight line at

constant speed. At the event, the velocities are updated using the conservation law, i.e. assuming instantaneous elastic collision [142, 143].

EDMD reproduces the physical dynamics of hard spheres without taking the solvent into account and is particularly suitable for studying equilibrium configurations in hard-sphere systems. However, this technique is also effective for other systems with high density and discontinuous potentials, such as square wells [142].

2.3.3 Monte Carlo Simulations

In contrast to previous techniques, MC does not integrate the equation of motion, but samples configurations of the system according to the rules of statistical mechanics. It is one of the most important techniques for investigating the statistical physical behaviour of colloidal and soft matter systems and can be easily adapted to different thermodynamic ensembles and boundary conditions. The aim of MC is to generate states with probabilities proportional to the Boltzmann weight. MC does not produce physically meaningful trajectories, but the equilibrium properties of the system can be reliably traced. The simplest implementation is Metropolis-Hastings MC. This involves proposing a random move, in our case the displacement of a particle, followed by the calculation of the energy difference. If the energy is lower than that of the previous states, the move is accepted immediately. If the energy difference is positive and the previous state has low energy, the move is accepted with a probability proportional to the Boltzmann weight. Thus, correct equilibrium distributions are sampled. For hard spheres, where no potential energy exists, particle moves are accepted if no overlaps exist in the new configuration [142]. The HOOMD-blue package offers a simple implementation of MC with parallelisation options for faster simulation of large systems [146, 147]. For small step sizes, the MC reproduces the results of Brownian Dynamics [148, 149].

For many of our systems with low supersaturation, nucleation events are very rare. For the simulation techniques mentioned above, in which phase space is explored according to the natural rules of statistical mechanics (brute-force), these events can barely be observed on the time scale of the simulations [1, 38, 150]. Therefore, so-called advanced sampling schemes are used. In our case, Monte Carlo simulations with umbrella sampling, in which an order parameter is first selected. Along this reaction coordinate, the system is biased to sample previously very rare configurations. The bias is then mathematically removed and the correct free energy is recovered [142].

In one of the following chapters, we will determine the height of the free energy barrier for systems of

hard spheres, and use the number of particles n in the largest crystal nucleus as the bias parameter accordingly. Then, statistics are collected in ranges of n that would otherwise be inaccessible, and these biased distributions are stitched together to obtain the full free energy barrier [22, 36, 151, 152].

2.4 Structure Analysis

From confocal microscopy and computer simulations, we can extract particle-resolved data, from which we are able to calculate different observables describing the structure of the system under investigation. In the course of this work, we want to find underlying connections between the structure on a particle-based level and macroscopic behaviour of our systems. For this purpose, we want to examine two-point and higher-order correlations. In the following, we well introduce the famous radial distribution function, the topological cluster classification, and the bond orientational order parameter. We are aware that there are other measures that can be used to describe the structure, such as the three-particle correlation function or common neighbour analysis, but these are beyond the scope of this thesis.

2.4.1 Radial Distribution Function

Liquids do not exhibit a clear long-range structure in the way that crystals do. Instead, their microscopic properties are best described using spatially averaged quantities. One of the most fundamental of these quantities is the *pair correlation function*, $g(r)$. The function $g(r)$ represents the probability of finding a particle at a distance r from a test particle located at the origin.

For a system of N particles with potential energy $U_N(r_1, \ldots, r_N)$, the probability of a configuration in which n particles are found at positions $r_1, \ldots, r_n$ is given by

$$p^{(n)}(r_1, \ldots, r_n) = \frac{1}{Z_N} \int \cdots \int e^{-\beta U_N} \, dr_{n+1} \cdots dr_N, \tag{2.3}$$

where Z_N is the normalising configurational integral [153], defined as

$$Z_N = \int \cdots \int e^{-\beta U_N} \, dr_1 \cdots dr_N. \tag{2.4}$$

Assuming identical particles, we can define the n-particle density as

$$\rho^{(n)}(r_1, \ldots, r_n) = \frac{N!}{(N-n)!}\, p^{(n)}(r_1, \ldots, r_n). \tag{2.5}$$

In the simplest case, the single-particle density reduces to

$$\rho^{(1)} = \frac{N}{V} = \rho, \tag{2.6}$$

as expected, since the configurational integral cancels out. For an ideal gas, the particles are uncorrelated, so the two-particle density becomes

$$\rho^{(2)}(r_1, r_2) = \rho^{(1)}(r_1)\rho^{(1)}(r_2) = \frac{N(N-1)}{V^2} \approx \rho^2. \tag{2.7}$$

We may now define the pair correlation function as

$$g(r_1, r_2) = \frac{\rho^{(2)}(r_1, r_2)}{\rho^2}, \tag{2.8}$$

which quantifies the deviation from the ideal gas result [154]. For an isotropic liquid, the correlation depends only on the distance between r_1 and r_2, so that $g(r_1, r_2) = g(r)$. The radial distribution function for hard sphere systems with different volume fractions is shown in Fig. 2.2.

The calculation of the radial distribution function involves solving the Ornstein-Zernike equation [155]. In the case of hard spheres, an exact analytic solution has been obtained [156] using the Percus-Yevick approximation [157, 158].

2.4.2 Topological Cluster Classification

So far, we have only considered two-point correlations. Another way to describe the structure of colloidal systems is to analyse local arrangements of particles. Various methods are used for this, such as Voronoi tessellation [158], common neighbour analysis [160] and bond orientational order [161]. We to introduce a different approach that can be used to identify higher-order clusters in the samples. The so-called topological cluster classifier (TCC) finds minimum-energy clusters for different numbers of isolated particles for various potentials, such as the Lennard-Jones potential, Morse potential and dipolar interactions between the particles [162, 163]. Renderings of different clusters for the different models are shown in Fig. 2.3. Although clusters that minimise potential

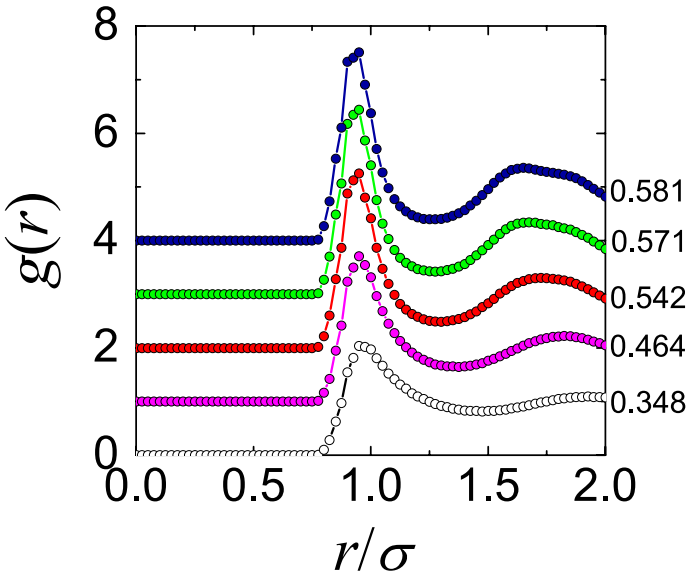

Figure 2.2: Radial distribution function of a hard sphere fluid at different volume fractions. Points represent experimental data. Lines come from computer simulations with experimental polydispersity. Reproduced from [16, 159]

energy do not exist in systems of hard spheres, previous studies have found that these higher-order assemblies also play an important role in freezing processes or glass formation in systems of hard spheres [34, 164, 165].

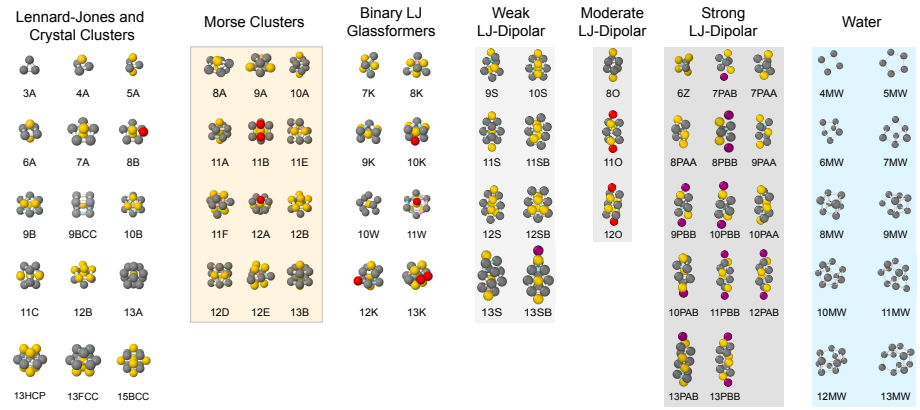

Figure 2.3: Overview of minimum-energy clusters that can be identified with the TCC for different model systems, from Lennard-Jones, Morse, Binary Lennard-Jones, Lennard-Jones and dipolar interactions and water.

The TCC is based on a modified Voronoi tessellation, in which each particle is assigned a volume consisting of the points that are closest to that particle. Voronoi polyhedra are constructed around each particle, and two particles are recognised as neighbours if they share a surface of the Voronoi polyhedron and the line between their centres passes through it. In addition, a threshold value is introduced, which determines the maximum distance between two particles at which they can no longer be identified as neighbours.

In the next step, the shortest path rings containing 3, 4 or 5 particles are identified from the neighbours. This means that two particles can only become part of a ring if the shortest path through the network spanned by the connections of the particle centres connecting the two particles is also part of the ring [166]. Another parameter determines the extent to which a 4-membered ring can be deformed before it is identified as two 3-membered rings sharing one side. Then individual particles are added to the identified rings, thereby identifying larger formations.

The TCC has been successfully used in various systems to link the particle-based structure with macroscopic phenomena. For the system of hard spheres, this allowed a connection to be made between the inhibition of nucleation in sedimenting samples and the increased population of fivefold symmetry clusters in those systems [27]. Other studies were able to explain the phenomenon of polymorphic selection and the tendency of hard spheres to crystallise into the FCC crystal structure by the increased occurrence of clusters that exhibit fluid and FCC-like symmetries, thereby reducing the surface free energy [52].

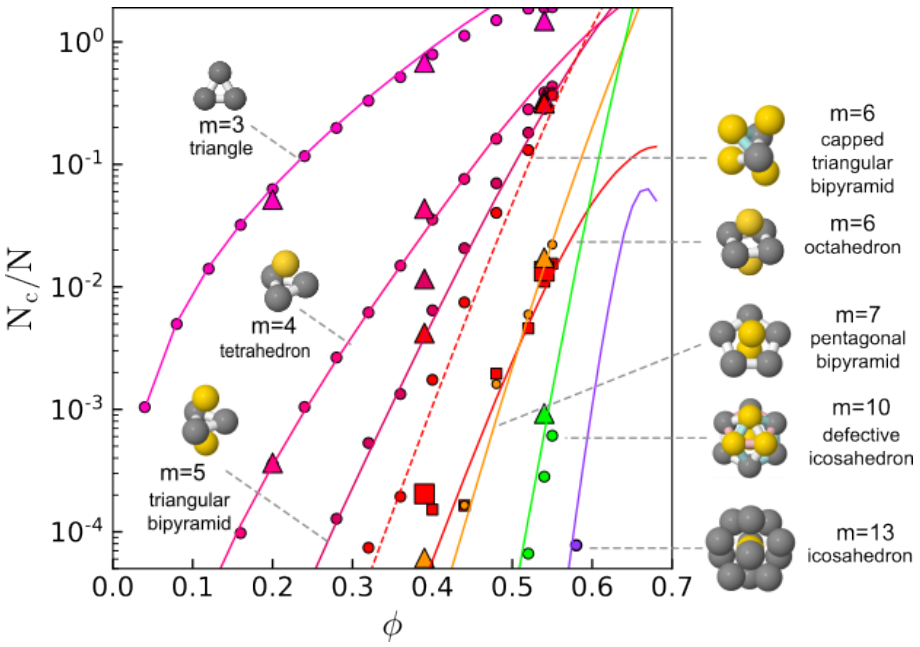

Figure 2.4: Population of higher-order cluster in the hard sphere fluid as a function of Volume fraction. Cluster contain $m = 3$ to 13 particles. Lines come from theoretical predictions [167]. Small data points represent results from monodisperse Monte Carlo simulations. Large data points are from confocal microscope experiments with 2 μm PMMA particles. Simulation data and experiments were analysed with the topological cluster classification (TCC) [168]. Reproduced from [16]

For us, the TCC is also important for mapping experimental systems onto computer simulations. In contrast to the shape of $g(r)$ (Fig. 2.2), the cluster population is more dependent on the state point of the system. Figure 2.4 shows the population of higher-order clusters consisting of $m = 3$

to 13 particles. Data from experiments are compared with computer simulations and predictions from morphometric theory. In the following chapters, we will use both 2-point correlations and higher-order correlations in the form of cluster populations to map our experimental systems onto computer simulations.

2.4.3 Bond Orientational Order Parameter

The core concept is to represent the local arrangement of nearest neighbors through spherical harmonic functions Y_{lm} of Ten Wolde et al. [169],

$$q_{lm}(i) = \frac{1}{N(i)} \sum_{j=1}^{N(i)} Y_{lm}(\hat{r}_{ij}), \tag{2.9}$$

where $N(i)$ is the number of nearest neighbour particles and l describes the number of specific arrangements of the neighbours, and indicates the symmetry of the spherical harmonics. There are various methods for obtaining nearest neighbours, such as a cut-off distance or Voronoi tessellation [170, 171]. We choose a parameter-free approach, the solid-angle based nearest-neighbor algorithm (SANN) [172]. In SANN, each possible neighbor is given a solid angle, and the cutoff radius is chosen so that the total solid angle adds up to 4π. A commonly used choice is $l = 6$, as it is well suited for identifying fcc- and hcp-like structures, since the hexagonal planes in these crystal lattices exhibit six-fold symmetry. To identify connected particles, we apply the dot-product cutoff value of $q_6(i) \cdot q_6(i) = 0.7$ and consider a particle to be in a crystalline environment if the number of solid-like neighbours is at least 5.

Chapter 3

"Colloidoscope": Deep Learning and Particle Tracking

The development, training and validation of the tracking routine was carried out by Abdelwahab Kawafi as part of his PhD thesis [173]. The benchmarking and comparison with a conventional tracking routine for a system of larger colloids explained in this chapter was performed by the author. The complete code with documentation is publicly available on GitHub: `https://github.com/wahabk/colloidoscope`. *Parts of this chapter have been published in [174].*

The overarching topic of this thesis is the investigation of underlying processes of crystal nucleation with 3D confocal microscopy, the so-called particle-resolved studies (PRS) [16, 17, 44, 175]. With this type of experiment, particle-resolved data provide insight into the systems under investigation that would not be accessible through, for example, light scattering experiments [126]. Therefore, particle tracking plays a crucial role. High-quality data are needed at the single-particle level to be able to draw reliable conclusions from the experiments. Especially for the identification and analysis of higher-order structures, avoiding missed particles, false positive identifications, and localisation uncertainties is crucial. In addition, the robustness against photobleaching, the intensity decay throughout an experimental measurement, plays an important role. Higher robustness means longer measurements and with that better statistics.

In this chapter, the output of the novel deep-learning routine “Colloidoscope” (U-net) [174] is analysed and compared to “Trackpy” (TP) which is based on the conventional tracking algorithm developed by Crocker and Grier [138]. The neural network used is described in detail, as is how it was trained and how the training data sets were produced.

3.1 Deep Learning for Particle Tracking

In the past, particle tracking was done mainly by conventional tracking routines based on the work of Crocker and Grier [138]. This novel routine developed by Abdelwahab Kawafi is a deep learning pipeline that uses a 3D residual U-net architecture to improve the results of particle tracking in terms of the number of tracked particles and localisation uncertainty [174].

The approach of using deep learning for computer vision is not new [176, 177]. Convolutional neural networks are often used for this purpose, which, compared to fully connected layers of networks, have a smaller number of connections and thus fewer parameters to train. Frequently used methods include semantic segmentation (binary) [178], in which each pixel of the image to be examined is assigned to a specific category, in this case foreground (particles) and background (solvent). In our case, we use heatmap regression, which is particularly advantageous in high packing density

regimes because labels from binary classifications can overlap, leading to misidentifications and lost particles.

A problem with applying deep learning approaches to particle tracking is the deficiency of a ground truth on which to train the model. In the case of particle tracking, the ground truth is an experimental image and corresponding particle positions, which are not known in experimental systems. It is clear that it is not easy to produce such training data sets, especially because deep-leaning applications in other fields often rely on manual labelling of data by humans.

One could use self-supervised learning based on the geometric symmetries of the particles [179], or use generative adversarial neural networks (GANs) to produce artificial training data sets [180]. However, in this work, we want to simulate datasets by creating amorphous configurations with hard sphere Monte Carlo computer simulations and convolving them with kernels such as the point spread function (PSF) [181]. This gives us complete data that allow us to quantify the output of the tracking and the influence of imaging parameters.

The working principle is shown in Fig. 3.2. The U-net labels the experimental image as a Gaussian heatmap. After that a conventional method, in our case TP, has to be used to extract the particle position with sub-pixel resolution.

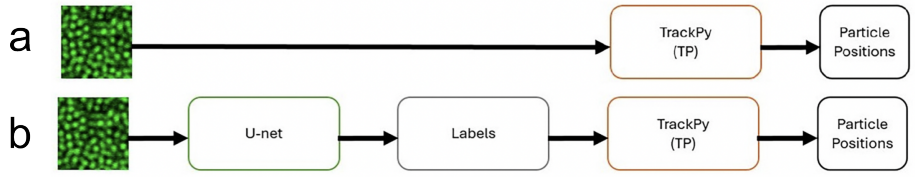

Figure 3.2: (a) Operating Principle of TP. (b) Operating Principle of “Colloidoscope”. A U-net labels the image and TP extracts the particle positions with sub-pixel resolution. Reproduced from [174].

Finally, two fundamental variables must be defined that quantify the success of particle tracking.

- **Recall** describes the proportion of particles in the system that were successfully detected.
- **Precision**, on the other hand, refers to the proportion of detected particles that correspond to real particles in the sample.

3.2 Model Training

“Colloidoscope” is a pre-trained model available on GitHub (`https://github.com/wahabk/colloidoscope`).

The package can be installed and applied to experimental data without system-specific adaptations, as the model was trained to account for substantial variability in particle sizes and image characteristics. Here we explain in detail how the training was realised.

3.2.1 Network Architecture

We use a simple network with 3D U-net architecture [182] and a loss function L_1. The encoder blocks are used as residual blocks to implement deeper models. To make data management more efficient, we use tiling, in which each image is divided into small pieces during training. This allows the model to be trained with larger batch sizes and also enables larger experimental images to be analysed later on. In addition, augmentation, such as zooming or flipping, was used to create realistic variations of the training data, which prevent overfitting and improve generalisation.

3.2.2 Training Data Set

For the training, amorphous configurations of particle positions are created using hard sphere Monte Carlo simulations at high volume fractions (up to $\phi = 0.55$) [142, 144]. A configuration with a low volume fraction is produced in a large simulation box. The box is then continuously reduced in size, with the particles performing random displacements and not being allowed to overlap until the desired volume fraction is reached. The data sets were produced using Hoomdblue [147, 183].

In the next step, the imperfections of the experimental images are transposed onto the simulated coordinate. Characteristic values describing the experimental parameters are used for this purpose. The signal-to-noise ratio (SNR) is defined by the mean brightness of the foreground $f_{\bar{x}}$ and the background noise f_s

$$\mathrm{SNR} = \frac{f_{\bar{x}}}{f_s}. \tag{3.1}$$

However, this value is not particularly meaningful, especially in confocal microscopy, where the particles have different brightnesses. Instead, we use the contrast-to-noise ratio, which is defined by

$$\mathrm{CNR} = \frac{|f_{\bar{x}} - b_{\bar{x}}|}{b_s}, \tag{3.2}$$

where $b_{\bar{x}}$ describes the mean brightness of the background. The CNR is a useful measure for image quality, specifically in cases where laser illumination is important for photobleaching. These SNR and CNR values are later used to investigate the influence of various experimental parameters on the results obtained with “Colloidoscope”.

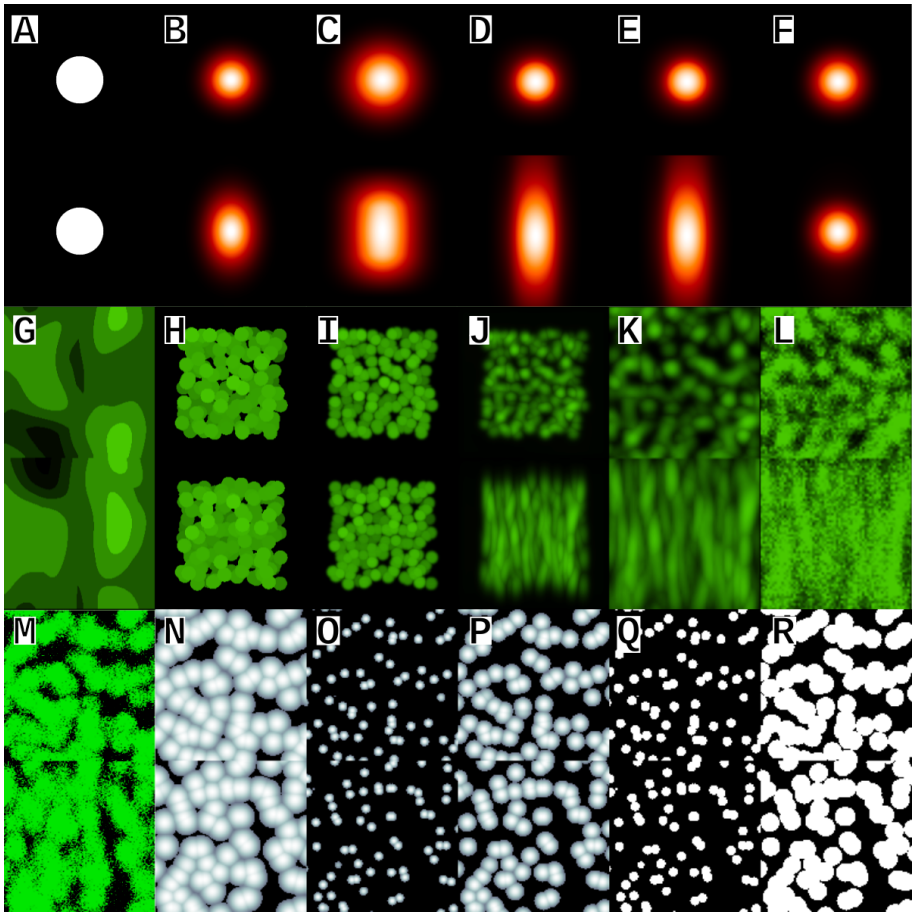

Figure 3.3: The process used in “Colloidoscope”. Red: PSFs. Green: colloids, White: training labels. In each case, the xy plane is shown followed by, lower, an xz cut.
(A)–(F) Approximations of confocal and STED PSFs. (A) Simulated particle with $\sigma = 10$ pixels. (B) The particle convolved with a Gaussian kernel of (9,5,5) (z,x,y). (C) A simulated particle of size 200 nm using the least-squares Gaussian method. (D) A simulated particle of size 200 nm using a Huygens STED XY PSF. (E) A simulated particle of size 200 nm using a Huygens STED 50XY 50Z PSF. (F) A simulated particle of size 200 nm using a Huygens STED Z PSF.
(G)–(L) Colloid simulation steps. (G) Background. (H) Drawing spheres. (I) Aliasing. (J) Convolved PSF. (K) Crop. (L) Noise.
(M)–(R) Gaussian heatmap regression and semantic segmentation for particle detection. (M) A simulated volume of colloids. (N) Gaussian heatmap label with varying radius $r = s$. (O) Gaussian heatmap with constant radius $r = 4$. (P) Gaussian heatmap with constant radius $r = 7$. (Q) Semantic labels of with varying radius $r = s$. (R) Semantic labels with constant radius $r = 4$. Reproduced from [174].

After SNR and CNR are defined, the fluorescent cores of the particles are superimposed on the PSFs. The shape of the PSF is defined by the excitation and emission wavelengths, the refractive index of particles and solvent, the numerical aperture and magnification of the lens, and the pinhole size. A

straightforward approach to recreating a PSF is to use a Gaussian blur (Fig. 3.3(B)) stretched in the z-direction, or the closely related least-squares Gaussian method shown in Fig. 3.3(C) [184]. Here, however, we use PSFs produced by Huygens Professional version 22.10 software (Scientific Volume Imaging, The Netherlands), which provides PSFs for confocal and STED microscopy. Examples are shown in Fig. 3.3(D)-(E)

The second row of Fig. 3.3(G)-(L) summarises the creation of the simulated experimental images (64 pixels cubed) for training the network. First, an image with double resolution is created, which is later downsampled by a factor of 2 to introduce aliasing. Padding is also added to prevent cutting off filters or the PSF at the edge of the image. Perlin noise [185] defined by the CNR is used to mimic the background noise of the image (Fig. 3.3(G)). Perlin noise refers to a type of gradient noise, which, in contrast to purely random noise, is characterised by a smooth transition between neighbouring values, which recreates the typical background noise of microscopic images.

Then the particle images are produced using the coordinates and radii generated by computer simulations (Fig. 3.3(H)).

The image is then coarsened or zoomed in to achieve aliasing (Fig. 3.3(I)), followed by convolution of the particle images with the PSFs (Fig. 3.3(J)). The stretching of the intensity distribution along the z-direction typical for confocal and STED microscopy can be clearly seen.

Now the edges are cut off (Fig. 3.3(K)) and a Gaussian noise is superimposed to simulate the foreground noise (Fig. 3.3(L)).

Figure. 3.3(M) shows a different simulated volume of colloids, from which, training labels can be drawn. There are various approaches for producing label images, from Gaussian heatmaps with varying or constant radii to semantic labels with different radii, which can improve tracking in polydisperse systems. For semantic segmentation, i.e. the binary classification of all pixels into background and foreground, labels of different particles may overlap, leading to misidentifications. Also, a smooth heatmap approach enables the use of a L_1 loss function for the model. After testing various approaches, we decided to generate a Gaussian around each particle to draw the label image. This completes the data sets used to train the network.

After training the model on different image properties, “Colloidoscope” acts as a de-noiser in the particle tracking process. Heatmaps are produced that contain information about the particle positions. In the final step, the coordinates are extracted using TP with a single parameter, the particle diameter.

3.3 Validation of the Model

Validating the trained model on experimental data is not straightforward, as the number of particles and their positions are not known *a priori* [186]. Therefore, we first give the physical definitions for the previously introduced values of *Recall* and *Precision*. We can then perform a validation using more simulated training data, where the positions and number of particles are known.

This will be followed by validation with various experimental systems using the radial distribution function $g(r)$ and the number of tracked particles before we perform a detailed analysis with systems of larger PMMA particles, in which we will quantify the output of "Colloidoscope" more precisely by comparing populations of higher-order structures of the experiments and computer simulations.

3.3.1 U-net Validation with Simulated Data

In object detection, accuracy is often measured using average precision (AP), which depends on how well bounding boxes and ground truth boxes match. The match is typically determined using intersection over union (IoU). In our case, for the simulated data, the diameters of the particles are known and we are interested in the distance between the predicted particle centre and the true particle centre. Therefore, we calculate the distance matrix (normalised by the diameter of the particle in pixels).

$$D_{ij} = |p_i - \hat{p}_j|, \tag{3.3}$$

where p_i is the true position of the particles and $\hat{p}_j$ is the predicted position. The mismatch matrix can then be calculated by considering predictions where the distance is less than a certain percentage of the diameter τ to be a "match".

$$M_{ij} = \begin{cases} 1 & \text{if } D_{ij} > \tau \\ 0 & \text{if } D_{ij} \leq \tau \end{cases} \tag{3.4}$$

In our case $\tau = 50\%$ and AP becomes AP_{50}. Now we can define

$$\text{Precision} = \frac{1}{\hat{N}} \sum_{j=1}^{\hat{N}} \left(1 - \prod_{i=1}^{N} M_{ij} \right) \tag{3.5}$$

and

$$\text{Recall} = \frac{1}{N} \sum_{i=1}^{N} \left(1 - \prod_{j=1}^{\hat{N}} M_{ij} \right), \tag{3.6}$$

where N is the true number of particles and $\hat{N}$ is the predicted number of particles.

The U-net can now be validated using more than 20 data sets with different simulation parameters, such as noise and particle diameter. For the analysis, one parameter was changed, while the others were kept constant in an optimal regime in which small changes had no influence on the predictions of the U-net. This allows the influences of the individual parameters to be examined separately. The results are shown in Fig. 3.4. It can be seen that the U-net produces perfect precision, like TP, for all parameters. However, the U-net has a higher recall, i.e. more tracked particles, compared to the conventional approach with TP. This is of great importance for the analysis of experimental data because the value is related to the control parameter, the volume fraction ϕ. Furthermore, in the course of this work, we will analyse the higher-order structure of the colloids using particle-resolved data. Missed particles have a particularly critical influence on the calculated population. The U-net performs significantly better, especially for colloids with low contrast and brightness. Note that TP would also be able to identify particles in this parameter range, but this would require adjusting many tracking parameters. “Colloidoscope”, on the other hand, offers a simpler approach to the user that does not require any system-specific parameters to be adjusted.

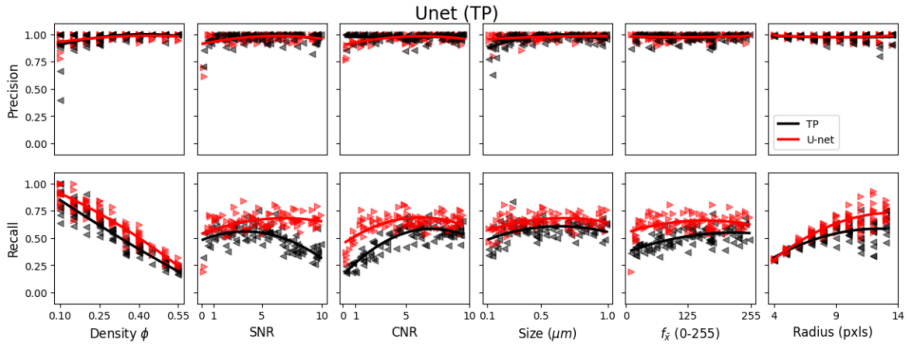

Figure 3.4: U-net precision and recall (AP_{50}) against simulation parameters. Reproduced from [174].

3.3.2 U-net Validation with Experimental Data

We will now proceed with the validation of the U-net using various experimental systems. Here, the ground-truth deficit character of the tracking problem becomes apparent once again. The number of particles in the experimental image to be examined is unknown, and it is not possible to determine the distance matrix. Therefore, we use the radial distribution function $g(r)$ for validation and compare the number of identified particles with the volume fraction of the sample, determined by weighing the components during sample preparation.

The shape of the $g(r)$ is uniquely determined for an isotropic fluid with spherically symmetric pairwise interactions and can be predicted from theory with high accuracy in many cases [187]. We can use the shape to compare the results of “Colloidoscope” and TP and draw further conclusions about the quality of the tracking. In experiments and computer simulations, in addition to the interaction potential and the state point of the system, polydispersity, localisation uncertainty and *Precision* also have an influence on the shape of the curves. False positive identifications lead to contributions in $g(r)$ smaller than the diameter of the particle $r < \sigma$, and polydispersity and high localisation uncertainties result in a lower and broader first peak.

Figure. 3.5 shows the results of the U-net and TP for different experimental systems. We analysed small Silica particles ($\sigma = 560$ nm) and small PMMA particles ($\sigma = 315$ nm) at a high volume fraction ($\phi > 0.55$) and larger Silica particles ($\sigma = 1.2$ μm) at a smaller volume fraction ($\phi = 0.2$). Systems with small particles and high density pose a particular challenge for conventional tracking methods. For small silica particles, the U-net finds significantly more particles (46%) than TP (36%). The percentages were determined by calculating the fraction of tracked particles from the estimated true number of particles, which was obtained by weighing the components during sample preparation to determine their correct volume fractions. Interestingly, “Colloidoscope” also improves recall for the analysis of the same system after image deconvolution. In summary, it can be seen that U-net improves the recall for all systems. Significantly more particles are identified compared to TP. It is important to note that there are no signs of false positives, i.e., there are no contributions for $r < \sigma$. It is also noteworthy that U-net produces a higher first peak in all cases, indicating a lower localisation uncertainty.

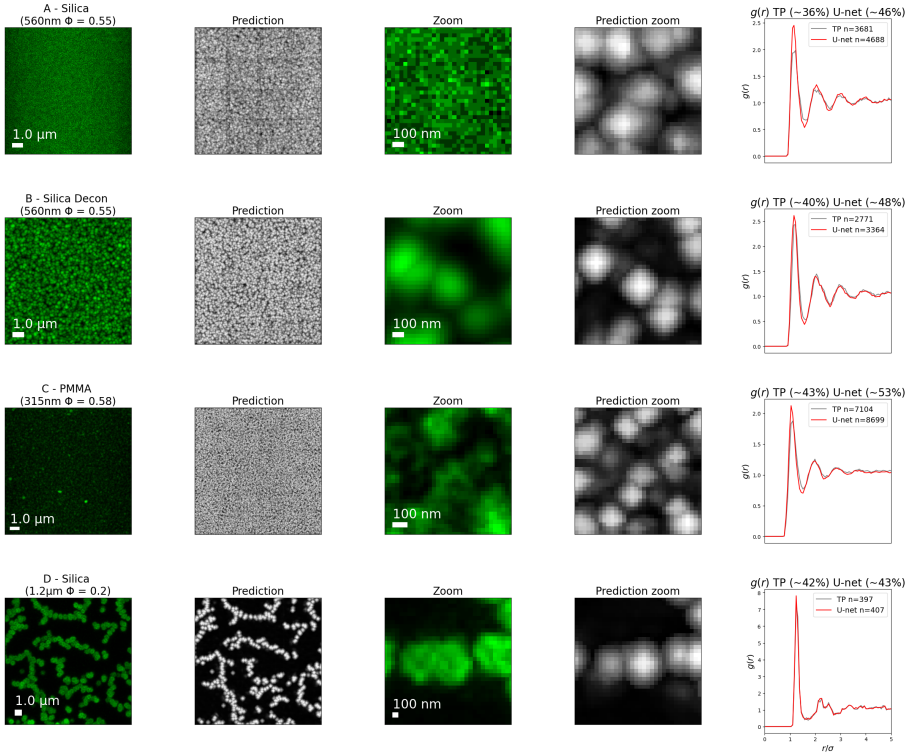

Figure 3.5: Experimental predictions using TP as a postprocessing method for a U-net. (A) and (B) Experimental images of colloids. (B) Deconvolved (Decon.) volume of (A). C, D, other experimental systems. The images are shown as maximum projections followed by the model's predicted labels. A zoomed in maximum projection of a 32 cubed volume is taken around a random particle with the corresponding prediction shown on the right-hand side. The approximated percentage detected is derived from the experimentally prepared and predicted volume fractions. Reproduced from [174].

3.3.3 U-net Validation with Higher-Order Structural Measures

After general validation of the trained model with additional simulated data and various experimental systems consisting of relatively small particles, for which only about half of the identifications are possible, we will now turn to a system that is significantly simpler for particle tracking. The high-density system consists of large PMMA particles, in which more than 95% of the particles can be identified using conventional tracking methods. The improved recall and statistics enable us to analyse the tracking results more accurately by comparing the population of higher-order structures identified by the TCC [162] from computer simulations (ground truth), U-net and TP.

We will first introduce the experimental system in more detail and then analyse the effect of photobleaching and the quality of the tracking results.

Validation Methods

We use a model system of colloidal hard spheres consisting of PMMA particles (diameter of 2 μm) with 4% polydispersity in a density and refractive index matched mixture of Decalin, Tetralin and CHB with volume fraction, $\phi = 0.525$. TBAB salt was added to the solvent to screen residual charges on the surface of the particles, which otherwise could lead to a softening of the interaction potential. This hard sphere system is well characterised and easily accessible to computer simulations. We want to analyse the experimental data with "Colloidoscope" and different parameters in TP and compare to the "true" values we get from computer simulations. This allows us to quantitatively compare the different routines against a ground truth.

For "Colloidoscope" only one parameter, the approximate particle diameter of 5 or 7 pixels and no image processing to increase signal-to-noise ratio is used. In the case of TP, to guarantee a fair comparison, we compensate the intensity loss in the z-direction of the microscopic image and after that apply a Gaussian filter to smooth the image and avoid misidentifications. With pre-processing the number of tracked particles increases, and the localisation uncertainty is minimised. In addition, compared to "Colloidoscope" an anisotropic tracking diameter is used to compensate for the elongation of the intensity in the z-direction of the image of a single particle. This distorted representation in the microscopic image can lead to two particles that lie on top of each other being tracked as one particle. This type of misidentification can cause a peak in the radial distribution function, $g(r)$ at values smaller than the particle diameter ($r < \sigma$). The values used for the anisotropic diameter are either 5 pixels in the xy-direction and 7 pixels in the z-direction, or 7 pixels in the xy-direction and 9 pixels in the z-direction.

In the following, the novel tracking routine will be benchmarked by comparing the number of tracked particles (volume fraction) throughout a single measurement despite the effect of photobleaching, the shape of the radial distribution function, which depends on the tracking uncertainty, and the population of higher-order clusters.

Photobleaching

Photobleaching is the irreversible loss of fluorescence of the sample under investigation due to illumination with excitation laser light. Figure 3.6(a) and (b) show the influence of photobleaching on a slice of a 3D confocal image over the course of a 32 frames measurement (approx. 3 min). It determines the duration of the measurement and the maximum possible laser intensity which

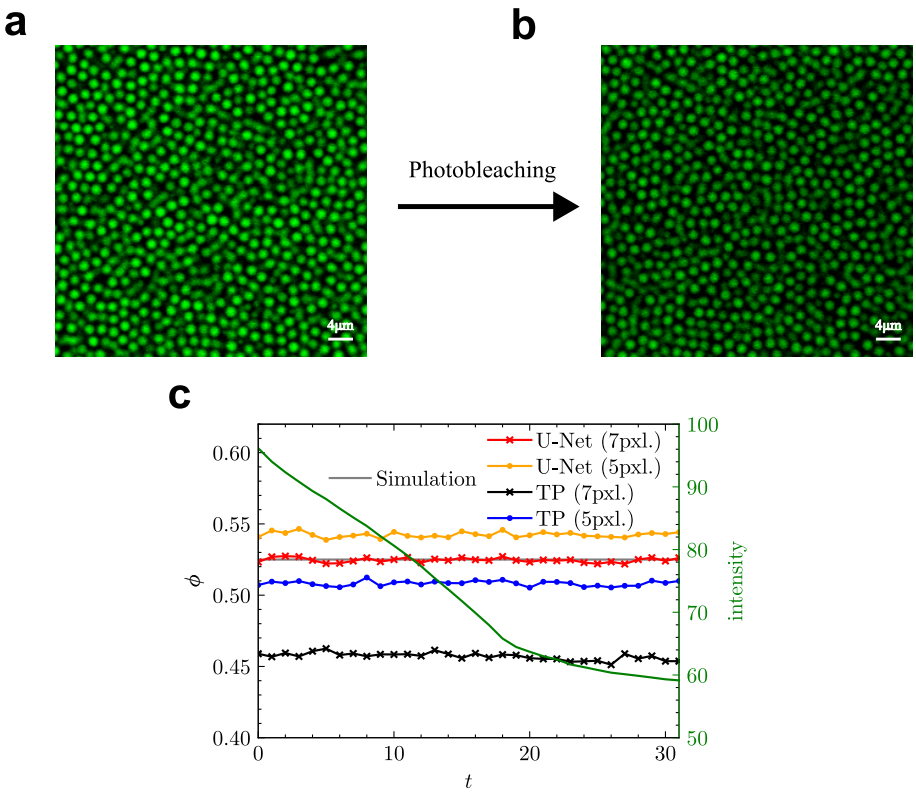

Figure 3.6: Photobleaching in a confocal image and influence on particle tracking. (a) and (b) The effect of consecutively imaging a volume of colloids for 32 frames. (c) Quantified intensity (brightness) of the 32 images, with the predicted volume fractions of the U-net and TP (ground truth $\phi = 0.525$).

influences the resolution of the microscopic image and with that the outcome and quality of the tracking routine. A tracking routine with high robustness against the influence of photobleaching enables longer measurements with higher quality and more statistics.

Figure 3.6(c) shows the volume fraction calculated by counting the tracked particle and the averaged intensity, which falls from approximately 98 to 60 in the 8-bit image over the measurement period. It is clear that with the smaller tracking diameter of 5 pixels “Colloidoscope” is overestimating the volume fraction by a couple percent, due to misidentifications. The approach with a diameter of 7 pixels, on the other hand, tracks 100% of the particles and reproduces the correct volume fraction ($\phi = 0.525$). It tracks more particles than either approach of TP and therefore shows significantly better efficiency. As expected, TP with a smaller diameter of 5 pixels tracks more particles ($\phi = 0.51$) than the approach with a diameter of 7 pixels ($\phi = 0.46$). This translates to a loss of approximately 150 particles between the two.

In conclusion, “Colloidoscope” outperforms the conventional approach with optimization and processing of the microscopic image in terms of the number of tracked particles, which has a great

influence on the identification of the higher-order clusters as we will see in Chapter 3.3.3.

Radial Distribution Function

The shape of the radial distribution function $g(r)$ is determined by the state point of the system, the polydispersity (width of the particle size distribution) and the localisation uncertainty, or error in the positions of the particles. By comparing the height of the first peak, we can draw conclusions about the quality of the outcome of “Colloidoscope” and TP.

Figure 3.7 shows the $g(r)$ curves for computer simulations and the different tracking routines. The height of the first peak is determined by the localisation uncertainty of the tracked particle positions. Both “Colloidoscope” approaches and TP with the larger diameter of 7 pixels produce almost identical $g(r)$s and agree very well with the computer simulations, which indicates a small localisation uncertainty. However, the TP approach with the smaller diameter of 5 pixels has significantly lower precision, which can be seen from the smaller first peak.

Taking into account the number of tracked particles shown in Fig. 3.6(c) a trade-off between precision and recall arises for the conventional tracking routine. For “Colloidoscope” the high precision approach with 7 pixels also reproduces the correct number of particles.

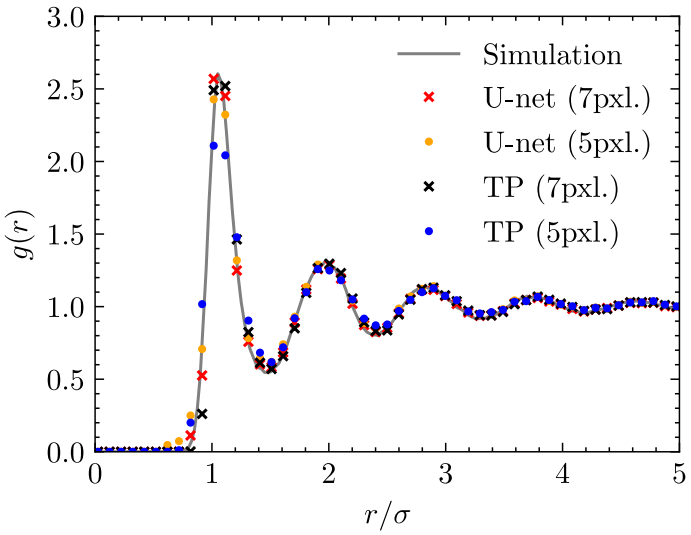

Figure 3.7: Radial distribution function for different parameters in “Colloidoscope” (U-net) and TP, compared to ground truth from computer simulations

Population of Higher-Order Structures

So far, we have considered pair correlations of particles using the radial distribution function $g(r)$. However, higher-order structural correlations provide a more detailed probe of the quality of particle tracking when benchmarked against simulation data. Correctly classifying these structures requires tracking the correct number of particles with low localisation uncertainty. For example, in the case of the fcc cluster, a failure to identify one particle out of 13 will result in the cluster not being detected. The same applies to a particle that is localised with greater uncertainty. We calculated the averaged population of different cluster types identified from coordinates produced by “Colloidoscope” and TP and compared them to hard sphere simulation data.

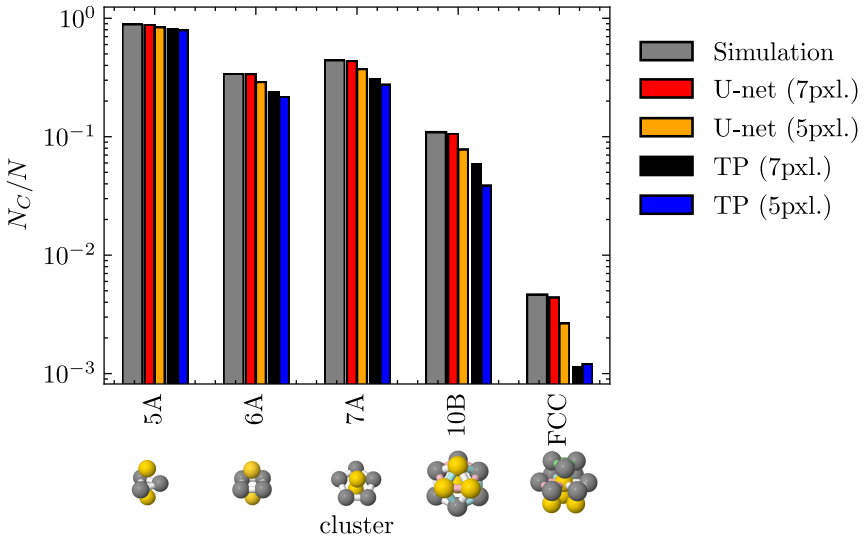

Figure 3.8: Topological cluster classification (TCC) results for different parameters in “Colloidoscope” (U-net) and TP. The averaged cluster population is compared to the ‘ground truth’ from computer simulations.

Here we consider five clusters each consisting of m particles relevant to the system in question. These are the triangular bipyramid (m = 5), the octahedron (m = 6), the 7-membered defective icosahedron (m = 10) and the face-centred cubic crystal (m = 13). Figure 3.8 shows that “Colloidoscope” with a particle diameter of 7 pixels matches the cluster population of the simulation, maintaining a closer match than TP. Both TP approaches deliver comparable results, which can be explained by a similar influence of recall and precision on the cluster population. In one case more particles are tracked with lower localisation uncertainty and in the other case it is the other way round. Unidentified particles and particles tracked with high uncertainty influence the population of higher-order structures in a similar way.

From the comparison of populations of higher-order structures one can say that “Colloidoscope”

outperforms the TP approaches with different particle diameters during the tracking for all cluster sizes, matching the structure of the simulation accurately.

3.4 Conclusion

We developed a deep learning pipeline employing a 3D residual U-net architecture to improve the results of particle tracking. The network was trained on high-density amorphous configurations produced by hard sphere Monte Carlo computer simulations. The particle positions were convolved with noise and different PSFs to mimic the experimental conditions. After successful training of the U-net, the results were first validated with simulated data by considering *Precision* and *Recall*. We found that the “Colloidoscope” tracks more particles without false-positive identifications, especially in the regime of high SNR and low brightness.

We moved on to validate the U-net with different experimental systems of small particles and high volume fraction. We again found that the deep learning approach identifies more particles with smaller localisation uncertainty.

After that, we considered an experimental system of larger PMMA particles. Here we analysed the output of “Colloidoscope” with computer simulations and TP by analysing the population of higher-order structure. We found that comparing the results for the number of particles tracked and the localisation uncertainty derived from the quantities shown in Fig. 3.7 and 3.8, one can see that for TP there is a trade-off between the number of particles and the localisation uncertainty with which they are tracked. It opens an optimisation space for every parameter that can be changed in the TP routine. This ranges from the experimental settings during image acquisition, to image preparation, to the selected particle diameters in TP.

In summary, it can be said that TP can probably reproduce the particle positions produced by “Colloidoscope”. However, this requires careful fine-tuning of all parameters and probably post-processing in the form of manual filtering. In the test case we have considered, hard spheres, it is straightforward to compare against simulation data. In general, this is not always possible. This brings us to the question of how to actually know which parameters give “more correct” coordinates in the case of TP. An obvious quantity to tune against is the volume fraction. That is to say, to adjust the parameters until the desired volume fraction is obtained. One drawback of this approach is that the volume fraction itself is typically not known to high accuracy, with relative errors of 6% being routine [23, 24] (although improvements have been made very recently [188]). As discussed

above, the radial distribution function g(r) has limitations in assessing tracking quality, although higher-order correlations can shed more insight [189]. Overall, such parameter tuning can lead to subjective results.

Chapter 4

Free-Energy Barrier of Precritical Nuclei in Hard Spheres

This project was carried out in collaboration with Frank Smallenburg and Antoine Castagnède from University Paris Saclay. They are responsible for the majority of the computer simulations and developed the code to identify crystal nuclei. The author carried out the computer simulations for the Yukawa potential, all experiments and analysed all the data. Parts of this chapter have been published in [41]

As described above crystallisation is a phenomenon surrounding us in our everyday life. From aerosol crystallisation being the reason for huge uncertainties in weather predictions to pharmaceutical implications. Especially for industrial pharmaceutical production, crystallization plays a major role. Controlled crystallization is used to purify the active ingredients and remove impurities. Melting, the inverse process, plays a role in bioavailability. If the ordered structure of the active ingredient does not melt in a suitable place in the body, the effect may be missed. Finally, often the more stable crystalline form of the active ingredient is used to make the medication more durable. Overall, it seems that the crystallization process for a wide range of materials should be understood and well predicted. But surprisingly that is not the case [1, 2].

We see discrepancies in predictions of the nucleation rate of many orders of magnitude in a variety of different systems. The reason lies in the nature of the nucleation process itself. Due to its rare-event character and microscopic size in time and space, it is difficult to capture in experiments and difficult to access for computer simulations [1, 21].

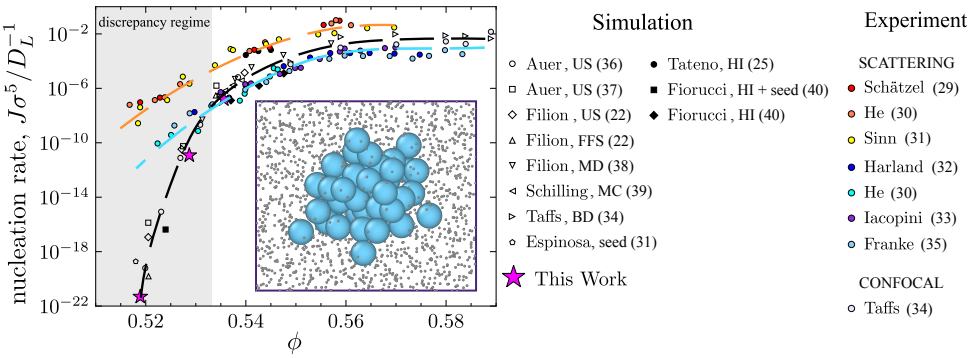

Figure 4.1: Reduced nucleation rates from experiments [29–35] and computer simulations [10, 22, 25, 34, 36–40]. Experiments are divided into two branches. Upper branch (orange) shows results of experiments without density matching, lower branch (blue) with approximate density matching and almost no sedimentation. Inset shows rendering of coordinates from experimental system ($\phi = 0.54$) with pre-critical nuclei (green) identified with q_6 bond-orientational order parameters of Ten Wolde [169]. Liquid particles (grey) are depicted smaller

Classical models of water, for example, show a discrepancy that can be attributed to inaccuracies in the thermodynamic properties [11] and we find a similar situation in electrolyte solutions [190]. However, there is even a discrepancy between different implementations of the same computational model and comparisons with experimental data are only possible if the state point of simulations is massively rescaled [191, 192].

4.1 The Hard Sphere Nucleation Rate Discrepancy

In this work, the crystallization is investigated using colloids. The advantage of these model systems is that they follow the same laws of statistical physics, but in contrast to atomic systems, can be imaged in real space and time, with confocal microscopy due to their larger size [16–18]. Their simple, classical interactions mean that they are also easily accessible for large-scale studies with computer simulations [15]. Particle-resolved data from experiments and simulations can then be used to gain insights into the details and underlying mechanisms of crystallisation processes [19]. Again, it can be assumed that for these systems, good agreement should be found in the nucleation rates of experiments and simulations. But even for the simplest and most studied model system of hard spheres we find a very large discrepancy [16, 20–22] as can be seen in Fig. 4.1. This discrepancy is troubling for various fields of research because it exists between experiments and data points produced by rare event sampling applications. These biased simulation techniques are used in various fields from molecular science to biochemistry [152, 193, 194]. A direct comparison between simulation and experiment is therefore all the more important.

As described above in Chapter 1.3.2 on the general phase behaviour of colloidal hard spheres, this system undergoes an entropically driven phase transition at the freezing volume fraction $\phi_{\text{freezing}} = 0.492$. Here, the nucleation rate vanishes, but increases dramatically with a further increase in the chemical potential. Figure 4.1 shows the nucleation rates from experiments and computer simulations for different values of ϕ. Two regimes are clearly recognizable. For large supersaturation, experiment and simulation are in good agreement. Here the crystallization process is fast. With decreasing supersaturation, where the crystallization process is slow, the discrepancy between experiments and computer simulations widens to more than 10 orders of magnitude. This area is highlighted in grey in Fig. 4.1 and is referred to below as the discrepancy regime. It is important to note that the discrepancy exists between biased simulations and experimental data obtained from light scattering experiments. Here, the size of crystal nuclei are measured indirectly from the diffraction patterns [16, 21]. In the recent past, however, experiments have been carried out with larger particles that are visible under the microscope [18, 195]. From the particle-resolved data, nucleation rates were determined (pale light blue) that are in the range of large supersaturation and in good agreement with the simulation data [34]. There are no data from confocal microscopy in the discrepancy regime because it was not accessible for this type of experiment until now. The kinetics of colloidal spheres are characterized by the Brownian time, i.e. the time it takes for an isolated sphere to diffuse its own radius. This time scale scales with the particle diameter cubed. The particles used in light scattering experiments (200 nm) are about a factor of 10 smaller than the particles needed for real space studies (2 μm), so they explore phase space a thousand times slower and the discrepancy regime becomes inaccessible because it would take too long for the system to crystallize. The same applies to the investigation of these regions with unbiased simulations. Therefore, rare event sampling techniques must be used.

In the past, various attempts have been made to resolve this discrepancy. One general idea was to integrate the imperfections of the experiments into the computer simulations. The influence of sedimentation on the nucleation rate was investigated [27] and also polydispersity was taken into account [23, 37]. For sedimentation the authors indeed found a link between the density mismatch and a slowing down of the crystallisation process, which explains a part of the discrepancy. The slowing down of the crystallisation dynamics was associated with an increase in fivefold symmetry in sedimentation systems [27]. In addition, simulations were carried out with soft spheres, which were intended to better represent the nature of the experimental hard spheres [196]. Hydrodynamic interactions [25]and the influence of external walls were taken into account [26]. However, these investigations could only explain a small part of the discrepancy, if any. The

influence of polydispersity and electrostatic interactions will be explained in the following section on how to accurately map the experimental state point to computer simulations.

From a naive perspective, one could argue that there are two possible reasons for the discrepancy. Either the nucleation rate differs between experiments and predictions made by simulations, or the state points are not correctly mapped between the two. Before, major advances have been made in determining the volume density of colloidal samples in the last few years [42], mapping the state point between experiments and simulations was considered difficult. This is mainly due to electrostatic interactions caused by residual charges on the surfaces of the particles, which lead to a softening of the interaction potential and introduction of an effective diameter that must be determined with caution [24].

Here, we will attempt to investigate the discrepancy based on two innovations. Firstly, based on the novel deep learning routine for tracking particles in confocal images introduced in the previous chapter, "Colloidoscope", we will determine the state point of the experiments with unprecedented precision. For this purpose, we will compare 2-point, but also higher-order correlations from experiments and computer simulations, which are much more sensitive to changes in volume fraction than the radial distribution function.

Secondly, we will measure the free energy for the formation of pre-critical nuclei and thus determine the start of the nucleation barrier. In classical nucleation theory, the nucleation rate can be determined as follows using the height of the nucleation barrier ΔG^* at the critical nucleus size n^*:

$$J = f^+ \rho_f Z e^{-\beta \Delta G^*} \tag{4.1}$$

where the attempt frequency is the product of f^+ the single-particle attachment rate at the top of the barrier, the number density of the fluid ρ_f and the Zeldovich factor Z which accounts for the probability that a critical nucleus will grow to become a macroscopic nucleus [110]. To investigate the discrepancy between the nucleation rate in experiments and predictions from simulations, we will measure the free energy of formation of a pre-critical nuclei. The prefactor in equation 4.1 is well matched between experiments and simulations and has too small an influence on the nucleation rate to be responsible for the immense discrepancy.

As mentioned above, critical nucleus sizes were already determined using confocal microscopy [34, 197], but only in the regime where crystallisation proceeds rapidly and there is no discrepancy. In

the slow crystallisation regime, the critical nuclei are large and their formation is rare, therefore not accessible on the time scale of the experiments. We focus on measuring the size distribution of the pre-critical nuclei, which can be reliably measured due to their more frequent occurrence even in systems with low supersaturation and can be compared with computer simulations.

4.2 Materials and Methods

4.2.1 Experimental System

We investigated sterically stabilized PMMA spheres with a diameter of 2.0 microns and polydispersity of 4% [78] as determined using static light scattering. The particles are dispersed in two different solvent mixtures. One consisted of cyclohexyl bromide (CHB) and cis-decalin and the other one of CHB, tetralin and decalin. In both 4 mMol of tetrabutyl ammonium bromide (TBAB) salt was dissolved to screen residual charges on the surface of the particles and avoid softness in the interaction potential. By comparing the radial distribution function to hard sphere computer simulations (Fig. 4.2), we found that our particles interact very similar to the hard sphere interaction and that the choice of the solvent components has no measurable influence on the outcome of our analysis.

Nevertheless, we favour the 3-component mixture because it enables us to match the density and refractive index of the particles separately. We exclusively investigated samples with careful density matching to avoid any influence of sedimentation on the nucleation events [27, 198]. The PMMA spheres were left in the solvent for a week to equilibrate, loaded to a glass capillary and then imaged by 3D confocal laser scanning microscopy to obtain particle-resolved information.

4.2.2 Particle Tracking

The investigation of size distributions and structure of pre-critical nuclei places great demands on the quality of our experimental data. Missed particles and positions with a large localisation error not only lead to a higher uncertainty in the effective volume fraction but could also shift the calculated nucleation barrier. Therefore to extract particle coordinates from the experimental image we use a recently developed deep-learning routine called “Colloidoscope” [174]. Especially in the regime of high volume fractions where particles are densely packed and their intensity

distributions overlap, "Colloidoscope" tracks a higher number of particles with a smaller localisation uncertainty in comparison to conventional approaches, based for example on the Crocker-Grier-Algorithm [138]. We compared the outcome of different tracking routines by analysing the number of tracked particles, the shape of the $g(r)$ and the population of higher-order clusters. We found that "Colloidoscope" tracks more particles, produces a higher first peak in the $g(r)$ and an increased higher-order cluster population, which indicates that the particles are tracked with better precision. In addition "Colloidoscope" is particularly robust against the influence of photobleaching, allowing us longer exposure times and higher resolution for a longer period of time. From comparison to computer simulations we found that "Colloidoscope" tracks approximately 98% of the particles in the experimental image with an error in position of around 5% of the particle diameter.

4.2.3 Computer Simulations

In order to compare our experimental results to ideal hard spheres, we perform both unbiased and biased simulations of size polydisperse hard sphere mixtures. We match the experimentally observed distribution of particle diameters by employing a deterministically generated Gaussian distribution with 4% polydispersity (defined as the ratio of the standard deviation of the particle size σ over the mean particle size $\bar{\sigma}$). For the unbiased simulations, we use event-driven molecular dynamics simulations [199] of $N = 10^5$ particles starting from a fluid phase, for a range of different volume fractions ϕ in the supersaturated regime.

To facilitate comparison to the experimental data, we also recalculate the expected distributions of sizes of nuclei and TCC cluster concentrations in the presence of experimental errors. In order to mimic the experiments as closely as possible, we include the effects of a finite imaging volume, error in the position of the particles, and "missed" particles during tracking. First, we divide each simulation box of $N = 10^5$ particles into sub-blocks of equal volume containing approximately $N_{\mathrm{sub}} = 5000$ particles in order to simulate the effects of a finite imaging volume on the detection of nuclei. Second, we apply a random displacement to all particle positions, drawn from a Gaussian distribution with zero mean and a standard deviation of $d_{\mathrm{err}} = 0.05$. Third, we delete a small fraction α of the particles from the configuration (typically less than 2%), with the particles chosen at random. Note that this approach does not take into account the possibility of correlations between tracking error and particle environments, which could in principle be present in the experimental data.

We also perform biased Monte Carlo simulations in the isobaric-isothermal ensemble with an

umbrella sampling scheme [142], using the number of particles n in the largest crystalline nucleus as our bias parameter. The nucleus size was determined based on standard bond-orientational order parameters, described in the following section. Note that the role of the bond-orientational order parameters on the height and shape of the free-energy curve was explored in Ref. [22]. The umbrella sampling simulations allow us to reconstruct the free-energy barriers as a function of nucleus size at different supersaturations.

We also considered a hard-core Yukawa potential, taking into account softness from the screened residual charges on the surface of the particles. The pair potential is given by

$$\beta u(r) = \begin{cases} \beta\epsilon \frac{\exp[-\kappa\sigma(r/\sigma-1)]}{r/\sigma}, & r > \sigma \\ \infty, & r < \sigma \end{cases}, \tag{4.2}$$

where $\beta\epsilon$ is the value of the contact potential, κ denotes the inverse Debye screening length and σ is the particle hard-core diameter. In this work we chose $\beta\epsilon = 11$ and $1/\kappa\sigma = 0.05$ and mapped the state point of the system with softer interaction potential on hard sphere systems with the Barker-Henderson equation [200].

4.2.4 Order Parameter

We monitor the distribution of sizes of crystalline nuclei using the q_6 bond-orientational order parameters of Ten Wolde *et al.* [169], for which we employ the dot-product cutoff value to consider pairs of particles to be connected to be $q_6(i) \cdot q_6(j) = 0.7$, and where we consider a particle to be in a crystalline environment when its number of solid-like neighbors is at least 5. Specifically, we determine nearest neighbors using the SANN algorithm [172] which avoids the need for another cutoff parameter.

4.2.5 Detecting Higher-Order Structures

We analyse our data with the topological cluster classification (TCC) [162]. This detects geometric motifs whose bond topology is identical to that of clusters which minimise the local free energy for hard spheres in dense fluids [167]. The TCC uses Voronoi tessellation to identify nearest neighbours and then detects shortest path rings (3,4,5 particles) in those configurations. Basic clusters are constructed on them and by adding more particles clusters of various size can be identified. We use

identical methods for analysing experiments and computer simulations to prevent biasing certain cluster type populations.

4.2.6 Asphericity Calculation

We use Principal Component Analysis (PCA) to quantify the sphericity of crystal nuclei. We apply PCA on sets of 3D coordinates in a crystal arrangement to find the two axes of our crystal nuclei with the highest ($\lambda_{\max}$) and lowest variance ($\lambda_{\min}$). Here λ denotes the eigenvalues of the covariance matrix. For a perfect spherical nucleus, the two variances should have a similar value and therefore $\lambda_{\min}/\lambda_{\max}$ should be close to one. For our data we find distributions with a peak at 0.2 in computer simulations and experiments. This is likely because we only consider relatively small numbers of particles per pre-critical crystal nuclei. We also analysed larger crystal nuclei of up to 100 particles that were produced with biased computer simulations and found that the ratio of variances slowly converges towards one with increasing nucleus size.

4.3 Mapping Experiments to Hard Sphere State Points

Nucleation barriers are highly sensitive to the state point of the system. We want to calculate the start of the barrier from the size distribution of precritical nuclei found in experiments and compare to computer simulations. Therefore, special attention must be paid to the determination of effective volume fractions in experiments. In the following a newly developed procedure of carefully mapping experimental data sets onto computer simulations is described. One advantage of this technique is that almost no *a priori* knowledge of the properties of the sample is required for the complete characterisation. An experimental data set of a hard spheres system is described by a few parameters. These include the polydispersity, the effective volume fraction, the localization uncertainty, and the fraction of particles that get lost during the tracking process.

The polydispersity was determined from static light scattering experiments. The localisation uncertainty of the tracking routine can be inferred from its effect on the shape of the first peak of the radial distribution function as shown in Fig. 4.2(a) and was determined in a previous publication [174]. We found that adding a Gaussian error with 5% standard deviation to the simulation coordinates matches the experimental conditions.

For the mapping we use two observables, both sensitive to the state point of the system and the

interaction potential of the particles. The first one is the logarithm of the total correlation function $\log(|rh(r)|)$ with $h(r) = g(r) - 1$ (Fig. 4.2(b)). The decay of the height of the peaks is determined by the state point of the system. The second quantity is the population of higher order clusters, identified by the TCC (topological cluster classification) [162]. Both observables are also influenced by the properties of the tracking routine in a way similar to that of a change in the state point. That makes the mapping somewhat subtle.

In general, we want to find the effective volume fraction of the experiments, the effective average hard sphere diameter of the particles and from that an estimate of the fraction of particles not being identified by the tracking algorithm. The mapping routine consists of 3 steps. The first step is a comparison of the total correlation function. The experimental data is binned onto the available simulation state points. The result is a first rough estimate of the effective volume fraction for the experiments.

The second step is a careful comparison of populations of specific higher-order clusters shown in Fig. 4.2(c) that have no similarities to crystal nuclei. In comparison to the pair correlation function, cluster populations are more sensitive to the state point and allow a more accurate second estimation of the effective volume fraction.

The last step deals with the fact that for experimental data we are only considering a subset of coordinates of the "true" system. We again compare the total correlation functions of experiments and computer simulations based on the results from the second step. From that comparison an effective hard sphere diameter σ_{eff} can be extracted that is used to calculate a second effective volume fraction from the number of particles tracked N_p.

$$\phi_{\text{exp}}^{\text{counted}} = N_p \frac{\pi\sigma^3}{6V} \tag{4.3}$$

Here V is the imaged volume of the experimental system. This second estimate is smaller compared to the true value ($\phi_{\text{exp}}^{\text{counted}} < \phi_{\text{exp}}^{\text{true}}$) due to particles lost during the tracking routine. To ensure that we actually compare the identical effective state points we delete the same fraction of particles from the simulation coordinates, so that $\phi_{\text{exp}}^{\text{counted}} = \phi_{\text{sim}}^{\text{counted}}$. The fraction of deleted particles varies slightly for different volume fractions around 1%. A comparison of the distribution of those effective volume fractions is shown in the insets of Fig. 4.4.

Figure 4.2(a) and (b) show very good agreement between experiments and simulations, which clearly indicates that the state point was determined with high accuracy and that the quantification

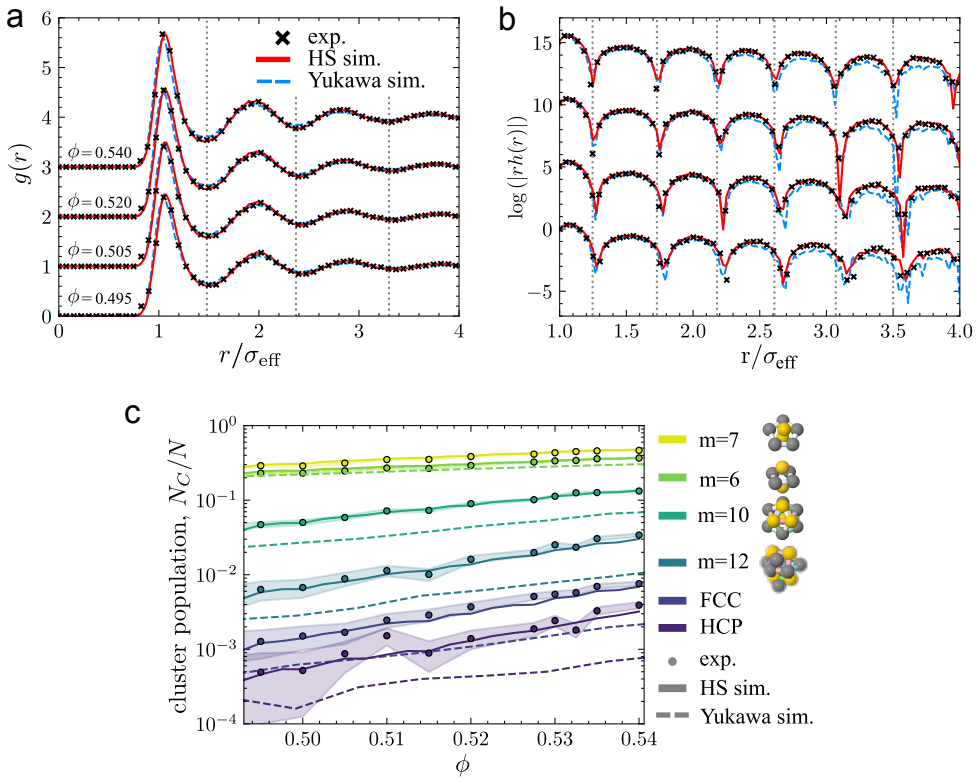

Figure 4.2: Mapping between experiment and computer simulation at fluid state points around the coexistence regime. (a) Radial distribution functions at a range of volume fractions. Data are offset for clarity. (b) Total Correlation function at a range of volume fractions. Data are offset for clarity. Same state points as shown in (a). (c) Higher-order correlations in the hard sphere fluid as a precise probe of state point matching. Selected clusters are plotted as a function of volume fraction. Errors were calculated from the standard deviation of mean populations of different experiments mapped to the same volume fraction.

of the tracking uncertainty was also successful. However, to compare the nucleation barriers from experiments and simulations, we need a quantity that is even more sensitive to changes in the volume density of the system. We examine the population of a selection of clusters identified by TCC Fig. 4.2(c) and also find excellent agreement between experiments and hard sphere simulations. Only the Yukawa simulations show a larger difference, suggesting that our experiments can be better represented by hard spheres than highly screend, slightly soft spheres. It is important to note that despite the high precision of the mapping, an assessment of the systematic error in the determination is appropriate.

As described above, the volume fraction of the experiment is determined by a compromise of the agreement between the total correlation function and the TCC population. If we only considered the best fit (least squared difference between the experiment and simulation curves) with the total correlation function, we actually end up with a value $\delta\mu = 0.0025$ less than the result of the final mapping. However, for this slightly smaller volume fraction, we find a worse agreement in the TCC

population. As a compromise between the two variables, we decide to use a slightly higher volume fraction, which results in a better agreement with of the TCC population but does not produce any noticeable difference when comparing the total correlation function. This gives us an error in the determination of the volume fraction of < 0.0025, which is an order of magnitude better than what was achieved in previous work and close to the limit for experimental colloidal systems.

Since the state point of experiments has been successfully mapped to computer simulations, we can now continue to investigate the size distribution of pre-critical nuclei and compare nucleation barriers.

4.4 Free-Energy Barrier of Precritical Nuclei

By precisely mapping the state point in the experiments, we have created a good foundation for investigating the effective free energy of the formation of pre-critical nuclei and for comparison it between experiments and computer simulations. As described above, we use the q_6 bond-orientational order parameters to identify the crystalline particles. This allows us to distinguish between separate nuclei and determine how many particles each one consists of. With N_n, the number of observed nuclei with size n, and the total number of particles N in the system, we can determine the free energy of the formation of precritical nuclei as follows:

$$\Delta G(n)/k_B T = -\log(N_n/N) \tag{4.4}$$

It is important to note that, as introduced above, we added artificial experimental errors to the simulations and randomly deleted particles from the configurations in order to reproduce the experimental volume density. Therefore the measured value in experiments and modified simulations is not the actual nucleation size n, but the *observed* value n_{obs} and with that also the *observed* barrier height $\Delta G_{\mathrm{obs}}(n_{\mathrm{obs}})$ is calculated. The true value can only be extracted from the untreated simulation data and will be discussed further later for the calculation of the nucleation rate from the height of the nucleation barrier extracted from biased simulations.

A further comment is necessary to correctly interpret the characteristics of the nucleation barriers shown in Fig. 4.3(a). The outcome of the bond-orientational order parameter analysis is a discrete value of the free energy barrier for a certain nucleus size. These discrete values were binned manually to ensure a reasonable representation of the raw data (Fig. 4.4). The size of the bins varies according

to the number of nuclei found for each size. The error bar is then calculated as the square root of the number of nuclei in each bin. Figure 4.4 shows the *observed* free-energy for formation of crystal nuclei of size ($n_{\rm obs}$) individually for different volume fraction in the coexistence regime. Crosses represent the raw data for each nuclei size. The solid lines are the averaged and binned values with error (shadows) which compensate for the fact that, particularly in imperfect experiments and simulations, not every nucleus size is identified. The barrier for these sizes would be infinitely large.

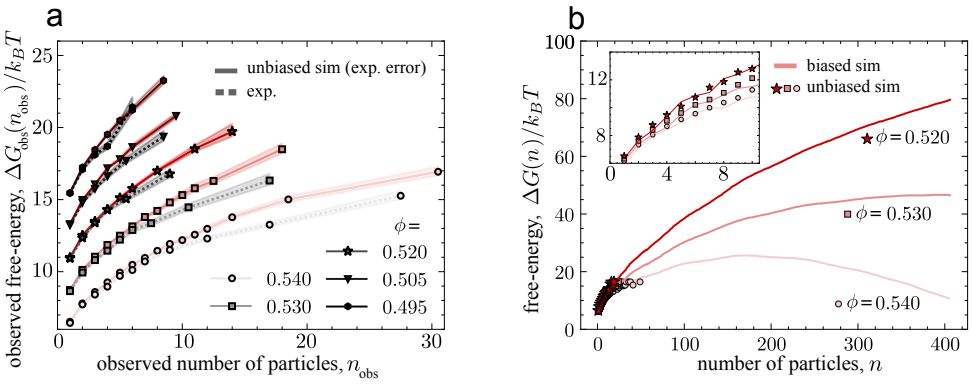

Figure 4.3: (a) Comparison of the start of the observed nucleation barrier calculated from size distribution of precritical nuclei from experiments and unbiased hard sphere computer simulations with experimental error ($\Delta G_{\rm obs}$). Data points for both were binned into different nuclei sizes to compensate for fluctuations in the number of identified nuclei. The error bars are calculated as the square root of the number of nuclei in each bin. Data are offset by $2k_BT$ each for clarity. (b) Comparison of nucleation barriers from biased hard sphere computer simulations (solid line) and nucleation barriers calculated from precritical nuclei in unbiased hard sphere computer simulations (data points), both without experimental error (ΔG). Inset shows zoomed in start of the barriers.

Figure 4.3 shows the beginning of the observed nucleation barrier for four selected state points within the coexistence regime. The data are offset for clarity. As expected, we see an increase in the free energy curves with decreasing supersaturation. For the lowest volume fraction experiments and simulations agree very well. for slightly higher volume fractions of $\phi = 0.505$ and 0.520, we cannot detect any significant differences. Only for the highest volume fractions of $\phi = 0.530$ and 0.540 we can detect differences of approximately k_BT between experiments and simulations. Surprisingly, we find good agreement in the discrepancy regime shown in Fig. 4.1 and small differences can only be seen in the range of fast nucleation, where simulations and light scattering experiments are in good agreement. However, the difference found here for the two highest volume fractions is so small that it has, if at all, only a minor influence on the nucleation rate and is not relevant for the hard sphere discrepancy.

After finding good agreement for the free energy of formation of pre-critical nuclei for a variation in volume fractions in the coexistence regime between experiments and computer simulations, we now want to extract nucleation rates from our data. Figure 4.3(a) shows the experimental data

and the observed free-energy from simulations with artificial tracking uncertainty imposed on the coordinates and random deletion of a subset of particles. To determine the nucleation rate, we now turn to the raw and biased simulations shown in Fig. 4.3(b). The logical connection is easy to explain. The experiments agree with the unbiased simulations with artificial errors. If we remove the imperfections from the simulated data, we arrive at the data points represented as circles in Fig 4.3(b). For small nuclei sizes the data points from unbiased simulations are in very good agreement with the biased simulations using umbrella sampling approach (solid lines), which we can use to extract the full nucleation barrier height from which we calculate nucleation rates for the polydisperse system [36]. We can rewrite the in equation 4.1 introduced Zeldovich factor

$$Z = \sqrt{\frac{\beta|\Delta G''(n^*)|}{2\pi}}, \tag{4.5}$$

[22, 36]. $G''(n^*)$ denotes the second derivative of the nucleation barrier at the critical nucleus size n^*. We extract the attachment rate f^+ from short Monte Carlo simulations at the top of the nucleation barrier by measuring the mean squared displacement of the cluster size [36]. We calculated the rates for the 3 different volume fractions and added them as the magenta stars in Fig. 4.1. We see good agreement between our data and estimates for the nucleation rate from previous works, also indicating that there is no evidence for the nucleation rate in our experimental data.

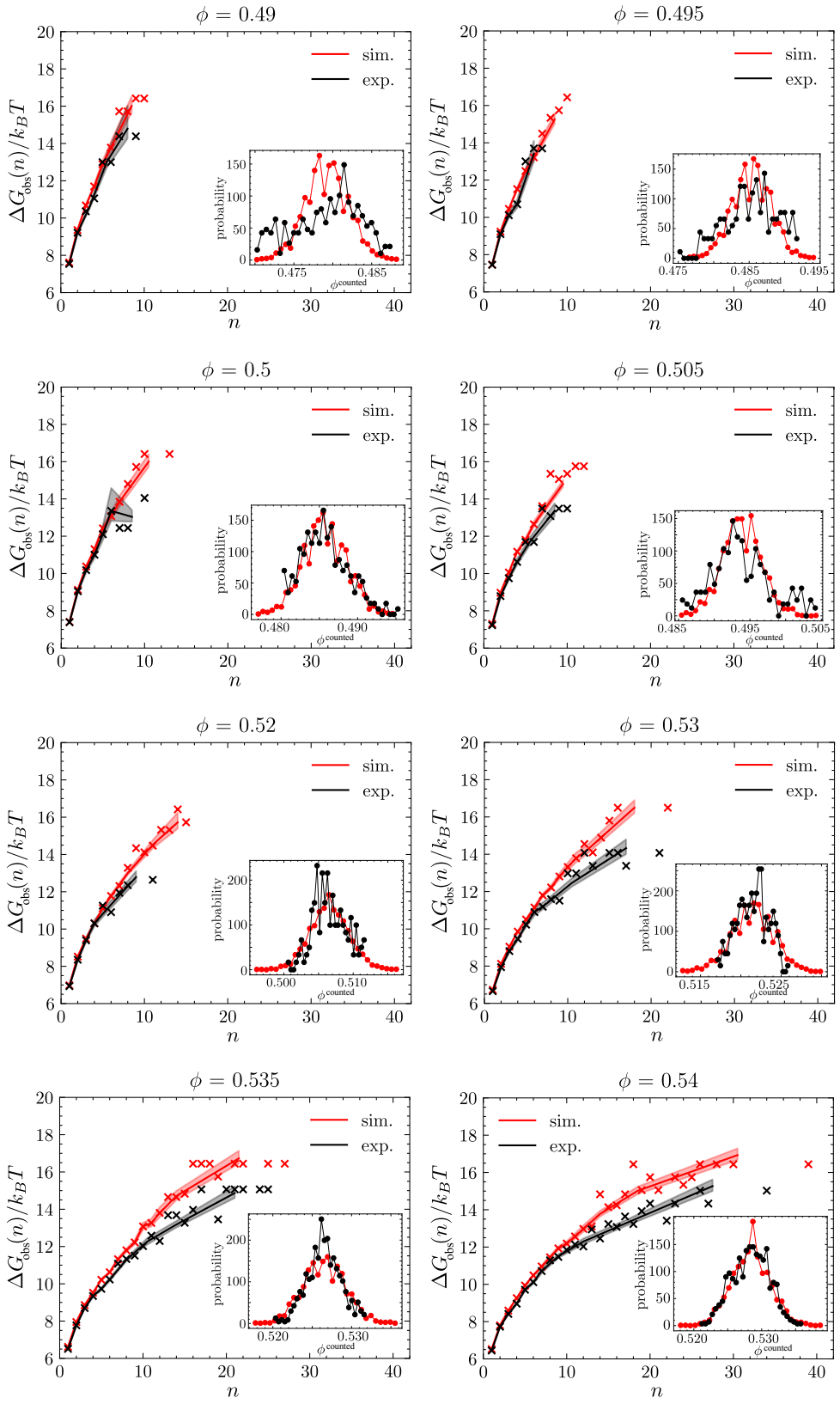

Figure 4.4: Raw output of the bond-orientational order parameter analysis (x-symbols) and the effective and binned nucleation barrier. Insets show a comparison of the effective volume fraction by counting particles between experiments and simulations.

4.5 Properties of Precritical Nuclei

Our study naturally provides a large set of crystal nuclei particle coordinates, along with those of the surrounding fluid. We now want to analyse the properties of these nuclei by exploiting our particle-resolved data.

First we use Principal Component Analysis (PCA) to quantify the sphericity of crystal nuclei. We apply PCA on sets of 3D coordinates in a crystal arrangement to find the two axes of our crystal nuclei with the highest ($\lambda_{\max}$) and lowest variance ($\lambda_{\min}$). Here λ denotes the eigenvalues of the covariance matrix. For a perfect spherical nucleus, the two variances should have a similar value and therefore $\lambda_{\min}/\lambda_{\max}$ should be close to one. For our data shown in Fig. 4.5(a) we find distributions with a peak at 0.2 in computer simulations and experiments. This is likely because we only consider relatively small numbers of particles per pre-critical crystal nuclei. We also analysed bigger crystal nuclei of up to 100 particles that were produced with biased computer simulations and found that the ratio of variances slowly converges towards one with increasing nucleus size. In general, we find good agreement between experiments and simulations and for both, large nuclei tend to be more spherical.

Another important geometric quantity is the compactness of the nuclei. This has been related to the crystal-fluid interfacial free energy [164]. Like previous work [164] we see a considerable spread in the values of the radius of gyration for a given nucleus size. We emphasize the agreement between experiment and simulation here. We also analyzed the influence of a change in volume fraction on the averaged radius of gyration. Figure 4.5 (c) and (d) show the parameters of the fitted power law as a function of the state point. While the data show considerable fluctuations, and more statistics would be needed before strong conclusions can be drawn, there is some evidence for a drop in the fitted power law b with increasing volume fraction (see Fig. 4.5 (d)). This could be interpreted as nuclei becoming less compact with increasing volume fraction, though we caution that this observation should be treated as preliminary.

4.6 Discussion

We determined the free energy of pre-critical nuclei in hard sphere systems and compared the results of experiments and simulations, finding good agreement. Of course, we did not measure the nucleation rate directly, nor did we analyse critical nuclei for the discrepancy regime to determine

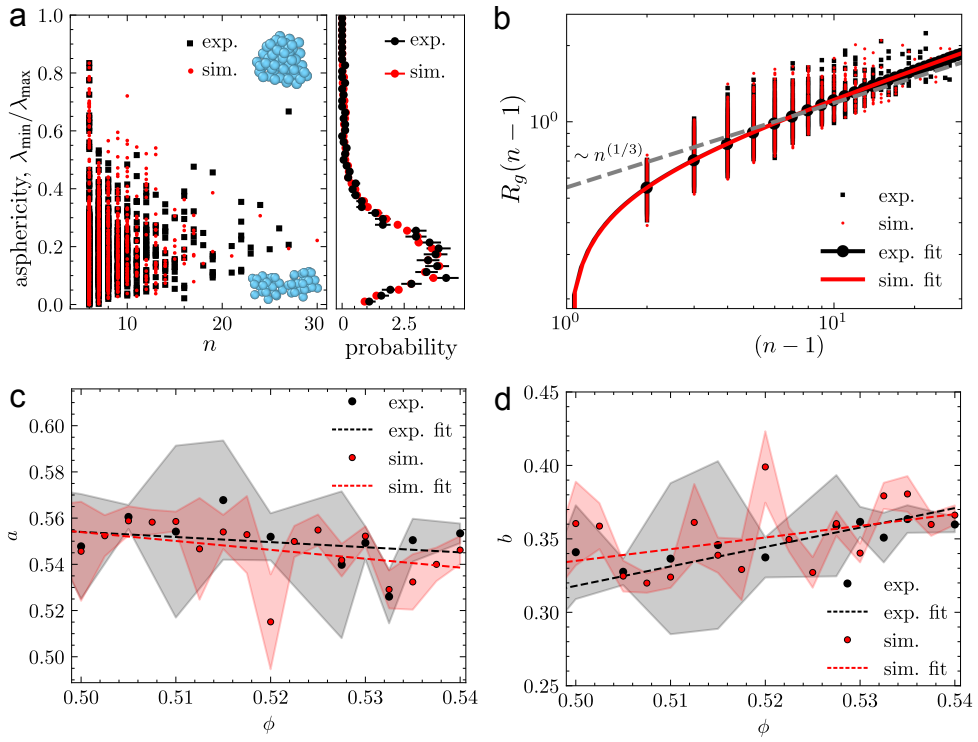

Figure 4.5: (a) Asphericity quantified by ratio of minimum and maximum variance along different axis of the pre-critical nuclei for hard sphere simulations and experiments. (b) Radius of gyration as a function of the nucleus size. Fit of shape $R_g(n-1) = a(n-1)^b$ for experiments: $a = 0.552 \pm 0.005, b = 0.361 \pm 0.006$ and computer simulations: $a = 0.550 \pm 0.005, b = 0.363 \pm 0.006$. (c)(d) Parameters a and b of the power law fit $R_g(n) = a \cdot (n-1)^b$ for experiments and simulations as a function of the state point.

the height of the nucleation barrier. Nevertheless, it is interesting that we found good agreement, especially in the small supersaturation regime close to the freezing volume fraction, where the difference in nucleation rates should be more than 10 orders of magnitude.

In contrast to the older light scattering experiments, which produce the discrepancies with simulations, we have introduced two innovations. First, we calculated the free energy using particle-resolved data. This means that the data analysis for experiments and simulations was practically identical. We performed large-scale simulations and only examined cut-outs from the datasets to imitate the character of the experiments, where we are looking at a small part of a macroscopic capillary. In addition, we introduced further experimental imperfections, such as localisation uncertainty and missing particles due to particle tracking in the experiments, into the simulations. We then determined the state point of the experiments with unprecedented accuracy in order to create an optimal foundation for calculating the free-energy of precritical nuclei, which is very sensitive to changes in volume fraction.

In the old light scattering experiments, the crystals are identified using an established method

based on the analysis of diffraction patterns. Past studies have shown that crystal formation can be reliably tracked. Since we found no evidence of a discrepancy in our experiments, we must assume that there may be a problem with the calculation of the volume fraction in the light scattering experiments. The hard sphere model system investigated here has been extensively studied and is very well characterised, but unlike most atomic systems, it poses a challenge when it comes to determining the exact state point.

Based on the results described above, we are convinced that with confocal microscopy and particle-resolved data sets we were able to improve the precision of the effective volume fraction calculation compared to studies that used the phase diagram to extract the effective particle diameter and with that calculate the state point of their sample. This approach is based on the work of Paulin and Ackerson [43], who determined phase transitions by observing phase behaviour in sedimenting samples. A more detailed explanation follows in the next chapter. One drawback of this approach is that during the nucleation process in sedimenting systems, the timescales of nucleation, phase separation and sedimentation compete with each other. The influence this has on the determination of the volume fraction and whether this can lead to the resolution of the discrepancy will be discussed in the next chapter.

4.7 Conclusion

In summary, we could not find any significant difference between the free-energies of precritical nuclei from experiments and computer simulations. The state point of our experiments was determined with improved precision based on 2-point and higher-order correlation. To put it bluntly, the hard sphere nucleation discrepancy disappears for particle-resolved data.

Further experiments with smaller particles that explore the phase space more quickly and provide more statistics in the discrepancy regime would be of great interest. With improved microscopy techniques and tracking routines, the nucleation process in the regime of small supersaturations may soon become accessible for nano particle-resolved studies [201]. Advances in other techniques, such as femtosecond X-ray spectroscopy, represent further promising avenues for investigating nucleation processes in colloidal hard sphere systems.

Chapter 5

On the Origin of the Hard Sphere Nucleation Discrepancy

The author of the thesis performed all the experiments and analysed all the data. Francesco Turci is developing a method for modelling sedimentation systems in computer simulations to support experimental results.

In the previous chapter we calculated the start of the nucleation barrier for hard sphere systems in the coexistence regime by considering precritical nuclei. After carefully mapping the experimental state point to computer simulations and adding experimental imperfections to the simulated configurations we found good agreement, especially in the regime of low supersaturation [188], where earlier light scattering experiments found a discrepancy of more than 10 orders of magnitude with respect to computer simulations [16]. We were unable to find evidence for the nucleation discrepancy from our particle-resolved studies, which raises the question of why this discrepancy is found in the earlier light scattering experiments.

Assuming that our observations are correct, there are only two possible answers to this question. Either the nucleation rate was not measured accurately in the light scattering experiments, or the calculation of the state point is biased to slightly smaller volume fractions, which could explain the increased nucleation rate compared to computer simulations.

The method for measuring the nucleation rate has been widely used since the early 1990s [29, 32, 125]. A more detailed description can be found in Chapter 1.6.5. It is based on a time-resolved

measurement of the structure factor, which is characterized by crystalline and fluid parts of the sample. The number density of the average-sized crystal can be determined from the averaged line size of the recorded signal. Finally, a nucleation rate can be determined from the evolution of the crystal number density [32]. To enable a comparison of samples with different particle sizes, the nucleation rate is rescaled with the dynamics of the particle, which is defined by its diameter. This method can be used to reliably measure nucleation rates and there is no evidence of any bias. In this context, examples of recent progress for the investigation of atomic and molecular systems must also be mentioned. In the case of argon, for example, femtosecond X-ray diffraction of microscopic liquid jets was used to measure nucleation rates for the supercooled atomic liquid, which, however, could only be brought into agreement with the theoretical predictions by fitting the thermodynamic parameters [128]. A similar approach was used to analyse the structure of water and access the regime of where ice crystallisation becomes extremely rapid [129, 130].

Figure 5.1: Sedimenting colloidal hard sphere systems with increasing volume fraction from left to right (2-10). $\phi_{\text{eff}} = 0.491, 0.517, 0.525, 0.542, 0.568, 0.593, 0.611, 0.637, 0.654$. The effective volume fractions were determined with the Paulin-Ackerson method [43]. Samples (a) immediately, (b) one, (c) four days after mixing. Reproduced from [202].

To determine the equilibrium phase diagram of the samples, an approach developed by Paulin and Ackerson is used [43]. In the coexistence regime between the freezing and melting volume fractions, where both phases are stable, the fraction of crystals χ increases linearly from 0% to 100% [23]. By measuring χ as a function of the state point, the phase boundaries can be determined using a

simple linear fit and in the next step rescaled with the known boundaries. To determine the the crystal fraction systems of sedimenting particles are used, similar to the ones shown in Fig. 5.1.

These famous images show macroscopic samples of sedimenting PMMA particles with a diameter $\sigma = 320$ nm and polydispersity $s \approx 0.05$, refractive index matched with the solvent. A total of nine samples with volume fractions ϕ between 0.491 (sample2) and 0.654 (sample10) were prepared and imaged immediately after mixing (Fig. 5.1(a)). After one day (5.1(b)), an iridescent crystalline sediment with a sharp interface to the fluid on top can be observed for the samples in the coexistence regime (3-5), whereas the sample with the lowest volume fraction (2) remains in an equilibrium fluid state. Samples with slightly higher concentrations (6-8) are already completely crystallized, in contrast to samples (9-10) with the highest volume fraction, which remain in a glassy amorphous state. After four days (Fig 5.1(c)), it is assumed that the systems have completed their phase separation. In sample (2), sedimentation has formed a small crystal layer at the bottom. All other samples show similar behaviour as before, with a crystal sediment and fluid above it, completely crystallized or in a glassy state.

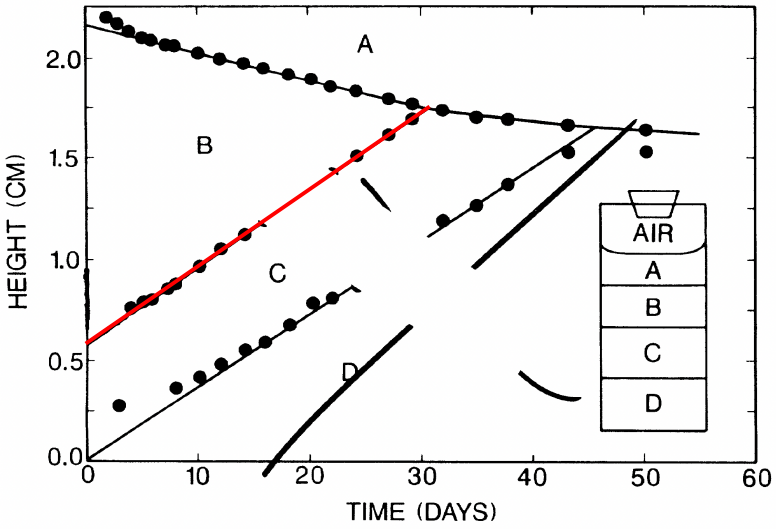

Figure 5.2: Height of different regions in the sample ($\phi = 0.49$) as a function of time. Indent shows the structure of the sample after sedimentation. Reproduced from [43].

The following section provides a more detailed explanation of this process and its application in determining the effective volume fraction. In macroscopic systems with high density and low Péclet number, the sedimentation dynamics can be described by a batch settling process [89]. First, a sample with a volume fraction in the coexistence region and homogeneous density distribution is produced. The particles sediment downwards to the bottom and crystallize, resulting in a polycrystalline sediment that grows over time. A schematic representation of a sample during

sedimentation can be seen in the inset of Fig. 5.2. A high-density polycrystalline sediment (D) forms at the bottom of the sample. Above is a the polycrystalline solid (C), followed by the sedimenting liquid (B) and the clear supernatant (A). For our investigations, the division between the two regions (C) and (D) is irrelevant, and we consider them together as crystal sediment. After a certain period of time, a balance between sedimentation and diffusion is established. Then only a very small region of the fluid remains, with a size in z-direction comparable to the gravitational length. If one creates a linear fit for the height of the boundary between crystalline sediment and liquid (red line in Fig. 5.2), one can interpolate back to $t = 0$ and obtain the crystal fraction (χ) prior to sedimentation, where the system is phase-separated *prior* to the influence of an external field.

However, this approach is based on the assumption that the timescales of sedimentation (months) and phase separation (days) are well separated. We argue that this is not necessarily the case and that critical nuclei may be present in the sedimenting fluid. This would then result in a bias in the calculation of the effective volume fraction, which could possibly explain the discrepancy.

In this chapter, we will first introduce a case study to show how exactly the presence of crystalline structures in the liquid affects the calculated volume fraction. We will then reproduce Paulin and Ackerson's experimental setup, but examine the system over time using confocal microscopy. With the particle-resolved data, we can probe for crystal nuclei in the sedimenting liquid.

5.1 Making the Nucleation Discrepancy Disappear

Here, we want to take a closer look at the influence that a change in crystallinity in the sedimenting macroscopic system could have on the measured effective volume fraction. First, we examine the figure introduced in the previous chapter again, which illustrates the nucleation discrepancy. In contrast to the previous representation, here the experimental data points have been shifted by $\delta\phi = 0.005$ to larger volume fractions, which results in the disappearance of the discrepancy in the range of small supersaturation (5.3). This bias represents a systematic error in the determination of the state points, which is larger than the typical random uncertainty associated with the Paulin-Ackerson method [23].

To determine the amount of crystal in the sedimenting liquid that could cause such a bias, we perform an example calculation (Fig. 5.4(a)). A macroscopic sample with unknown volume fraction in the coexistence regime is left to sediment. After measuring the height of the sediment over time as shown in Fig. 5.2, the crystal fraction of the system can be determined *prior* the influence

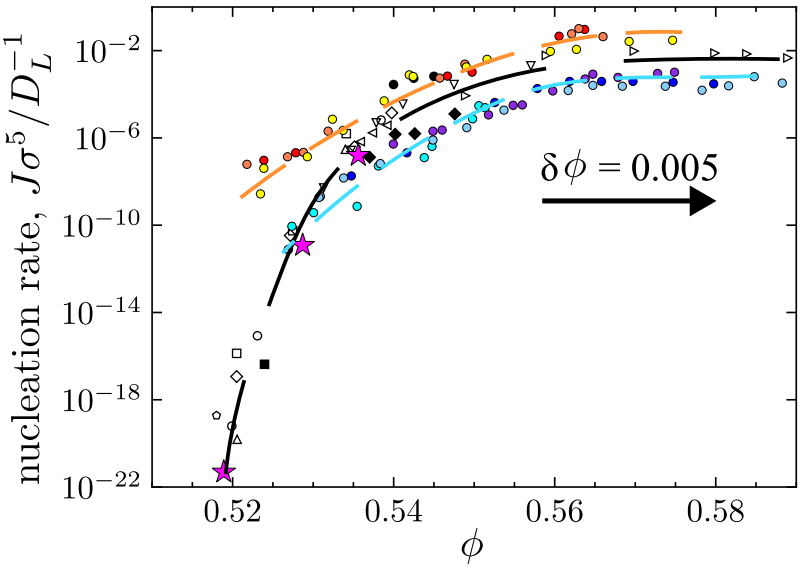

Figure 5.3: Reduced dimensionless nucleation rates as function of state point for experiments and computer simulations. Experimental data is shifted by $\delta\phi = 0.005$ to slightly higher volume fractions, leading to the disappearance of the discrepancy (see representation in the previous chapter for references).

of gravity. After interpolation, we can obtain $\chi_{obs} = 35.6\%$ in our case. Considering that the crystal fraction χ at the freezing volume fraction ϕ_f is equal 0% and then increases linearly to 100% at the melting volume fraction ϕ_m, a volume fraction of $\phi_{obs} = 0.51$ can be calculated from $\chi_{obs} = 35.6\%$. However, we assume that the correct value is underestimated by $\delta\phi = 0.005$ and that the corrected volume fraction should actually be $\phi_c = 0.515$. We can calculate the crystal fraction in the sedimenting liquid with

$$\chi_L = \frac{\left(\frac{\delta\phi}{\phi_\mathrm{m}-\phi_\mathrm{f}}\right)}{1-\left(\frac{\phi_\mathrm{obs}-\phi_\mathrm{f}}{\phi_\mathrm{m}-\phi_\mathrm{f}}\right)}, \tag{5.1}$$

where $\delta\phi = 0.005$ is the constant volume fraction bias, ϕ_m, ϕ_f are the phase boundaries (see Fig. 5.4(a)) and $\chi_{obs} = 35.6\%$ is the observed total crystal fraction we get from reproducing the sedimentation experiments.

In other words, To remain within the framework of Paulin and Ackerson's picture, this would mean that at $t = 0$ there is no clear phase separation, but rather $\chi_L = 15.1\%$ of the sedimenting liquid is crystalline. It is important to note that this effect depends on the effective volume fraction of the sample. As the liquid phase sitting on top of the crystal gets smaller with increasing volume fraction, the crystal fraction of the liquid also has to increase in order to introduce a constant bias of $\delta\phi = 0.005$. Figure 5.4(b) shows the expected crystal fraction in the liquid χ_L as a function of the state point extracted using the Paulin-Ackerson method ϕ_obs. The crystal fraction χ_L increases

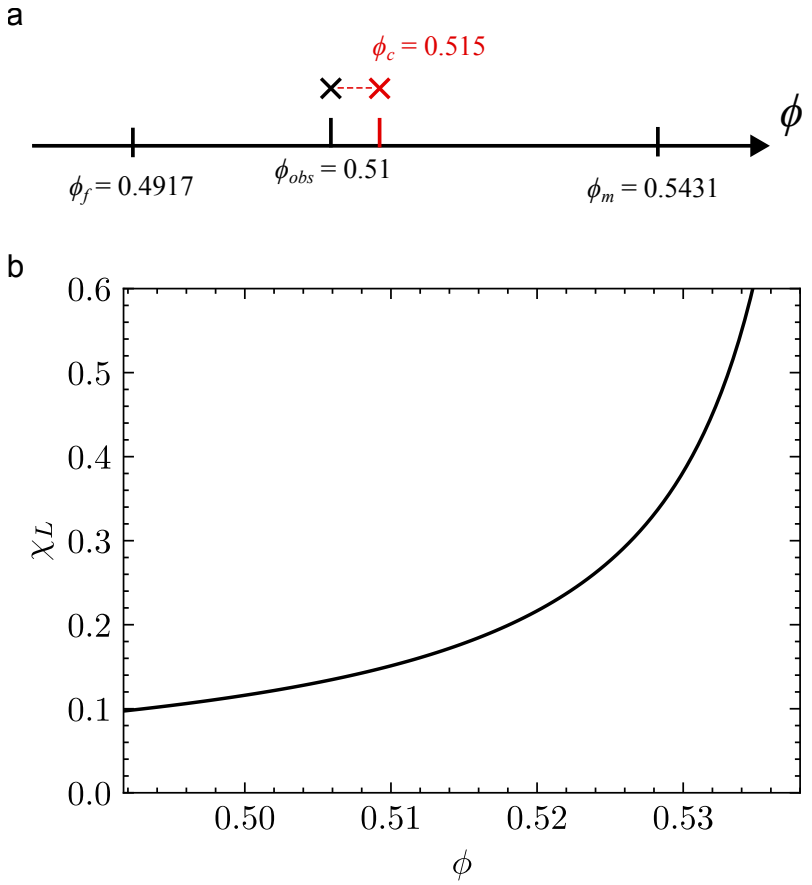

Figure 5.4: Expected crystal population in sedimenting liquid. (a) Schematic representation of the volume fraction shift due to higher crystallinity. An increase in volume fraction of $\delta\phi = \phi_c - \phi_{obs} = 0.05$ for a system with $\phi = 0.51$ is equivalent to an increase in the observed crystallinity $\delta\chi = 15.1\%$. (b) Expected crystal fraction χ_L in the sedimenting liquid to introduce constant volume fraction bias $\delta\phi = 0.005$ for all volume fractions in the coexistence regime.

massively for volume fractions close to the melting phase boundary, which is related to the small volume at the top of compared to the total volume of the system.

5.2 Material and Methods

We want to investigate colloidal hard spheres that sediment in a gravitational field. These systems are characterized by the volume fraction $\phi(z,t)$ and the Péclet number. The Péclet number represents the ratio of the two timescales dominating the system

$$\mathrm{Pe} = \frac{\tau_B}{\tau_s}. \tag{5.2}$$

For diffusion, this is the Brownian time defined as the time an isolated particle with radius a needs to diffuse a distance equal to its own radius, $\tau_B = 3\pi\eta\sigma^3/(4k_BT)$, where η is the dynamical viscosity of the solvent and $\sigma = 2a$ is the diameter of the particle. For sedimentation, the time it takes for a particle to sediment its radius $\tau_s = \sigma/(2u_0)$, where $u_0 = \Gamma_0 mg$ describes the average (Stokes) velocity, which is defined as $\Gamma_0 = (6\pi\eta a)^{-1}$ for no slip boundary conditions on the sphere and m, g are the buoyant mass of the particle and the acceleration of the gravitational field, determines the characteristic time scale. In experiments, another quantity is often used to characterise the system, the gravitational length ξ_g. It is closely related to the Péclet number by $\mathrm{Pe} = a/\xi_g$.

To experimentally determine the gravitational length of a system, samples with a small volume fraction are produced and left to sediment for a few days until hydrostatic equilibrium is established. In this regime, the particles can be considered non-interacting (ideal gas limit) and there is an equilibrium between gravity, which pulls the particles downwards, and entropy, which favours a homogeneous mixture of the system. An inhomogeneous density distribution (barometric) is established and the volume fraction as a function of height in the sample (opposite to the direction of gravity, z) decreases exponentially, $\phi(z) = \phi_0 \exp(-z/\xi_g)$.

For our investigations of the structure of the sedimenting liquid, we want to focus on systems dominated by diffusion, i.e. $\mathrm{Pe} \ll 1$. In the following sections we want to describe how samples in the coexistence regime with a specific difference in density are produced and characterised. In addition, a detailed description will be provided of how the samples are imaged during sedimentation.

5.2.1 Sample Preparation with Density Difference

To realise sedimenting hard spheres in a gravitational field, we use a very similar system to the one introduced in Chapter 2.1. It consists of slightly smaller PMMA particles ($\sigma = 1.75$ μm and $\tau_B = 9.4$ s) dispersed in a mixture of Decalin, Tetralin and CHB. Particles and solvent are refractive index and, in the first step, density matched. Again TBAB salt was added to screen residual charges on the surface of the particles, ensuring hard sphere like interactions. In addition, a previous study [203] has shown that in systems of charged particles with long-range repulsion, a macroscopic electric field builds up that acts against sedimentation and leads to an extended sedimentation profile. This is also prevented by adding TBAB. After leaving the sample to equilibrate for a week, the solvent composition can be changed to make the particles sediment.

The amount of Decalin required to realise different Péclet numbers can then be calculated from

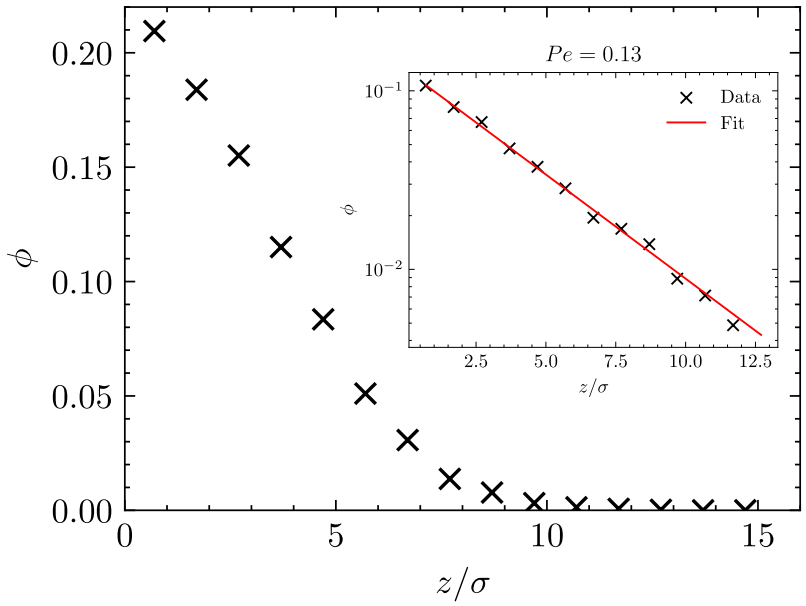

Figure 5.5: The sedimentation profile follows the barometric law. Inset shows semi-logarithmic plot of the density profile. By fitting an exponential (red line) we can extract the gravitational length ξ_g and Péclet number.

the volume of the sample and pellet, because Particles and solvent have the same density. For each solvent batch we produced a very dilute microscopic sample and extracted the gravitational length. An example measurement is shown in Fig. 5.5. After the samples have reached equilibrium, indicated by a stable density profile over time, the gravitational length can be extracted by fitting an exponential to the equilibrium density function. Then we calculated the Péclet number Pe = 0.13. We found that the Péclet numbers of the individual samples differ only slightly.

To obtain an estimate of the sedimentation velocity, we can determine the mobility Γ_0 from the density difference, as described above. We end up with a sedimentation velocity of 2476 μm/day for an isolated sphere. However, we must take hydrodynamic effects into account for the samples to be investigated with volume fractions in the coexistence regime. We follow the results of Hayakawa and Ichiki [204] and end up with a new expression for the mobility as a function of the volume fraction

$$\frac{\Gamma_{\mathrm{HI}}(\phi)}{\Gamma_0} = \frac{(1-\phi)^3}{1+2\phi+1.492\phi(1-\phi)^3}. \tag{5.3}$$

For a system with $\phi = 0.5$, we calculate a sedimentation velocity of approximately 64 μm/day.

5.2.2 Capillary and Imaging

After the composition of the solvent has been adjusted and analysed, macroscopic samples with higher volume fractions are produced in the coexistence regime. These can be used to measure the height of the crystalline sediment over time and analyse the structure of the liquid. A square glass capillary of 600×600 μm and length of ca. 50 mm is filled with the sample and glued with Norland adhesive to a microscopy slide. A sketch of the sample structure is shown in Fig. 5.6(a). The microscope slides are then placed in an upright position and the sample is left to sediment.

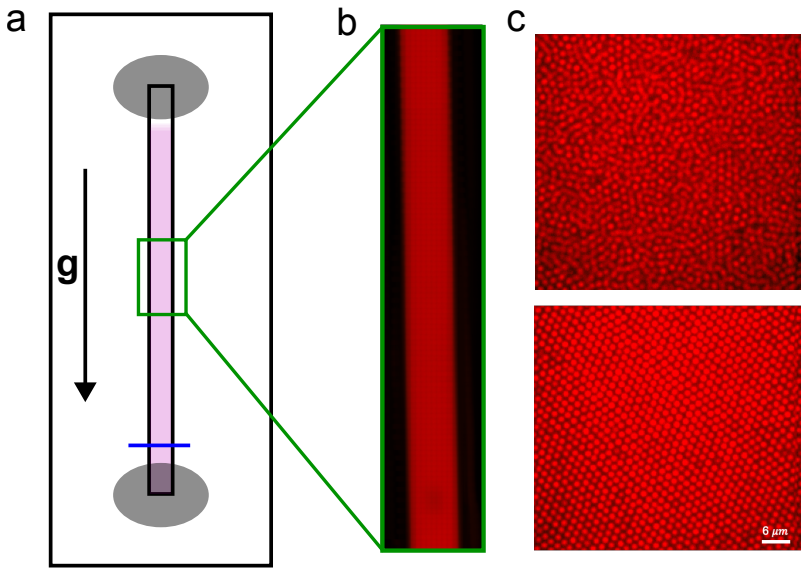

Figure 5.6: Structure of the macroscopic sample (a) Sketch of the sample structure. Capillary with dimensions $0.6 \times 0.6 \times 50$ mm (macroscopic in direction along the gravitational field) filled with sample. End of capillary sealed and attached to microscopy slide with Norland adhesive. Marker on the capillary to calibrate height in the capillary for each measurement. (b) Multiscale image of the sample, composed of many individual confocal images stitched together. (c) Zoomed-in sections from (b) showing liquid at the top and crystalline phases at the bottom of the capillary.

Previous experiments have shown that repositioning the capillary in a horizontal position for image acquisition can lead to disturbances in the structure of the sample. We therefore use a special setup that allows the entire microscope to be rotated. The objective lens points horizontally and the sample can be imaged as it is stored (gravitational field points perpendicular to the optical axis).

Due to the dimensions of the whole sample, it is not possible to examine the entire system using 3D microscopy. For this reason, several multiscale 2D images of the centre of the capillary are taken across the entire height of the sample. An example image is shown in Fig. 5.6(b). The image consists of 15×100 individual images consisting of 400×400 pixels (0.16 μm/pixel). We used a standard 40x lens.

The advantage of this imaging technique can be seen in Fig. 5.6(c). We can image the entire capillary and still obtain information about the structure of the sample at the particle level based on the 2D information. In particular, a distinction can be made between liquid (Fig. 5.6(c) top) and crystal regions (Fig. 5.6(c) bottom). This allows both the height of the crystalline sediment to be determined over time and the structure of the liquid to be examined for the presence of large crystalline structures.

We trained a simple neural network to analyse the multiscale images. We employed a U-Net with a ResNet-18 encoder pretrained on ImageNet for binary segmentation of grayscale microscopy images. Data were split into training and validation sets and augmented with cropping, intensity adjustments, flips, and per-image normalization. The model was trained using AdamW with a combined Binary Cross-Entropy and Dice loss, and performance was monitored with Dice and IoU scores, saving the best model based on validation Dice.

5.3 Structure in Sedimenting Hard Sphere Systems

Figure 5.7 shows the height of the crystalline sediment over time, measured using images from the confocal microscope. As in the original paper by Paulin and Ackerson [43], we observe linear growth of the crystalline sediment. By fitting a linear function to the data points and interpolating back to $t = 0$, we obtain a value for the crystal fraction prior to the influence of gravity. From this, we can determine a crystal fraction of $\chi_{\text{obs}} = 0.067$, which corresponds to a volume fraction of $\phi_{\text{obs}} = 0.495$ according to the Lever rule.

The format of the outcome of the experiments is identical to the measurements carried out for light scattering experiments to determine the state point, but we also have the option of examining the structure of the sedimenting liquid. Figure 5.8(a) shows an image taken with the confocal microscope after analysis with our neural network. White regions are crystalline and dark regions are in liquid phase. The direction of gravity is from right to left. The image reflects only a section of the actual sample, similar to the section shown in Fig. 5.6. It is clear to see that crystalline structures are located above the interface between sediment and liquid.

To determine the crystal fraction, we track the crystal population averaged over the plane perpendicular to the direction of gravity (Figure 5.8(b)). We obtain a value that depends on the height in the capillary, from which we can easily determine the exact position of the interface by fitting a hyperbolic tangent function and, through integration, also calculate the total crystal fraction in the

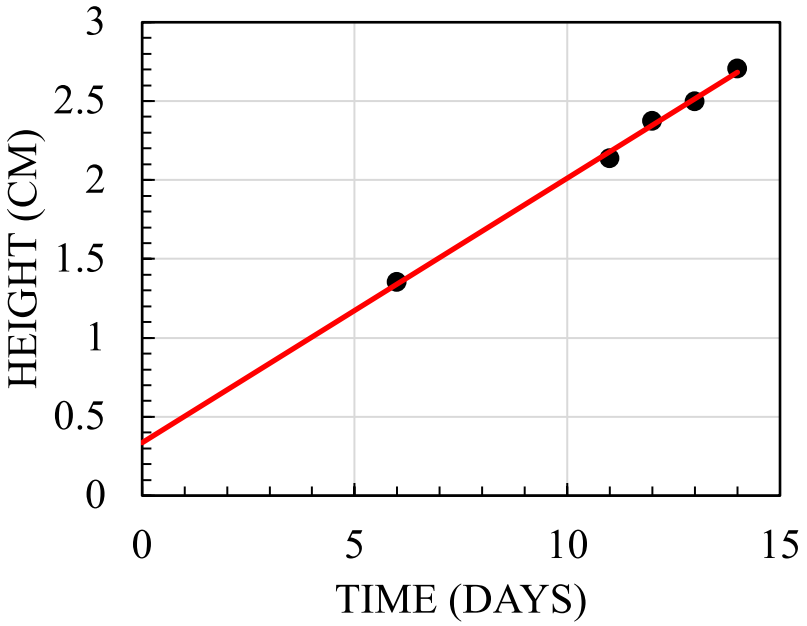

Figure 5.7: Height of the sediment as a function of time. Red line represents linear fit to the data to get the crystallinity χ of the system *prior* sedimentation. From the intercept of the linear fit we get $\chi = 0.067$ and calculate $\phi = 0.495$.

liquid. After integration, we obtain a crystal fraction in the liquid of approximately $\chi_{\mathrm{L,obs}} = 0.092$. From Eq. 5.1, we find that at this state point, we actually need a crystal fraction of $\chi_{\mathrm{L}} = 0.104$ to shift the experiments by $\delta\phi = 0.005$. This is in very good agreement with our result.

5.4 Conclusion

We have succeeded in reproducing the method developed by Paulin and Ackerson [43], which is used to determine the state point of samples for light scattering experiments, using confocal microscopy. From our measurements, we were able to determine the crystal fraction of the system prior to sedimentation by measuring the height of the crystalline sediment over time and calculating the volume fraction from this. We determined the sedimentation velocity and Péclet number using highly diluted samples by examining the equilibrium density distribution. At $\mathrm{Pe} = 0.13$ for our systems, the dynamics are dominated by diffusion and the crystalline sediment forms on a timescale of days, as described in the paper by Paulin and Ackerson.

However, crystalline structures also nucleate in the sedimenting liquid on this timescale. We were able to recognise this using multiscale images taken with the confocal microscope. Large crystal nuclei are located above the crystal-liquid interface in the system. After analysing the microscopic images with a self-developed deep learning approach, we were able to determine the crystal fraction

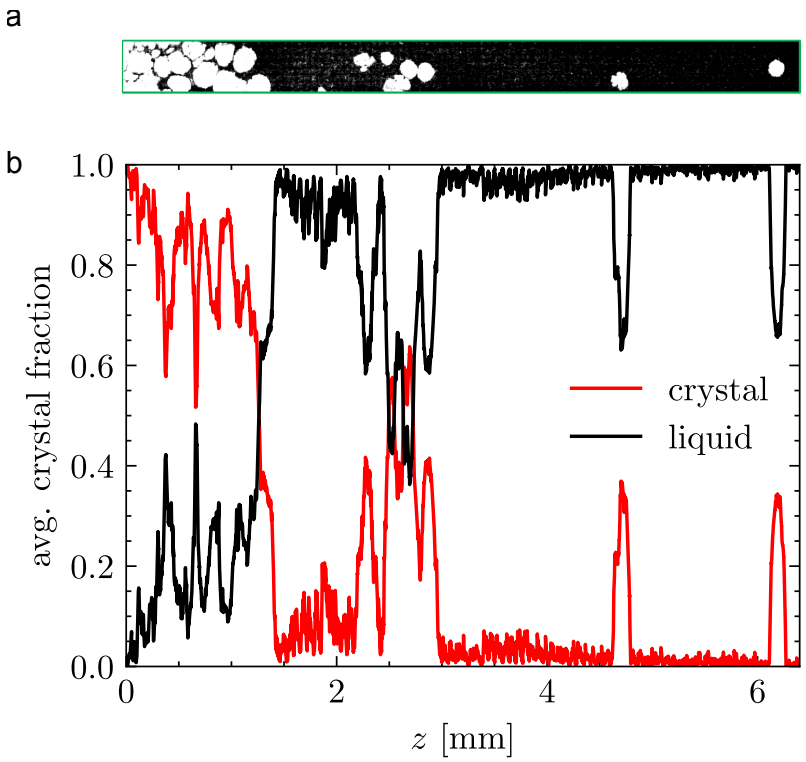

Figure 5.8: Analysis of the sedimenting system. (a) Binary segmentation of the experimental image into foreground (crystal) and background (liquid). (b) Averaged crystal fraction as function of height in the capillary.

in the liquid and correlate it with a bias in the calculated volume fraction.

To resolve the discrepancy between experimentally measured and computer simulation-determined nucleation rates, the volume fraction in the experiments would have to be systematically underestimated by $\delta\phi = 0.005$. In our experiments, we find a crystal fraction in the sedimenting liquid close to the value we calculated for this bias in the volume fraction.

It should be noted that the crystal fraction in the liquid depends on the state of the system. Further measurements of systems with different volume fractions will therefore be necessary in the future. At this point, at least two additional data sets were recorded that can be examined. Unfortunately, we encountered difficulties in analysing the systems that were recorded with slightly altered image properties. The neural network does not yet appear to be robust enough to withstand these influences and can only identify the crystal regions with significant noise, making them unusable for determining the crystal fraction in the liquid.

In addition, computer simulations of nucleation events in sedimenting liquids are being investigated in collaboration with Francesco Turci (University of Bristol). We hope that the data will provide further insight into crystallisation in the systems under investigation.

Chapter 6

Direct Observation of Ostwald's Rule of Stages in a Colloidal Model System

Experiments were conducted by Xiaoyue Wu during her PhD project under the supervision of Fiona Meldrum and by the author. All data analysis was performed solely by the author of this thesis. Simulations to determine the equation of state are performed by C. Patrick Royall. Fabio Leoni and John Russo are also part of this project and developed the deep-learning routine and trained the neural network used to identify the crystal structures and distinguish between the different polymorphs.

When a system undergoes a phase transition, it does not necessarily transition directly to the most thermodynamically stable form. In fact, the system often goes through a sequence of phases with decreasing free energy, which is described as Ostwald's rule of stages [53]. This can explain phenomena such as polymorph selection, in which different crystal structures with varying degrees of stability compete during a phase transition, resulting in a complex multi-stage crystallisation process [205]. This phenomenon was described in detail in Chapter 1.6.4.

A famous example of the influence of polymorphic selection is the so-called "ritonavir crisis" in the late 1990s. Ritonavir was originally marketed in its metastable form I, but over time the more stable form II formed. Form I crystallised because its free energy was closer to the parent phase,

but at some point it transformed into the thermodynamically more stable form II. This led to changes in solubility and bioavailability, which significantly reduced the drug's effectiveness and ultimately led to its recall [206].

It is evident that a fundamental understanding of the underlying processes of crystallisation is of great importance. However, the investigation is very complex. The rare-event character of nucleation processes, i.e. their microscopic time and length scales, makes investigation using experiments and brute-force computer simulations very challenging and direct observation poses a major challenge in various scientific fields.

Here, we investigate Ostwald's rule of stages using colloidal model systems. Colloids follow the same statistical laws as atoms and molecules [72], but can be imaged in real time with a microscope. They can be described by classical physics, which makes them easily accessible for studies with computer simulations, making colloidal systems an ideal platform with which to study microscopic phenomena such as nucleation [18], crystal growth [207] and melting [208, 209]. Confocal microscopy allows us to track detailed structural changes in the systems at the particle level and support our results with data from computer simulations [17, 18, 44].

In the past, studies of polymorphism in colloids have been limited to polymorph selection [52, 210] and the role of interfaces [211]. Ostwald ripening was only considered for amorphous states transforming into a crystalline structure [212]. We want to use a different colloidal system consisting of dipolar particles [48, 107]. At least five polymorphs, including face-centred cubic (FCC), hexagonal close packing (HCP), body-centred cubic (BCC), body-centred tetragonal (BCT) and body-centred orthorhombic (BCO), occur in this system, and the great advantage is that we can directly control the interaction strength in experiments and simulations *in vivo* and thus the phase behaviour. The tunability makes the system an ideal model for investigating Ostwald's rule of stages.

The dipolar interactions are introduced by an external alternating field pointing in the z-direction. Experimental [48] and computer simulation [51] work has investigated the phase behaviour, in which body-centred tetragonal (BCT), face-centred cubic (FCC) and hexagonal close packing (HCP) crystal structures were identified [213, 214]. We want to investigate a system in which a metastable HCP crystal has formed, which then melts and is replaced by a BCT crystal (stable phase).

In the following, we will first introduce the model system of dipolar colloids and explain the phase behaviour in detail. This is followed by a description of the realisation of such systems in experiments and computer simulations. On this basis, Ostwald's rule of stages will then be

analysed using the example just described. We analyse structural changes in the fluid surrounding the different polymorphs in order to understand the fundamental processes.

6.1 Material and Methods

We will briefly explain the dipolar interactions and the resulting phase diagram. This is followed by a description of our experimental colloidal samples and the sample cell used. Finally, we explain how we mapped the state points of the experiments to the computer simulations and how exactly we implemented the dipolar particles in computer simulations.

6.1.1 Dipolar Interactions in Colloidal Systems

Colloids in an external electric field interact with a dipole-dipole particle interaction, which was introduced in Chapter 1.4. The particles attract each other along the electric field and repel each other perpendicular to it. The dipole interaction strength can be controlled via the field strength.

Systems with this type of interaction potential display a rich variety of phases and interesting phase behaviour. Figure 6.1(b) shows the resulting phase diagram. At low volume fractions and weak dipolar strengths, the system remains in a fluid state. As the electric field—and consequently the dipolar interaction strength—increases, the system transitions into a string fluid phase, where particles form chain-like structures aligned with the field and coexist with the BCT crystal phase. At higher volume fractions, the system spontaneously crystallises into BCT or HCP phases, and into FCC at very low dipolar strengths, resembling the behaviour of a pure hard-sphere system.

The rich phase behaviour makes the system of dipolar colloids a good subject for investigating Ostwald's rule of stages. This is particularly important because, in experimental practice, a sample with a constant volume fraction is produced, but then different regions of the phase diagram can be investigated by changing the external electric field.

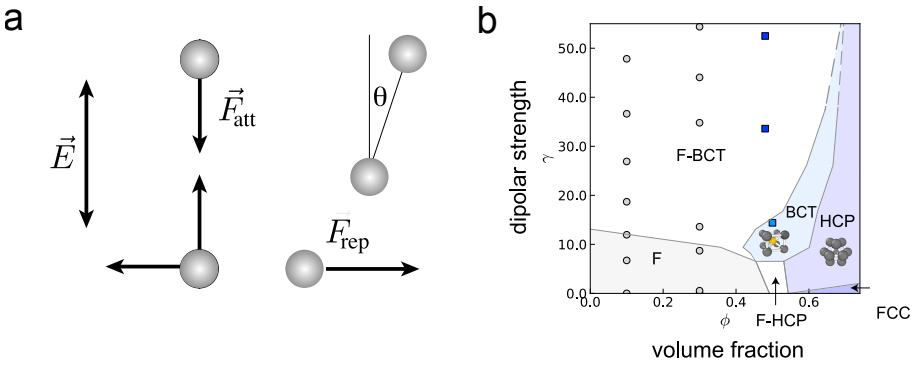

Figure 6.1: Schematic representation of dipolar interaction and phase diagram. (a) Dipolar interactions in a colloidal model system, where an AC electric field $\vec{E}$ is applied along the z-direction, inducing dipoles on the colloidal particles. (b) Phase diagram of the colloidal dipolar system. Phase boundaries are reproduced from Hynninen and Dijkstra [51]. Grey regions indicate phase coexistence. Data points denote the experimental state points realised. The pale blue data point (square) corresponds to the HCP–BCT transformation following Ostwald's rule of stages, while the two darker blue data (squares) points at higher dipolar strengths crystallise directly into the BCT phase.

6.1.2 Experimental Realisation of Dipolar Particles

Colloidal System

In order to experimentally realise colloidal systems with dipole-dipole interaction, an external electric field must be induced in the sample. The colloidal suspension used in this experiment was prepared by adding sterically-stabilised polymethyl methacrylate (PMMA) spheres (synthesized following reference [215]) ($\rho = 1.196$ gcm^{-3}) [203] of diameter $\sigma = 1.73$ μm and polydispersity $\lesssim 5\%$ (measured using static light scattering) to a mixture of density and refractive index matched solvents [216]. The particles were labelled with 1,1'-dioctadecyl-3,3,3',3'-tetramethyl-indocarbocyanine perchlorate, which may be excited at a wavelength of 543 nm [215]. The solvent is a mixture of cis-decalin ($\rho \approx 0.897$ gcm^{-3}) and cyclohexyl-bromide (CHB) ($\rho \approx 1.32$ gcm^{-3}). Tetrabutylammonium bromide (TBAB) salt was dissolved in the solvent to make up a solution with a TBAB concentration of 260 μM. This corresponds to a Debye length κ^{-1} of around 100 nm [34]. Since the Debye length is much less than the particle diameter, in the absence of an electric field, the colloids behave as nearly hard spheres [24, 34]. While more sophisticated treatments may be carried out to match the interaction potential, here we use a slightly soft potential in the computer simulations [78].

We determine the dipolar contribution to the interaction potential between the particles by evaluating Eqs. 1.11 and 1.12 with the particle diameter σ, the solvent dielectric constant $\epsilon_s = 5.6$ [217] and the measured value of the local electric field E.

In order to construct the sample cell to hold the colloidal suspension, two indium tin oxide glass slides (SPI supplies, thickness 0.13 to 0.17 mm, resistance 8 to 12 Ω) around 2 cm square were separated with spacer silica particles around 60 μm in diameter. A schematic representation of the sample structure is shown in Fig. 6.2. The electrodes were connected to a signal generator to provide an AC electric field across the sample. Everything was affixed by Norland Optical Adhesive 61. We use a Leica SP8 confocal microscope. During each measurement, 3D confocal images with at least ten pixels per particle diameter were captured.

In each measurement, the applied voltage and the thickness of the sample cell was measured in order to allow electric field strength comparison across different experiments. The frequency of the electric field applied was 1 MHz and the field strength was up to 0.3 $V\mu^{-1}$ measured peak-to-peak.

The Brownian time $\tau_B = (3\pi\nu\sigma^3)/(4k_BT) \approx 6.09\ s$ for our system, so we consider 30 min before starting the imaging process quite sufficient to relax equilibrium states. Here ν is the solvent viscosity.

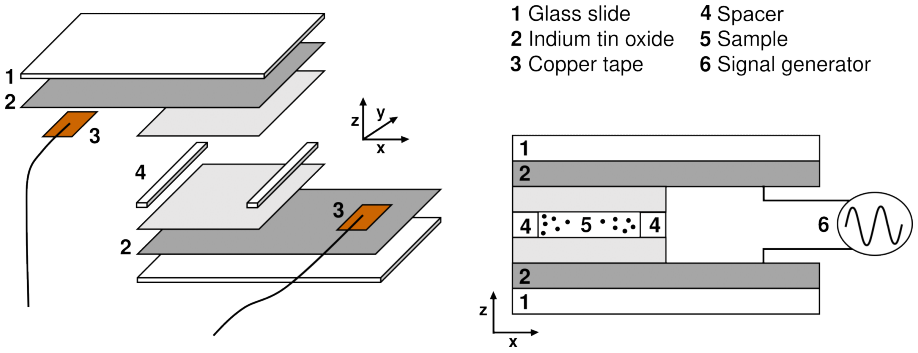

Figure 6.2: Schematic representation of the sample structure. The sample is placed between two ITO covered cover slips connected to a signal generator. The direction of the external electric field points in z-direction, parallel to the optical axis of the imaging setup. Reproduced from [104]

Particle Tracking

To extract particle positions from 3D confocal images we use the earlier introduced deep-learning routine called "Colloidoscope" [174]. In order to analyse the structure of the colloidal fluid on the basis of particle-resolved data, a reliable tracking routine is required that determines as many positions of the particles in the system as possible with high precision. Lost particles or positions with an increased uncertainty in the localisation could lead to clusters or crystal nuclei not being identified or being identified incorrectly. "Colloidoscope" was specially developed for high-density systems to meet these requirements. Especially in systems with dipolar interactions, where particles tend to form string-like configurations, tracking positions is challenging because the lower resolution

of the confocal microscope in the z-direction leads to overlapping of intensity distributions of single particles sitting on top of each other. With "Colloidoscope" we were able to track roughly 98% of the particles in the system with an error in position of around 5% of the particle diameter. This is much better compared to results we obtained with conventional methods based on the Crocker-Grier-Algorithm, for example [138]. We quantified the quality of the output of the tracking routine by comparing the shape of the $g(r)$ from experiments with the results of computer simulations to which we added experimental imperfections (localisation uncertainty and missing particles).

Mapping Experimental Volume Fraction

To determine the volume fraction of the systems we want to consider two different observables, the radial distribution function and the population of higher-order clusters. The latter is a strong function of state point and therefore allows an accurate mapping [41].

In order to obtain an exact determination, we want to analyse a system without dipolar interaction. The particles then behave like hard spheres and we can determine the volume fraction independently of the strength of the dipolar interaction, which has a significant influence on the structure of the fluid. Therefore, we investigate the start of the data set showing the fluid to BCT crystallisation (Fig. 6.7). Here, the electric field is applied suddenly to the system, and therefore, until it relaxes to the effect of the field, i.e. for the first frames, the system is initially a hard-sphere fluid. No ordering in the z-direction characteristic of this system [48, 78] could be observed (Fig. 6.3(a)). The $g(r)$ for x-, y- and z- directions lie on top of each other, which shows the isotropic character of the sample at the beginning of the measurement without the influence of the external electric field. Fig. 6.3(b), on the other hand, shows the anisotropic g(r)'s for an almost completely crystalline system in which a BCT parallel to the electric field has formed due to the dipolar interactions. It can be seen that, compared to the fluid system, there is a strong order in the z-direction, which is consistent with the structure of the BCT. Pronounced peaks can also be seen in the x- and y-directions, although they are less pronounced than in the z-direction, which is in agreement with the symmetry of the BCT crystal.

Figure 6.4(a) shows the comparison of the isotropic radial distribution function of the the first frame of the experiment and computer simulation with similar polydispersity and added artificial error in the position of the simulated coordinates to mimic the experimental data set. The experimental curve is scaled by the effective hard sphere diameter σ_{eff}. We observe good agreement between experiment and simulation, which proofs the accurate mapping of the experimental volume fraction.

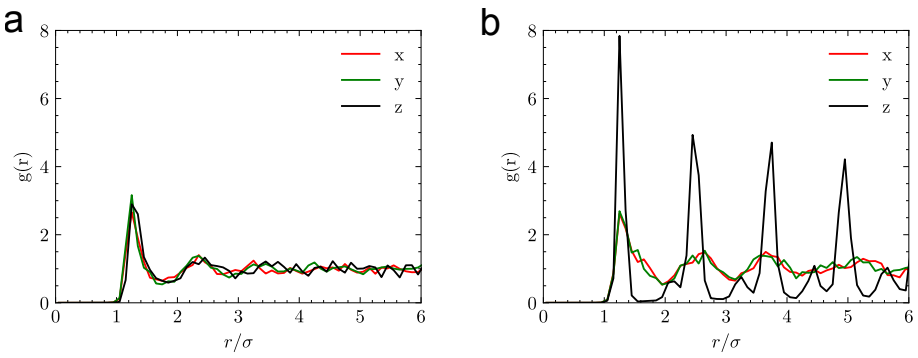

Figure 6.3: Anisotropic radial distribution function for the first frame (a) and last frame (b) of a crystallising system with $\phi_{\text{eff}} \approx 0.49$ and $\gamma \approx 52$.

Only the height of the first peak is not reproduced by the simulation. This could be explained by an overestimation of the polydispersity or localisation uncertainty. We can use the effective hard sphere diameter σ_{eff} and the number of observed particles by tracking N_{obs} in the experiment to arrive at an observed volume fraction $\phi_{\text{obs}} = N_{\text{obs}} \frac{\pi \sigma_{\text{eff}}^3}{6}$. Here we calculate $\phi_{\text{obs}} = 0.484$, which is slightly smaller than the volume fraction of the simulation $\phi_{\text{sim}} = 0.49$, because of missed particles during the particle tracking routine.

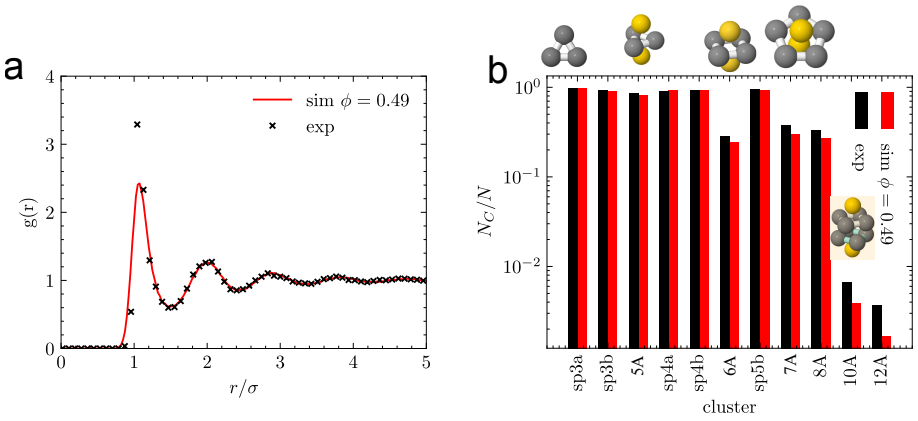

Figure 6.4: Mapping of the volume fraction. (a) Comparison of the $g(r)$ from experiments and hard sphere computer simulations with $\phi = 0.49$. Artificial experimental error was added to simulation data. (b) TCC cluster population for experiments and simulations with artificial experimental error. Rendered clusters can be seen in Fig. 6.14.

Figure 6.4(b) shows the comparison of the structure of experiment and hard sphere simulation by visualising the population of different clusters identified by the TCC. We observe good agreement between experiment and simulation for all clusters. The higher-order correlations are much more sensitive to changes in the volume fraction than the 2-point correlation function. This confirms that the state point of the samples was accurately determined and that the system resembles a hard sphere liquid at the beginning of the measurements.

Determining the Local Volume Fraction

Having mapped the experimental state point, we determine the local volume fraction by performing a Voronoi tesselation. All points in space that are closer to the center of a specific particle than to any other surrounding particle are determined forming the voronoi cell. We then divide the volume of this cell by the effective particle volume and arrive at the particle-resolved volume fraction. We can use this quantity to analyse spatial changes in the sample on a particle-resolved basis, which can be associated with changes in the macroscopic structure.

Crystal Identification

We use a structural order parameter combined with a neural network classification scheme, developed by our collaborators Fabio Leoni and John Russo [210]. They trained a neural network on bulk particle configurations of HCP, FCC and BCT crystals and liquid phases at the freezing and melting points, produced by computer simulations. Thirty different bond orientational order (BOO) parameters are used as descriptors. Through supervised learning, the model is ultimately able to identify the crystal nuclei and distinguish between the different polymorphs.

By adjusting the training data, this approach can be adapted to different model systems. Apart from hard spheres [210], the classification scheme has also been successfully applied to models of water [218] and now to systems of dipolar colloids.

6.1.3 Dipolar Colloids in Computer Simulations

We employed computer simulations using the LAMMPS package in the NPT ensemble, with some equilibration in the NVT ensemble with a Nose-Hoover thermstat (and Barostat as appropirate) [219].

Unlike the experimental system, for simplicity here we use used a monodisperse system for the simulations. To reproduce the (nearly) hard sphere behaviour of the experimental system, we use the Weeks-Chandler-Anderson (WCA) potential [220]. This takes the form:

$$u_{\mathrm{wca}}(r_{ij}) = \begin{cases} 4\,\epsilon_{\mathrm{wca}}\left[\left(\dfrac{\sigma_{ij}}{r_{ij}}\right)^{12} - \left(\dfrac{\sigma_{ij}}{r_{ij}}\right)^{6}\right] + \epsilon_{\mathrm{wca}}, & r_{ij} \leq 2^{1/6}\sigma_{ij}, \\ 0, & r_{ij} > 2^{1/6}\sigma_{ij}. \end{cases} \tag{6.1}$$

where $\epsilon_{\mathrm{wca}} = 5k_BT$ is the interaction energy and $\sigma_{ij} = (\sigma_i + \sigma_j)/2$.

We added the dipole-dipole interaction shown in Eq. 1.10, the Ewald sum which is implemented with the KSpace package in LAMMPS [219]. Here $\gamma = \gamma_{\text{sim}}$ controls the strength of the dipolar interaction. The interaction potential for the simulations then reads

$$u_{\text{sim}}(r, \theta) = u_{\text{wca}}(r) + u_{\text{dip}}(r, \theta). \tag{6.2}$$

We quote simulation results in reduced Lennard-Jones units, that is to say the unit of length is the diameter σ, and time is in units of $\sqrt{m\sigma^3/\epsilon_{\text{wca}}}$ where m is the mass of a particle. We use the Barker-Henderson effective hard sphere diameter of the WCA component of the interaction to determine the effective volume fraction ϕ_{eff} in order to match the experiments, ie $\phi_{\text{eff}} = (\pi/6V)N\sigma_{\text{eff}}$ where V is the volume, N is the number of particles and σ_{eff} is the effective hard sphere diameter.

To determine the equation of state, we are currently running NPT simulations. To prepare the crystal growth runs, we proceed as follows. We use a slab of crystal, with a fluid above and below. The crystal slab is taken from a configuration equilibrated under NPT. A columnar shaped box with a rectangular cross section is used. The system is run with periodic boundary conditions in 3D. simulations are performed in the NPT ensemble with the box fluctuations in the xy-plane decoupled from those in z.

6.2 Results

Here we present our main findings. Our data set shows a direct observation of Ostwald's rule of stages in a dipolar colloidal system, whereby an HCP crystal formed by heterogeneous nucleation melts and is ultimately replaced by the stable BCT crystal. An overview of this measurement is shown in Fig. 6.5. We will analyse the population of the two crystal polymorphs and examine the volume fraction of the crystal and the surrounding fluid separately. We find a continuous drop in the fluid volume fraction, which could destabilise the HCP crystal.

To show that HCP can indeed nucleate in such a system under similar conditions at the wall of the capillary, an example measurement was performed. To link the melting of the HCP structure with the simultaneous growth of the BCT crystal, we analyse the equation of state of the two polymorphs.

We then attempt to establish a connection between the structure of the liquid and the crystals. To do this, we examine the population of higher-order clusters first as a function of dipolar strength

and then for the transformation measurement over time. In doing so, we place particular focus on changes in the populations of clusters that are compatible with HCP and BCT symmetry.

Finally, we will investigate the spatial arrangement of the TCC clusters and attempt to find a connection between the polymorph selection and the structure of the surface of the respective crystal structure and that of the bulk fluid.

6.2.1 Ostwald's Rule of Stages in Dipolar Colloids

We present our main experimental findings in Fig. 6.5. Those are taken from a state point ($\phi \approx 0.49$; $\gamma \approx 14.5$) (Fig. 6.1(b)) where the BCT crystal is the stable phase. We find instead HCP crystal. This is presumed to have formed via heterogeneous nucleation on the sample cell wall as is well documented for colloidal systems [207].

To demonstrate heterogeneous growth of HCP induced by the capillary wall, we performed an example measurement. For this purpose, a sample with a volume fraction close to the coexistence regime ($\phi \approx 0.49$), similar to the one observed for the transition measurement, was produced and filled into the self-made capillary. For samples with a sufficiently high volume fraction, nucleation occurs immediately at the wall of the capillary while the nucleation process cannot be directly examined with confocal microscopy. We use the introduction of dipolar interaction between the particles to destroy the crystalline HCP structure. When the field is sufficiently large, the particles arrange themselves in chains and no crystal nucleus can be observed. Then the electric field is turned off and the particles interact again with the hard sphere interaction potential. Thus, nucleation starts again at the capillary wall and can be directly imaged.

Figure 6.6 shows a rendered configuration of this measurement before heterogeneous nucleation (a) and some time after the field was switched off again (b). At the beginning of the measurement, a layering can be observed for a distance of approximately two particle diameters from the capillary wall, but no crystalline structures can be identified. In contrast, Fig. 6.6(b) clearly shows the HCP structures that have grown into the sample from the wall of the capillary. Although the bottom layer is classified as BCT, we cannot trust this particular identification layer due to possible misidentifications at the edge of the microscopic image. The neural network was trained solely on systems with periodic boundary conditions, so misidentifications may occur at the edges. We have thus demonstrated that HCP structures can crystallise through heterogeneous nucleation.

Back to our main result (Fig. 6.5), after some time (here around 3000 τ_B), the HCP crystal starts

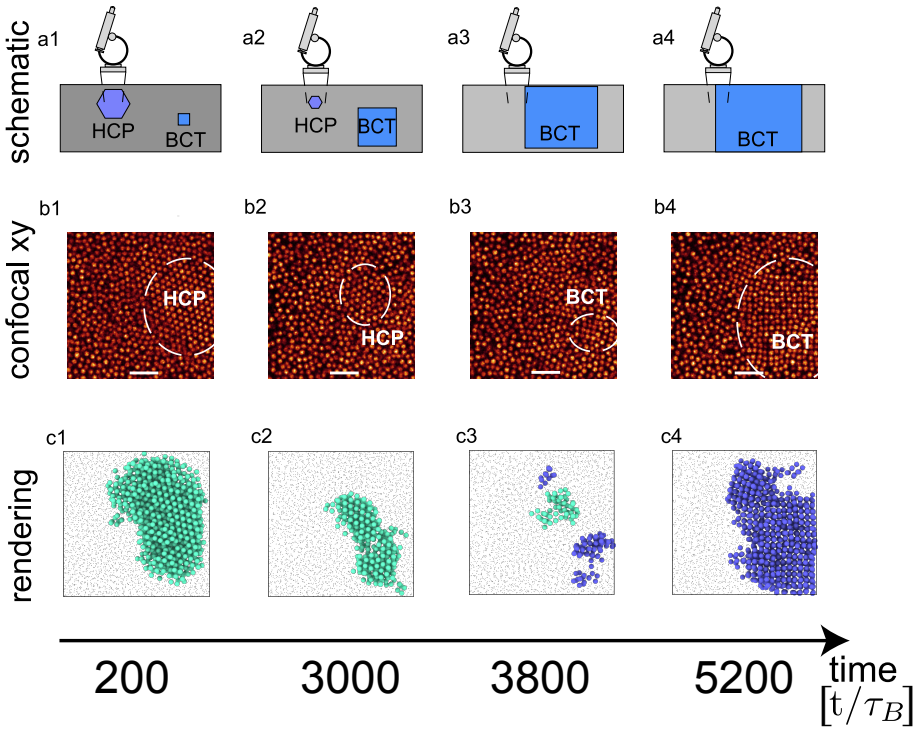

Figure 6.5: Ostwald's rule of stages in dipolar colloids. (a) schematic sequence showing Ostwald's rule of stages at the macroscopic level. This is inferred from microscopic observation of the system. (b) Sequence of confocal microscopy images in the xy-plane (perpendicular to the electrical field). (c) Renderings of particle-resolved data with crystals indicated. Bright particles are in the HCP crystal and dark ones in the BCT crystal. Liquid particles are depicted smaller.

to melt and is finally (after melting) replaced with a BCT crystal at around 3800 τ_B. Here the Brownian time for a particle to diffuse its own diameter $\tau_B = 6.09$ s [78]. The evolution of the crystal population of the two polymorphs is shown in Fig. 6.7(a). Initially, the system is dominated by HCP. Only after the crystal disappears does the population of BCT increase dramatically. This is evidence for the Ostwald rule of stages via Ostwald ripening.

While macroscopic observations might show similar global behaviour, our data at the single particle level enable us to probe the local mechanism for the melting of the HCP crystal. We see in Fig. 6.7(b) that the volume fraction of the fluid surrounding the crystal drops over time. This we infer is due to growth of a BCT crystal in a region of the system that is not imaged.

Now the BCT is at a higher volume fraction than the fluid at this state point (Fig. 6.1(b)). Since the entire system is in a sample cell the total number of particles is constrained and so the increase in volume fraction associated with the growth of the BCT results in the observed drop in volume fraction of the fluid. The drop in fluid volume fraction, acts to destabilise the HCP crystal at a higher pressure (and hence higher volume fraction) than for the BCT crystal.

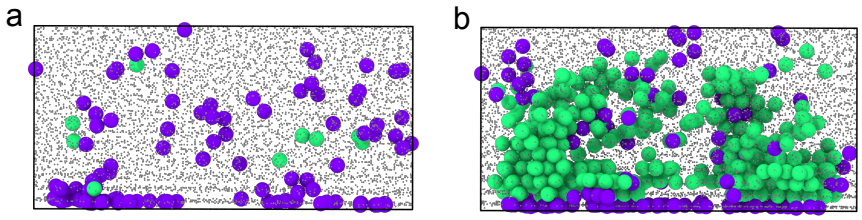

Figure 6.6: Heterogeneous Nucleation at capillary walls. Dark particles in BCT and bright particles in HCP (a) Configuration immediately after turning off the electric field. (b) Configuration after leaving the sample for approximately 10 minutes. Liquid particles are depicted smaller for clarity.

We are currently running computer simulations to determine the equation of state for the fluid and the two crystal structures. The results obtained so far, which are shown schematically in Fig. 6.8, lead to the following conclusions. The equation of state show a clear drop in pressure as the volume fraction is reduced, for the fluid and for both crystals (Fig. 6.8). We are furthermore computing the equation of state for the crystals. Although it is metastable the HCP is nevertheless able to grow at the expense of the fluid for $P > 5$. Crucially, as shown in Fig. 6.8, while HCP stops growing at pressure $P = 5$, BCT continues to grow until $P = 4$. Thus there is a regime of pressure - and hence volume fraction - where BCT grows but HCP does not. This could explain why the HCP melts in the experiments, but the BCT grows.

As a comparison, at higher field strength, the relative stability of the HCP and BCT is presumably different, and the BCT formed via "spinodal crystallisation", i.e. where there is a very small energy barrier to nucleation and crystallisation.

6.2.2 Liquid Structure

We now investigate how the local structure of the fluid may control the polymorph selection. To identify higher-order structures characteristic of the fluid, we use the topological cluster classifier

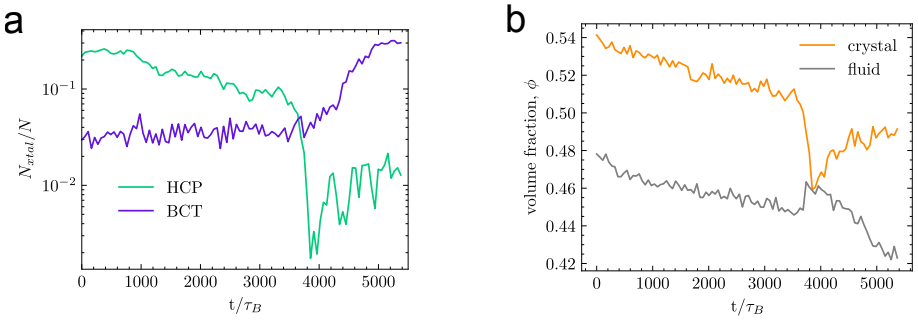

Figure 6.7: Characterisation of HCP-BCT transformation. (a) Change in Crystal population of HCP and BCT. (b) Change in fluid volume fraction during the HCP-BCT transformation.

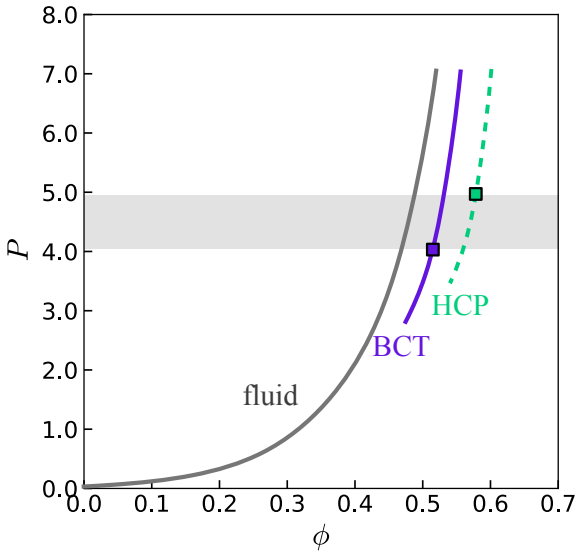

Figure 6.8: Schematic representation of the equation of state for fluid, BCT and HCP. These are not valid data, but the picture currently proposed by computer simulations. The data points on the crystal branches represent the lowest pressures at which the two crystals still grow. Grey area is regime of pressure (volume fraction) where BCT grows but HCP does not.

(TCC) [163]. Examples of clusters to be identified are shown in Figure 6.14. The first column represents minimum energy clusters of 7 to 13 particles for a Lennard-Jones system. Each subsequent column shows the minimum energy cluster for the identical number of particles, but for increasing dipolar strength. We see that the particles tend to form stretched clusters until, for very high dipole strength, a chain becomes the minimum energy arrangement of the particles.

Some clusters, such as the 7A cluster, are associated with the suppression of crystallization [34, 164], as the pentagonal bipyramids do not stack to fill the 3D space. In the past, the influences of liquid structures on, for example, polymorph selection have been investigated [52]. A previous study already showed that changing the electric field and thus the dipole interaction strength alters the cluster population [78]. We hope to find a similar connection between the structure of the liquid and the formation of specific crystal polymorph.

In addition to the data set discussed above, which shows Ostwald's rule of stages, we also conducted experiments with higher dipolar strength. Here we observe instant freezing of the fluid into BCT. Figure 6.9 shows an overview of this high dipole strength measurement. At the beginning, only a small number of isolated particles are identified as BCT. However, the crystal domains grow rapidly and after approximately 150 τ_B, a large part of the system has crystallized, as shown by the population of particles identified as crystalline in Fig. 6.9(b-c). We have also calculated the volume fractions of the crystal and fluid phases separately and see a constant value of $\phi_{\mathrm{xtal}} = 0.46$ and a continuously decreasing value for ϕ_{liq}. It should be noted that the calculated volume fractions are

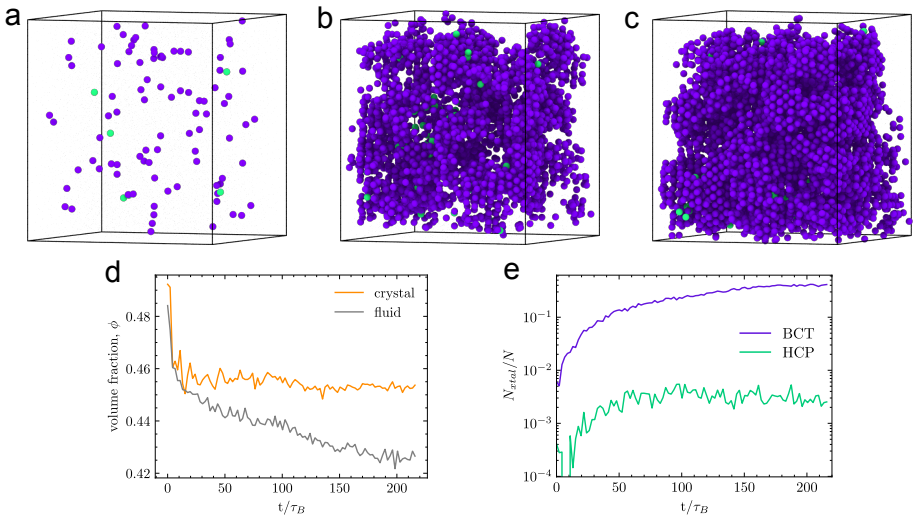

Figure 6.9: Fluid-BCT crystallisation measurement. (a-c) Rendered particle configurations at the beginning (a), in the middle (b) and at the end (c) of the measurement. Purple particles are considered to be in BCT crystal. Bright particles are identified as HCP. (d) Volume fraction of Crystal and Fluid during the measurement. (e) BCT and HCP population as a function of time.

based on Voronoi tessellation and are therefore strongly dependent on the effective particle diameter σ_{eff}. This is difficult to determine for the system under investigation, which is why a relatively large systematic error of approximately 1% must be taken into account in the determination of the volume fraction. We can now use the TCC to compare the structure of the fluid phase for hard spheres with systems of weak and strong dipole strength.

Figure 6.10 shows a comparison of the populations of different higher-order clusters identified with the TCC. It can be seen that the population of clusters characteristic for the Lennard-Jones system decreases with increasing dipolar strength. In contrast, the populations of the clusters stretched along the electric field show an increase for higher dipolar strengths, as expected. We have found that as the dipolar interaction increases, clusters such as 8O that are compatible with the BCT crystal are favored.

Now that we have characterized the structure of liquids depending on the strength of the dipolar force, we want to investigate the change in fluid structure during the transformation from HCP to BCT. Figure 6.11 shows the evolution of different TCC cluster populations during the experiment. At the beginning of the experiment, a large HCP crystal is present in the microscopic image. We can observe a high population of clusters that are compatible with this crystal structure in the liquid surrounding the nucleus. As the HCP structure melts, the population of 4-membered rings increases. Interestingly, an increased occurrence of the 7A cluster (pentagonal bipyramid) can also be observed. However, the population then decreases with crystallization of the BCT nucleus

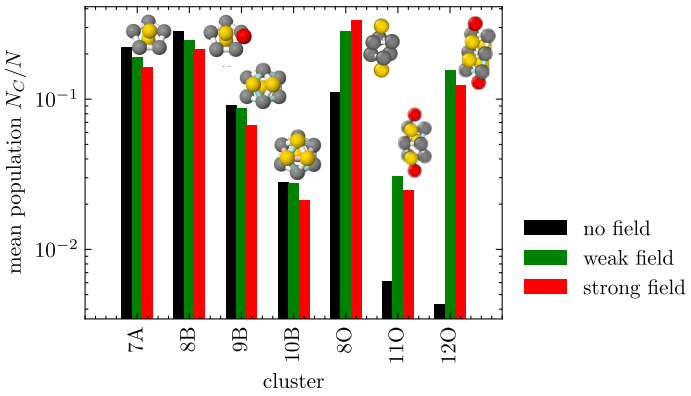

Figure 6.10: Comparison of the Population of higher order structures identified by the TCC, for hard spheres (no field) and weak/strong dipole interaction.

($3900\tau_B$). Overall, it can be said that the structure of the liquid surrounding the HCP and BCT crystals does not undergo any major changes during the transformation process.

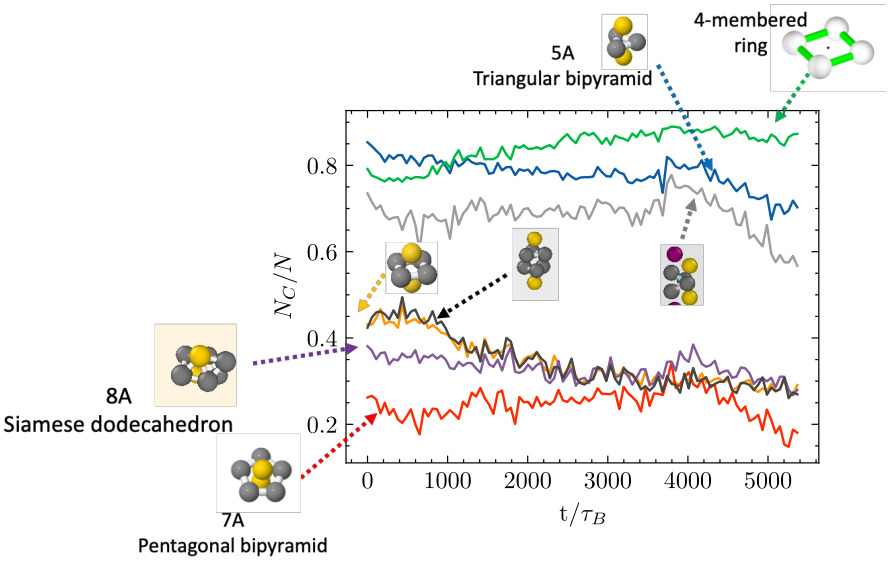

Figure 6.11: Temporal evolution of the fluid structure by analysing the population of a subset of TCC clusters during the transformation from HCP to BCT. Each colour represents a different cluster type.

Nevertheless, overall clusters that are more compatible with the existing crystal structure are becoming more prevalent. Since the temporal course of the structural change provides little insight into the underlying processes of Ostwald's rule of stages, we will now turn our attention to spatial analyses.

In addition to the averaged population of different higher-order clusters in the fluid surrounding the various crystal polymorphs, we can also analyse the position of these clusters relative to the position of the crystal nuclei. For this purpose, we introduce a new value that can be calculated for

each individual particle. The TCC identifies clusters of different sizes, whereby individual particles can be part of several clusters of the same type. We define the total number of identical clusters in which a single particle participates in (Fig. 6.12). We then determine the minimum distance for each particle to a particle that has been identified as part of a crystal structure and can use this information to estimate the number of clusters as a function of the distance to the surface of the crystal.

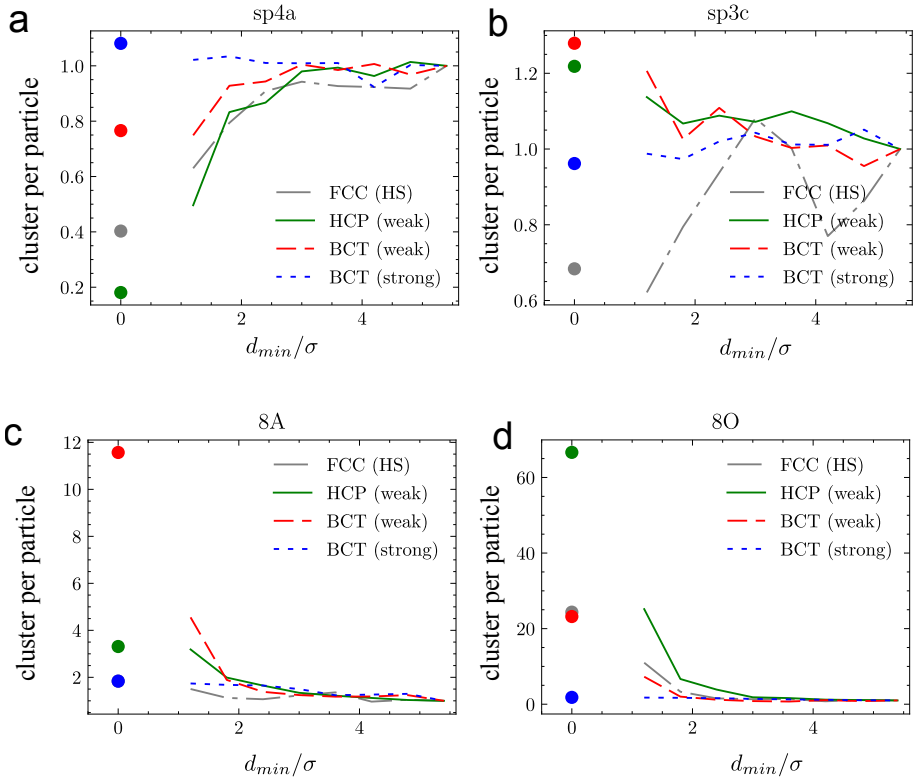

Figure 6.12: Number of clusters of a specific type a single particle participates in as a function of the minimum distance from a crystal nucleus. Values are normalized with the number of clusters we find for a particle in the bulk fluid. We compare the structure of the fluid surrounding different crystal polymorphs for a hard sphere system (FCC), weak dipole strength (HCP and BCT) and strong dipole strength (BCT).

Figure 6.12 shows this total number of clusters for each particle, binned and normalised by the average number of clusters we can find for a particle in the bulk fluid. For $d_{\min}/\sigma = 0$, the normalised number for a particle that is part of the crystalline nucleus is shown. This allows us to determine which cluster types are compatible with which crystal polymorphs. We can see that the 4-membered ring (sp4a) is compatible with BCT, but not so much with HCP and FCC. For HCP and FCC, significantly fewer of these clusters are found in the crystal than in the liquid surrounding it. With this representation, we can also determine which cluster types occur most frequently at the boundary between crystal and fluid. Of interest to our system is the distribution of the 8O cluster. This is compatible with HCP and should also be compatible with the BCT structure. We

find that this cluster occurs more frequently at the boundary between HCP and fluid, or BCT and fluid, but only in the case of weaker dipolar interaction. For the system with strong interaction, no change in occurrence compared to bulk fluid can be observed. This could result from the increased presence shown in Fig. 6.10, whereby the structure of the fluid adapts to the crystal.

The increased occurrence of 8O at the boundary between HCP and fluid is also evident when the particle configuration is rendered and the cluster number of each individual particle is highlighted in colour. Figure 6.13(a3/b3) shows the particle-resolved representation of the occurrence of 8O. HCP and BCT are marked in light and dark blue. It can be clearly seen that, in contrast to the BCT crystal at the end of the measurement, the HCP crystal is surrounded by a layer of 8O.

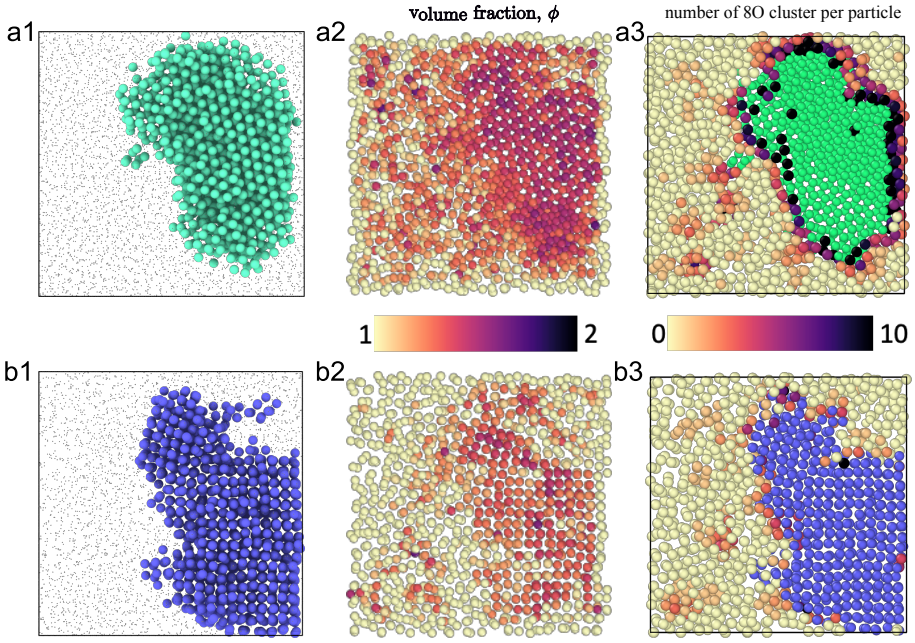

Figure 6.13: Particle resolved volume fraction and cluster population for configurations with HCP (a) and BCT (b) crystals. (a1) HCP crystal. (b1) BCT crystal. (a2, b2) Particle resolved volume fraction. (a3, b3) Number of clusters each particle participates in.

We also determined the particle-resolved volume fraction based on Voronoi tessellation and visualised it in Fig. 6.13(a2/b2). As expected, the crystalline domains show a significantly higher local volume fraction. In addition, more fluctuations can be seen at the beginning of the measurements in the fluid surrounding the HCP crystal. The stable BCT crystal is surrounded by a fluid with a significantly lower volume fraction.

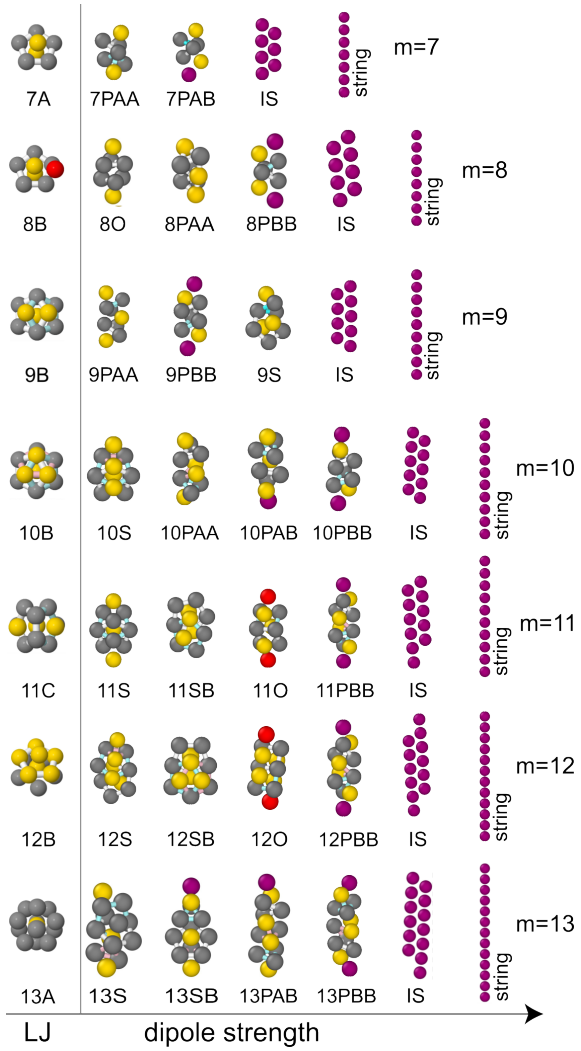

Figure 6.14: Dipolar clusters identified by the TCC. The first column shows the minimum energy cluster for the Lennard-Jones system. Each subsequent column shows the minimum energy cluster for increasing dipole strength [163].

6.3 Conclusion

We have found a model system for investigating Ostwald's rule of stages in a system of dipolar colloidal particles. Our central experiment shows how an HCP crystal, formed by heterogeneous nucleation, slowly melts and is replaced by a BCT crystal. We found that the melting process is caused by the simultaneous nucleation of the BCT crystal in another region of the sample and the associated decrease in the volume fraction of the fluid. From calculation of the equation of state for the fluid and crystal a regime of pressure, or in experiments a regime of volume fraction, in which the BCT crystal grows and the HCP does not, becomes evident.

We then compared the structure of the fluid with weak and strong dipole strength using the hard

sphere system and found that, as expected, the population of stretched clusters (minimum energy arrangements) increases with increasing dipole interaction. The evolution of the population of higher-order structures in the fluid was analysed and we found clusters compatible with the BCT crystal structure in particular increase during the measurement.

The spatial structure of the fluid was analysed as a function of distance from the various crystal nuclei. We found that the 8O cluster, which is compatible with HCP and BCT, is particularly prevalent at the boundary between the crystal and the fluid. Finally, visualisation of the particle-resolved volume fraction showed that the more stable BCT crystal is surrounded by a fluid with lower volume fraction compared to the HCP nuclei at the end of the data set and that the fluid also exhibits smaller density fluctuations.

In general, we were able to directly record the process of Ostwald's rule of stages in a model system of dipolar particles for the first time. The particle-resolved data allowed us to shed light on the underlying process, connecting the occurrence of different polymorphs with the structure of the surrounding fluid.

Chapter 7

Optimizing Self-Assembly in a Colloidal Model System

The experiments were designed and carried out by the author of this thesis. Antoine Castagnède developed the code for identifying the crystal nuclei. All data were analysed by the author. This project was carried out in collaboration with Frank Smallenburg's research group, where the protocols shown below are implemented in computer simulations to reproduce the experimental results.

As has become clear in the previous chapters, the investigation and prediction of nucleation events and crystallisation is still the subject of ongoing research in various scientific fields [1, 21]. Here, we want to go one step further and attempt to control and optimise the self-assembly process in colloidal model systems.

The idea of optimising the crystallisation process is not new. In the pharmaceutical industry, for example, crystallisation is a critical step in the manufacture of active pharmaceutical ingredients (APIs), which determine the purity, polymorphic form, crystal size, and morphology of the final product. These properties have a strong influence on the bioavailability or stability of drugs [221, 222]. Poorly controlled crystallisation can lead to undesirable polymorphs, a wide distribution of crystal sizes, and inconsistent product quality, which has an impact on the potency of drugs and the effectiveness of the manufacturing process [223]. In modern manufacturing, feedback control schemes are used to adjust the temperature, supersaturation, and solvent composition in real time during the crystallisation process. This makes the formation of large, defect-free crystals reproducible and more efficient by incorporating controlled growth and annealing steps that allow

defects to heal and crystals to mature [221].

Previous numerical studies with colloidal particles interacting via a short-ranged attractive potential showed that in these systems there is an optimal self-assembly path that is characterised by a trade-off between forming the stable ordered phase and reversibility of bonding to compensate for defects. They showed that optimising the interaction parameters during self-assembly can lead to formation of larger crystal domains without defects. With a real-time feedback scheme, particle interactions are automatically adjusted during the assembly process. They found that an optimised protocol involves strong bonds at the beginning to promote nucleation, and weaker bonds at later stages to promote rapid Ostwald ripening. [54–56, 224].

Another numerical study used Brownian dynamics computer simulations to investigate the influence of the quench rate on gelation through *in situ* changes of the interaction potential. For lower quench rates, the population of large structures in the gel increases, and for the slowest quench rate investigated, crystallisation was even observed in the system [225].

Here we want to analyse and optimise the self-assembly of a dipolar colloidal model system by systematically changing the strength of the dipolar interaction during the nucleation process. The dipolar system under investigation is characterised by an attractive interaction between particles along the direction of the electrical field and repulsion in the perpendicular direction [48]. High field strengths lead to immediate assembly in strings in z-direction, but less mobility in xy-direction. A schematic representation of the dipolar forces and the corresponding phase diagram is shown in Fig. 7.2.

We performed experiments with simple step-protocols, oscillating electrical fields, continuously increasing dipolar strengths and high-to-low protocols (schemes are shown below). A schematic representation of the different protocols is shown in Fig. 7.1.

We analysed the nucleation process by considering the averaged crystal population N_{xtal}/N, size of the largest crystal domain S_{max}, number of crystal domains N_{nuclei} and population of different higher-order structures during the nucleation process N_C/N, identified with the above introduced topological cluster classification (TCC). The crystal particles were identified by a simple bond orientational order parameter based on the work of Steinhardt [161] already introduced in Chapter 2.4.3. Then nuclei were distinguished from each other to be able to measure the averaged nuclei number and size of the largest crystal nucleus in the system. The overall goal is to optimise the duration of crystallisation and to increase the maximum domain size.

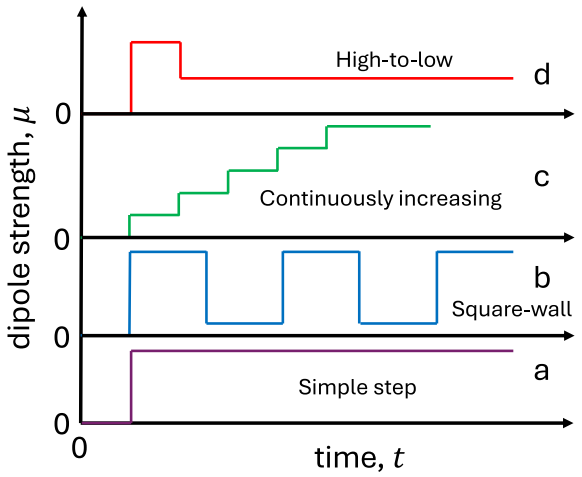

Figure 7.1: Schematic representation of the different protocols of the dipole strength we analysed. (a) Simple step protocol. (b) Square wall protocol with oscillating dipolar strength. (c) Protocol with continuously increasing dipole strength. (d) High-to-low protocol. Protocols are offset for clarity. All experiments start with a period without external field $\mu = 0$.

7.1 Material and Methods

Here we want to briefly explain how the system of dipolar colloids is realised in experiments and how we mapped the volume fraction and dipole strength separately to computer simulations.

7.1.1 Colloidal Model System with Dipole Interaction

Colloidal particles with dipolar interactions, due to an applied external electrical field, show an interesting phase behaviour and assemble in a variety of different structures [48, 51]. A detailed description of the interaction potential and phase behaviour can be found in Chapter 1.4. Since this work is being done in collaboration with Frank Smallenburg's group, which is performing computer simulations similar to the experiments, the dipole strength will not be described here in terms of γ but rather in terms of a closely related quantity defined as

$$\mu = \frac{1}{2}\sqrt{2\gamma}, \tag{7.1}$$

where μ is often used in the simulation package LAMMPS to describe the dipolar interactions. Another reason is the high dipole strengths we have induced for different protocols. Since μ scales with the square root of γ, we can better compare and visualize different protocols with each other. Figure 7.2 shows a schematic representation of the dipole interaction and the phase diagram for the dipole strength μ with our experimental state points.

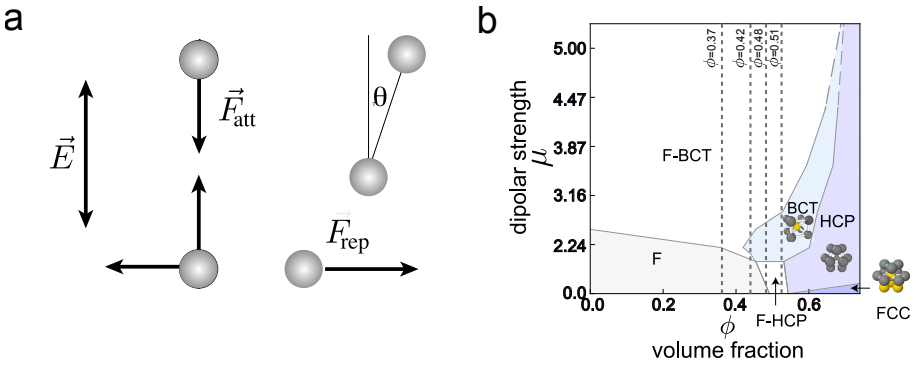

Figure 7.2: Dipole interaction and phase diagram. (a) Schematic representation of dipole interaction with attraction in the direction of the electrical field and repulsion perpendicular to it. (b) Phase diagram of a model system with dipole interaction and experimental state points. Reproduced from [51].

The system used consists of PMMA particles with a diameter of $\sigma = 2$ μm and polydispersity of 4% suspended in a density and refractive index matched mixture of decalin, tetralin and CHB. We added TBAB salt to the solvent to screen residual charges on the surface of the particles. More detail can be found in Chapter 2.1. Here we investigated systems with volume fractions $\phi = 0.37$, 0.42, 0.48, and 0.51 with confocal microscopy to image the sample in 3D and extract particle-resolved data. The Brownian time of the particles is $\tau_B = 9.6$ s and the frame duration for the experiments is roughly 4.5 s.

7.1.2 Construction of the Sample Cell

To apply an external alternating electrical field to the system, we use a special, self-constructed sample cell. It consists of an ITO covered cover slip (SPI supplies, thickness 0.13 to 0.17 mm, resistance 8 to 12 Ω) and an ITO covered microscopic slide separated by spacer tape of various width ($50 - 110$ μm). Figure 7.3 shows a schematic representation of the sample cell used. The ITO covered glass slides are connected to a signal generator (type) and a 20x amplifier by short wires that are attached to the ITO side of the cover slip. Everything was affixed by Norland Optical Adhesive 61. Norland Optical Adhesive 61 was also used to seal the sample cell. Before filling the capillary the adhesive was applied on the inside of the spacer tape to separate it from the sample. After filling the sample cell both ends were again sealed with 2-3 layers of Norland Optical Adhesive 61.

One has to be very careful with sealing the sample cell at the two ends after loading the sample, because in some of the systems a strong particle drift toward one of the ends of the capillary was observed. Due to the leak, these samples dried out after a short time and are not included in the

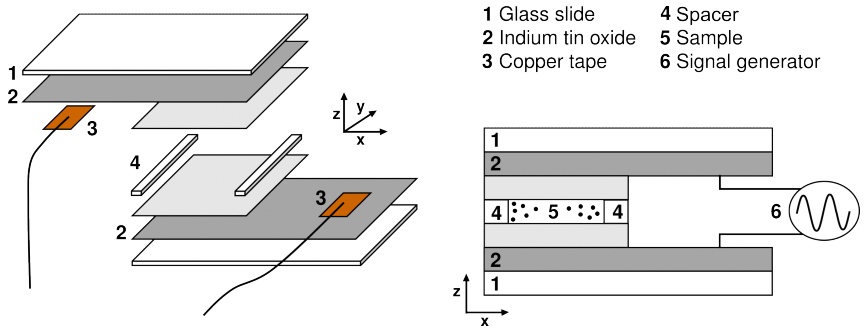

Figure 7.3: Sketch of sample cell for experiments with dipolar colloids. Tape with different thicknesses was used as a spacer ($50 - 110$ μm). Reproduced from [104]

following analysis. Another critical factor for the quality of an experimental cell was the width of the constructed capillary. If during the construction pressure was applied only on one side, the two electrodes were not perfectly parallel, leading to a field gradient and particle drift [226, 227]. This was tested by measuring the height of the capillary at 3 different positions in the cell. Samples with this construction error are also not considered in the following.

7.1.3 Mapping Experimental State Points to Simulation

To be able to compare observables from experiments and simulations one has to be sure that the systems are at the same state point. For dipolar colloidal systems the phase behaviour is determined by two control parameters, the well-known and already introduced volume fraction ϕ and the strength of the dipole moment μ. How to map the experimental state point to computer simulations is described in detail for both control parameters in the following.

Volume Fraction

The performed experiments followed different field strength protocols, but they all started with a period of no applied external field ($\mu = 0$) for roughly two Brownian times. During this period the sample behaves like a hard sphere system. As explained in Chapter 2.4.1 the hard sphere system is very well characterised by the isotropic pair correlation function $g(r)$ and the population of higher order clusters. We use these values to determine the volume fraction ϕ of the experimental system by comparing it to hard sphere computer simulations with artificial tracking error. Figure 7.4(a) shows a comparison of the experimental $g(r)$ and the one calculated from computer simulations with volume fraction $\phi = 0.48$. The curves and calculated volume fraction for the experiments by counting particles are in very good agreement. This shows, that the state point of the system is

well characterised, and that the tracking with "Colloidoscope" is very accurate giving the correct number of particles.

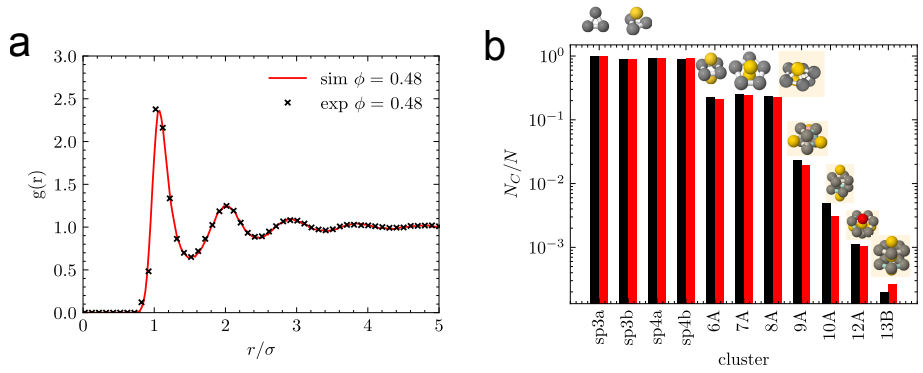

Figure 7.4: Mapping volume fraction for dipolar systems without electrical field. Without an electric field, the particles interact like hard spheres, which allows us to determine the volume fraction independently of the strength of the dipolar interaction. (a) Comparison of g(r) for first frames of experiments without dipolar interactions (hard spheres) to computer simulations with artificial tracking error. (b) Comparison of population of different TCC clusters from experiments (first frame with hard sphere configuration) and hard sphere computer simulations with artificial tracking error. At this point, we are not interested in the significance of certain clusters for the self-assembly process. For this reason, clusters for model systems that are not relevant for the dipolar system are also included.

Figure 7.4(b) shows the population of various TCC clusters and again demonstrates excellent agreement between experiments and computer simulations. In summary, we are confident that the state point in terms of the volume fraction ϕ is precisely determined by comparing radial distribution function and structure of the hard sphere fluid by analysing the population of higher-order clusters via the TCC.

However, in general we consider the behaviour of the dipolar system to be dominated by the dipolar interaction strength, which justifies a higher tolerance to measurement uncertainties of the volume fraction. Also, to get more statistics for a given state point, experiments are grouped by similar averaged volume fractions.

Dipolar Strength

To map the dipolar strength μ between experiments and simulations we analyse systems with a lower volume fraction of $\phi = 0.2$ in the string-fluid regime. To characterise the alignment of the particles into strings along the direction of the electrical field we use the string fluid order parameter ($\langle \cos^2 \theta \rangle$). It is defined as the average angle that particles form with their nearest neighbours. The inset of Fig. 7.5 shows a sketch of the angle θ formed by the nearest neighbours. Closest particles were identified by a simple iterative algorithm.

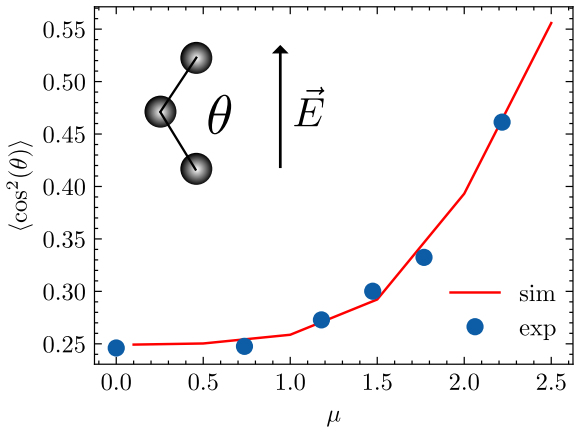

Figure 7.5: String fluid order parameter ($\langle\cos^2\theta\rangle$) as a function of the strength of the dipole moment μ for a system with volume fraction $\phi = 0.2$. The angle θ is defined by the centre particles and the two nearest neighbours.

A comparison of the string fluid order parameter for experiments and computer simulations is shown in Fig. 7.5. We find good agreement between experiments and simulation after scaling the experimental dipolar strength by a factor of 0.67. For a volume fraction of $\phi = 0.2$ the phase boundary between string fluid and fluid-BCT coexistence regime lays at approximately $\mu = 2.24$. We could not see any signs of crystallisation on the time scale of the experiments and consider the systems with the highest field strengths to be metastable.

After mapping the volume fraction and the field strength we are now in a position to investigate and compare the nucleation process of different protocols of dipolar interactions.

7.2 Results

Here we want to show the main findings of this chapter. After carefully determining the volume fraction and dipole strength of the experiments by comparing them with computer simulations, we will now examine the crystallisation for the various protocols. First, we examine different volume fractions using the simple step protocol. Then, detailed investigations of systems with volume fraction ($\phi = 0.48$) are carried out, measuring the average number of particles in a crystalline environment and the size of the largest crystal domain in the system over time for the different protocols. Finally, we attempt to determine an optimal protocol by comparing the various results and measuring the population of higher-order clusters.

Figure 7.6 shows rendered configurations for crystallisation at high and low dipolar strength. The particles in the liquid environment (grey) are depicted smaller in order to be able to recognise

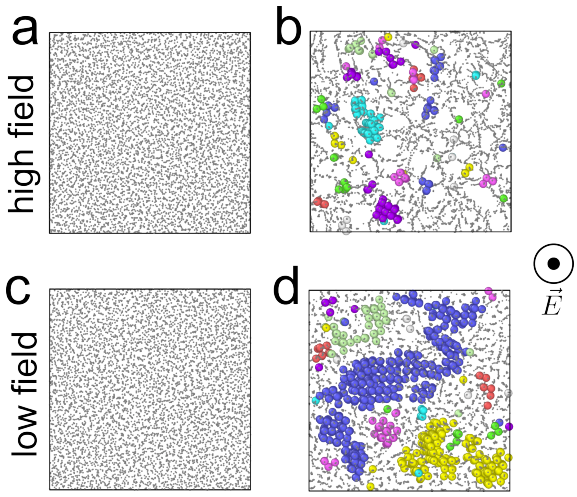

Figure 7.6: Rendering of crystal domains in dipolar colloids, viewed along the electric field direction from above the sample. Top shows crystallisation for high field strength and bottom for low field strength. (a,c) Configuration before applying the field (hard spheres). (b,d) Configurations after crystallisation. Coloured particles are in a crystal environment. Particles with the same colour are considered to be in the same crystal domain. Liquid particles are grey and depicted smaller for clarity.

structures in the system volume. The left side shows the configurations before the electric field is applied and no order can be recognised, identical to the system of hard spheres. The right side shows configurations in which coloured particles are in a crystalline environment. Particles of the same colour are considered to be in the same crystal domains. It can be seen that string-like structures form after the electric field is applied, and that the two crystal processes differ in terms of domain size.

7.2.1 Different Protocols

Step Protocol

First, a simple step protocol is considered for different volume fractions. We always leave the system to equilibrate at zero field strength for at least 5 minutes to regain the structure of a simple hard sphere fluid. After that the measurement is started, still without an electrical field ($\mu = 0$), we use the first frames to extract the volume fraction of the system. After 10 frames ($5\tau_B$) the field is turned on immediately to different values ($\mu = c$) resulting in a simple step function in μ.

The protocols for experiments with the smallest volume fraction $\phi = 0.37$ are shown in Fig. 7.7(b). From this first simple approach we see that for the smallest dipolar strength ($\mu = 2.41$) the system is not crystallising on the time scale of the experiments. By increasing the dipolar strength μ, and

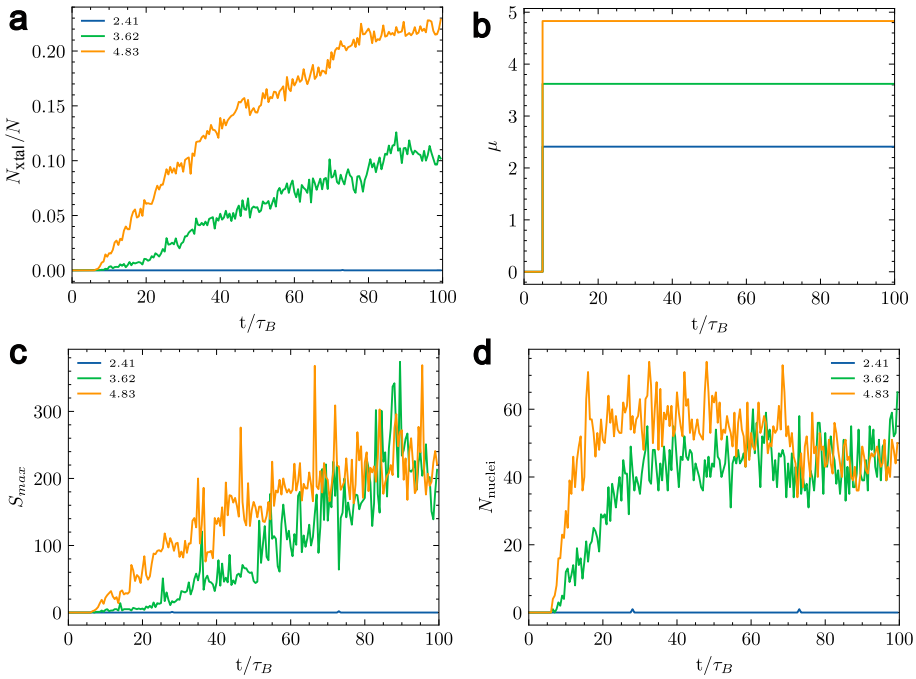

Figure 7.7: Crystallisation of a dipolar system with $\phi = 0.37$ with a simple step protocol ($\mu_0 = 0,\ \mu_1 = c$). (a) Number of crystal particles N_C normalized with the total number of particles N as a function of time. (b) Time-resolved protocol for dipolar strength μ. (c) Size of the largest crystal nucleus in the system. (d) Number of crystal nuclei in the system.

with that going deeper in the BCT regime of the phase diagram (see Fig. 6.1), we see faster increase in the normalized number of particles in a crystal environment (Fig. 7.7(a)). This could be expected, as the high dipole strength makes the particles quickly form string-like structures and arrangements compatible with the BCT crystal, as discussed in the previous chapter. When considering the evolution of the size of the largest crystal nucleus (Fig. 7.7(c)) and the total number of nuclei in the experimental image (Fig.7.7(d)) one can obtain two different stages of crystal nucleation. After an initial stage of separate formation of a lot of crystal nuclei, N_{nuclei} plateaus and after a certain time decreases which can be associated with merging of individual crystal nuclei.

We now want to consider slightly higher volume fractions of $\phi = 0.42$ to 0.51 with similar step-protocols, but higher dipolar strengths. The results are shown in Fig. 7.8. For small to moderate values in μ, we see a similar behaviour of increased nucleation with increasing dipolar strength. However, it can be observed that above a limit value μ_{crit} the nucleation proceeds more slowly. This shows for the first time an optimisation possibility in crystal formation of dipolar colloids. The experimental images show that for values above μ_{crit}, the particles quickly orientate into chains along the electric field, and these chains then slowly come together and form well-separated domains of BCT. Interestingly we also see an increase in the threshold value μ_{crit} with increasing volume fraction as can be seen from Fig. 7.8(g) and (h) where optimum assemblies of the three analysed

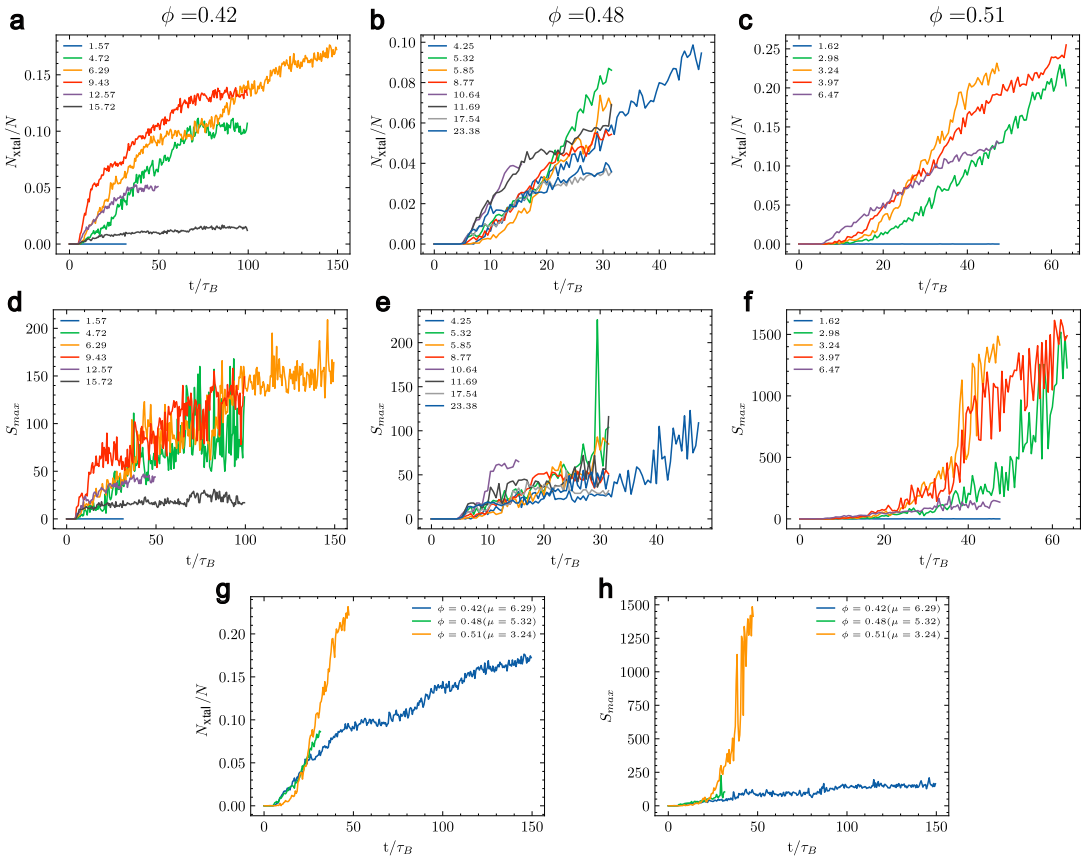

Figure 7.8: Crystallisation of a dipolar systems with $\phi = 0.42$, 0.48, and 0.51 with a simple step protocol ($\mu_0 = 0,\ \mu_1 = c$). Different colours represent different dipolar strengths. (a-c) Number of crystal particles N_C normalized with the total number of particles N as a function of time. (d-f) Size of the largest crystal nucleus S_{max} as function of time. (g-h) Comparison of the optimum step-protocol for different volume fractions.

volume fractions are compared.

In the following we will exclusively investigate data sets with volume fraction $\phi = 0.48$, just outside the coexistence regime for hard spheres. No nucleation of HCP / FCC and no heterogeneous nucleation introduced by the capillary walls was observed for these samples.

Square Wall Protocol

Having analysed simple step protocols, we now study somewhat more sophisticated functions in μ with fluctuating values in the dipolar strength for samples with volume fraction $\phi = 0.48$. The oscillating field is defined by the maximum and minimum dipole moment and the two time intervals the different values are applied for. We start with investigating the influence of the time duration of the minimum dipolar interaction strength on the self-assembly and then go to protocols with different maximum and minimum values.

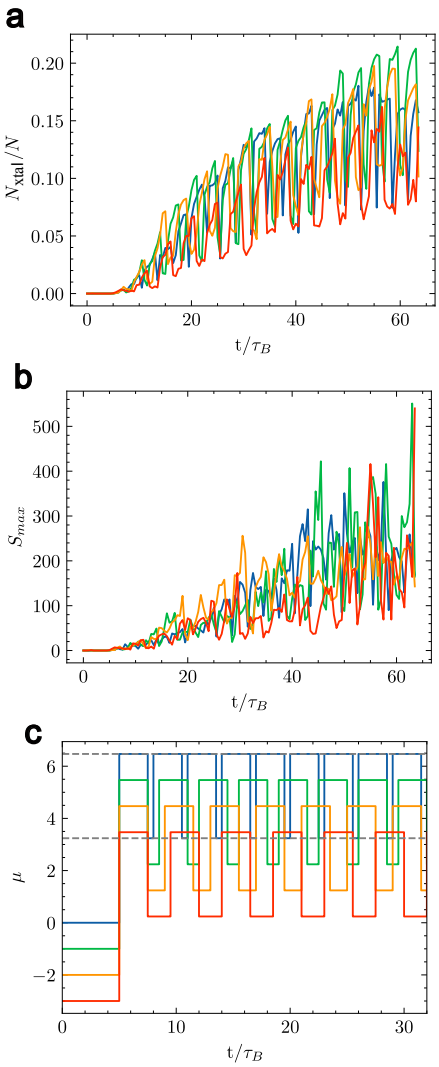

Figure 7.9: Crystallisation of system with square wall protocol of dipolar strength. (a) Crystal population as a function of time for different protocols. (b) Evolution of the largest crystal nucleus in the system. (c) Fluctuation-Protocol applying $\mu_{\mathrm{min}} = 3.24$ and $\mu_{\mathrm{max}} = 6.47$ for a system with $\phi = 0.48$ for different time. The curves are offset for clarity.

Examples of protocols with identical interaction strengths ($\mu_{\mathrm{min}} = 3.24$ and $\mu_{\mathrm{max}} = 6.47$) and differing time intervals ($0.5\tau_B$ to $2\tau_B$) applying μ_{min} are shown in Figure 7.9 (c). The curves are offset for clarity. Figure7.9 (a) and (b) show the crystal population and size of the maximum crystal nucleus as a function of time for the different protocols. One can see that there is an optimum protocol allowing the particles to form large clusters for a μ_{min} duration of $1\tau_B$ (green line). Even though the crystal population for all protocols is comparable the size of the largest crystal is at least 2 times larger compared to the worst case, where we applied the minimum field the longest. This could be explained by melting effects and a huge loss of crystallinity during the phase of applying μ_{min}. The optimum phase trajectory is characterised by a compromise of forcing the system to form ordered structures with high dipolar interaction strength and the mobility of the particles and

strings they formed.

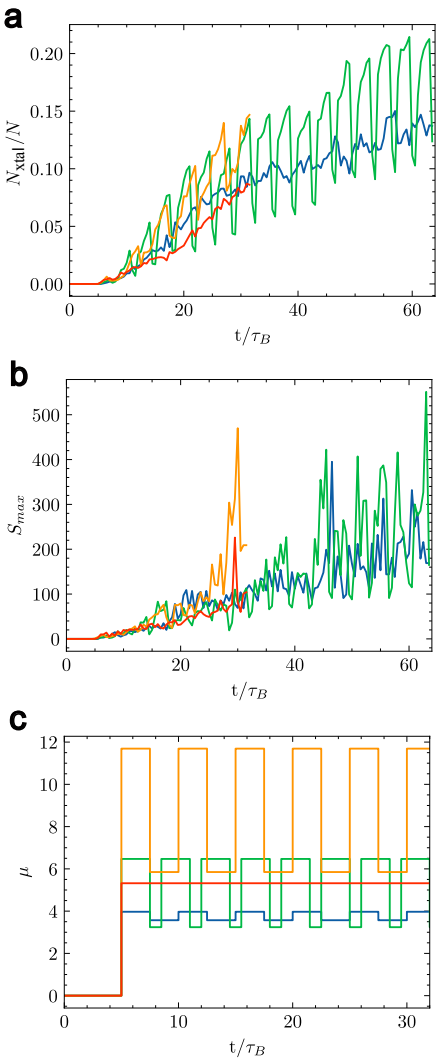

Figure 7.10: Crystallisation of system with square wall protocol of dipolar strength. (a) Crystal population as a function of time for different protocols. (b) Evolution of the largest crystal nucleus in the system. (c) Fluctuation-Protocol for different $\mu_{\min}$ and $\mu_{\max}$ for a system with $\phi = 0.48$.

Now we want to compare that optimum case to other fluctuation protocols characterised by different values of $\mu_{\min}$, $\mu_{\max}$ and durations. Figure 7.10 (a) and (b) shows the evolution of the crystal population and largest cluster size for those protocols (Fig.7.10 (c)). One can see that the number of crystal particles increases similarly for all the protocols, but the size of the largest nucleus is more strongly influenced. Even though the strongest interaction potential produces a big crystal after a very short time (yellow line) the best assembly can be observed again for fluctuations between moderate and high field strength forcing the particles to crystallise while allowing periods of nucleation with more mobility leading to merging of smaller crystal domains into large crystal nuclei of more than 400 particles. Compared to the optimum crystallisation with a step-protocol introduced in the previous chapter (red line) we can indeed observe an increase in crystal population

and domain size for the fluctuating dipolar interaction strength.

In the following section we want to investigate the self-assembly of systems with a continuously increasing dipolar strength. Allowing the particles to slowly structure into strings with high mobility and merging into crystals could lead to larger domains of BCT.

Continuously Increasing Protocol

Here we want to analyse the crystal nucleation process of colloidal dipolar system with continuously increasing dipolar strength. Examples of those protocols are shown in Fig. 7.11 (c). These step like functions of μ are characterised by the duration of each step and the difference between them.

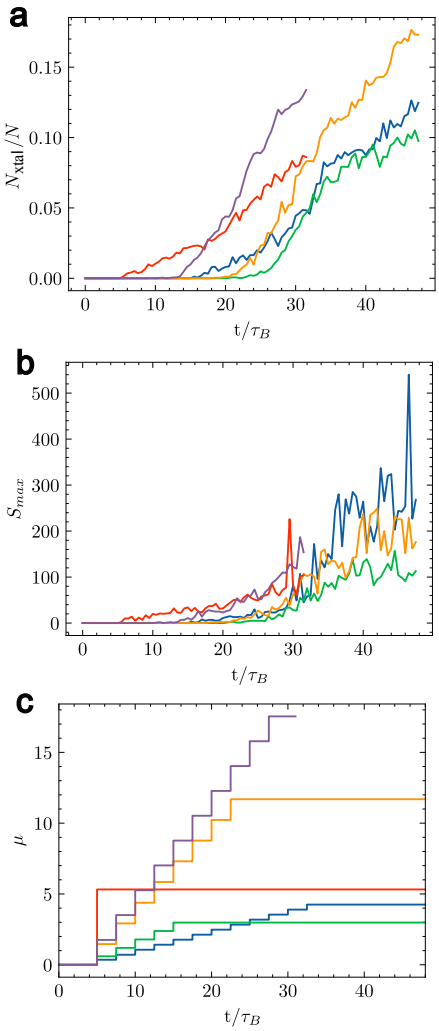

Figure 7.11: Crystallisation of system with continuously increasing dipolar strength. (a) Crystal population as a function of time for different protocols. (b) Evolution of the largest crystal nucleus in the system. (c) Continuous-Protocols for different step sizes in a system with $\phi = 0.48$.

Figure 7.11(a) and (b) show the evolution of crystal population in the system and the size of the

largest BCT nucleus as a function of time. Again nucleation processes with different characteristics can be obtained. Interestingly the slowest increase in the field strength produces the largest nucleus (blue line), even though the crystal population is smaller compared to protocols applying a higher electrical field. This again supports our assumption, that for high dipolar interaction strength a lot of clusters with ordered structure are formed, that can not merge. For the smaller interaction potential the particles are more mobile leading to the emergence of larger crystal domains with less defects. Compared to the optimum assembly for a step-protocol, the nucleation takes place at later times, but then with increased speed. Also, it looks like the step-protocol produces larger crystal domains compared to the simple approach introduces earlier. One could argue, that the nucleation time of the system with a continuous increase of the dipolar interaction should be rescaled with respect to the time the interaction potential crosses the phase boundaries and that could in fact lead to faster crystallisation. But here we are interested in the influence of reorganisation and structuring of the system before formation of crystal domains. Previous studies have shown, that the structure of the liquid changes with increasing field strengths, favouring higher-order structures that are compatible with BCT. This could lead to a lowering of the nucleation barrier and faster crystallisation. Therefore, rescaling the time is not appropriate here, as otherwise structural changes prior to crystal nucleation would be disregarded.

High-Low Protocol

We now want to analyse protocols in the dipolar interaction strength, that first apply a high field for a couple of Brownian times followed by a reduction leading to more mobility of the particles. With that the effect of particle organisation into strings prior crystallisation will be analysed. If the particles immediately form string-like structures that are compatible with the BCT crystal and are then able to move due to the instantaneous drop in field strength, merging of the individual strings could lead to an increase of large crystal domains. Figure 7.12 shows the applied protocols in μ and the observed crystal population and evolution of the largest crystal size in the system.

Compared to the simple step-protocol (red line) we observe a comparable increase in the overall crystallinity of the system and evolution of the size of the largest crystal domain. It seems like all the protocols produce similar crystallisation processes with small differences in the final structure of crystal nuclei. However it seems like a moderate increase to $\mu = 8$ followed by a big reduction of the dipolar interaction strength to $\mu = 2$ produces large crystal domains of more than 300 particles (green line). Here we want to emphasize again that experiments we are comparing can be a slightly

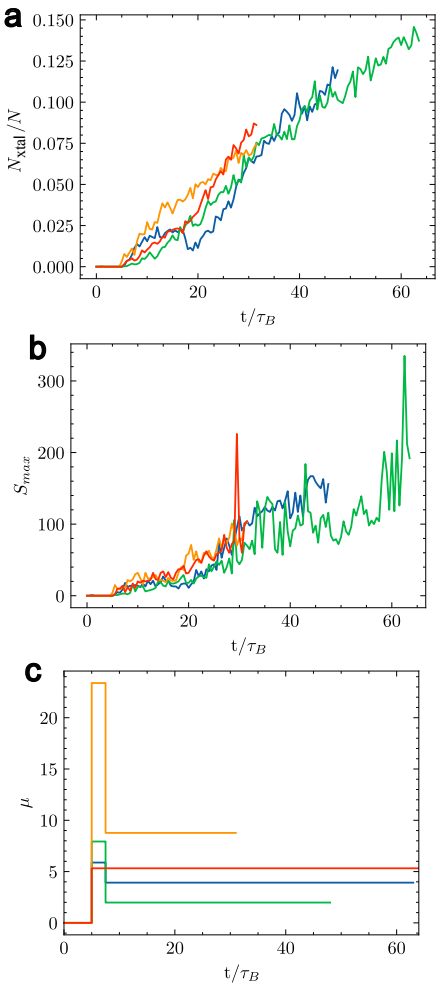

Figure 7.12: Crystallisation of system with varying dipolar strength. (a) Crystal population as a function of time for different protocols. (b) Evolution of the largest crystal nucleus in the system. (c) HL-Protocol for different μ_{min} and μ_{max} for a system with $\phi = 0.48$.

different state points in terms of the volume fraction. The earlier introduced mapping of ϕ between experiments and computer simulations comes with a random error due to small changes in the imaging properties and the binning of the state point. Small differences in the volume fraction come with slightly different phase boundaries for different experimental systems leading to a change in the dynamics of the nucleation process.

Nevertheless, in the next section we want to compare all the protocols introduced so far and find an optimum self-assembly path for dipolar colloidal systems.

7.2.2 Comparing Protocols

Here we want to summarize the analysis of crystal nucleation with different temporal functions of the dipolar interaction strength by comparing the optimum assembly of each protocol. Figure 7.13 shows the results for the best observed crystallisation of the simple step-protocol (red line), square-wall protocol (blue line), continuously increasing dipolar strength (green line) and high-to-low protocol (orange line).

Interestingly we find that all protocols in Fig. 7.13 (c) show similar values in μ close to the phase boundary between liquid and BCT for dipolar systems with volume fraction $\phi = 0.48$. This suggests, that crystal formation of large domains is optimised compared to other dipolar strength. Comparing the crystal population and evolution of the largest crystal size shown in Fig. 7.13 (a) and (b) shows that the fastest and most effective crystallisation occurs for a fluctuating protocol between moderate ($\mu = 3.25$) and high ($\mu = 6.5$) dipolar interaction strengths (blue line). For this protocol we observed a fast increase in crystallinity after a very short time and formation of a crystal domain of up to 500 particles. All other protocols only produce domains with 100-200 particles each. This could be explained by the optimisation in the balance between forcing the particles to form ordered string like structures and allowing the strings to reorganise into BCT domains without allowing the particles to become too mobile and thereby lose order.

To analyse the crystallisation precess from a particle-resolved persperctive, we now want to analyse the population of a higher-order cluster identified by the TCC. Fig. 7.14 shows the evolution of a selection of different TCC clusters consisting of 5 to 8 particles. First we again want to emphasize the system is in a hard sphere like configuration for the first 5 Brownian times, because no field is applied. The agreement for all measurements in this period indicates that the samples have very similar volume fractions.

Figure 7.14 (a) shows the evolution of the cluster 5A which consists of a 3-membered ring with two additional particles sitting on top and below. This cluster is not compatible with BCT order and therefore decreases for all the measurements as crystallisation sets in. Interestingly the decrease is only monotonous for the simple step-protocol (red line). With introducing the dipolar interaction the population of the 5A clusters drops and then stays constant even though the crystallinity in the system increases and the largest crystal domain is growing. For the fluctuating protocol the population of 5A also drops with applying of the field, but increases with every relaxation of the dipolar strength. The averaged population is comparable to the step-protocol. For the

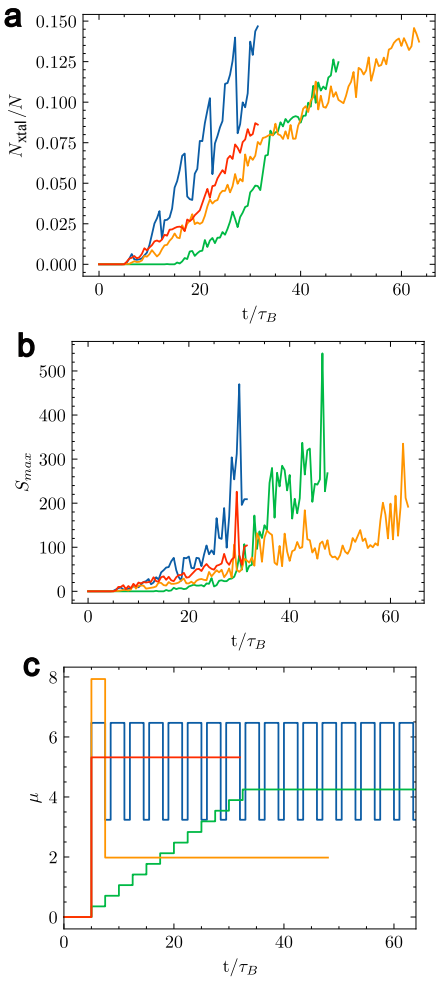

Figure 7.13: Optimisation of crystallisation with varying dipolar strength. (a) Crystal population as a function of time for different protocols. (b) Evolution of the largest crystal nucleus in the system. (c) Different protocol which maximise the crystallinity in the system.

high-to-low protocol first the population drops with increasing the field, but it increases again with the relaxation and then starts dropping again during applying a constant field due to formation of more crystal structures. Surprisingly for the protocol of continuously increasing dipole strength the population of 5A clusters first increases with increasing the field strength. It only starts dropping as soon the first crystal are formed in the system. A similar behaviour can be seen in the evolution of the 7A cluster (Fig. 7.14 (c)). This cluster is called the pentagonal bipyramid and it consists of a 5-membered ring with 2 particles sitting on top and below the ring. This cluster is often associated with inhibiting crystal nucleation, because it cannot be stacked to fill 3D space. In previous studies the occurrence was linked to slowing down of crystallisation [228]. In contrast to the 5A cluster the population of the 7A cluster vanishes for all of the protocols to the end of the measurements indicating fast crystallisation.

Figure 7.14 (b) and (d) show the evolution of the 6A and 8A clusters. Both are compatible with the

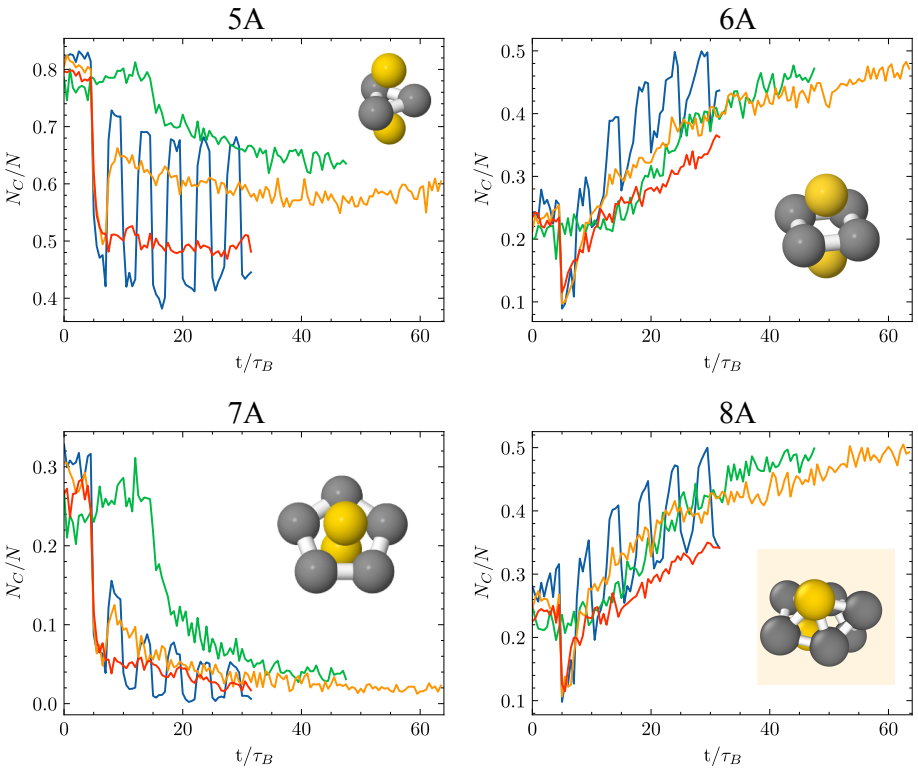

Figure 7.14: Analysis of the evolution of the system structure with population of TCC clusters. Each panel shows the evolution of the respective TCC cluster population during crystallisation. (a) 5A (b) 6A (c) 7A (d) 8A

BCT crystal and increase for all the protocols during the self-assembly process. Both figures look very similar and therefore we will only discuss the 6A cluster which consists of a 4-membered ring again with two particles sitting on top and below. Surprisingly only the continuos protocol shows a monotonous increase in the population of that cluster. For the other protocols the population of 6A drops with applying the electrical field and introducing the dipolar interaction. Then the population increases dramatically over the rest of the measurements. It is interesting that the step-protocol and the protocol of continuously increasing dipole strength (red and yellow lines) first show similar cluster populations due to the abrupt introduction of the dipolar interaction. Then the high-to-low protocol drops to a smaller value in μ allowing the structure to relax and regain fourfold symmetric structures and crystallise. We observed the most effective crystallisation with the fluctuating protocol (blue line). Even though the electrical field and accordingly the population of the BCT like cluster changes, a clear increase in four-fold symmetry compared to all the other protocols is present.

7.3 Conclusion

In summary, we have found a way to optimise nucleation in dipolar colloids. Different stages of nucleation are recognisable, characterised by the formation of string-like structures or small domains of BCT and the merging of different BCT nuclei. This can be seen by comparing the population of crystalline particles and the evolution of the maximum crystal domain in the system under investigation.

It becomes clear that crystallisation involves a compromise between high dipole moments, which lead to ordered structures and the nucleation of many BCT nuclei, and particle mobility, which allows defects to be annealed away and different domains to merge. It is important to balance phases of high mobility against the loss of order through melting, as can be seen from the fluctuating protocols with long periods of small dipole moments. We have found that there is an optimal range for the strength of the dipole moment near the phase boundary, independent of the form of the μ protocols. Nevertheless, a fluctuating field with small to moderate values produces large crystal domains most efficiently.

In addition, we analysed the structure of the systems using the TCC and saw that, as expected, the population of BCT-compatible structures in the sample increases with nucleation. Furthermore, although this is only speculative, it can be argued that ordering the system by continuously increasing the dipole moment promotes nucleation of large crystal domains. However, a more detailed investigation with more data would be necessary to make comprehensive statements.

Finally, it should be noted that the experimental data was binned to an average volume fraction. Here, again, more experiments in the future would be helpful to investigate the influence of small changes in the state point on the nucleation process.

Chapter 8

Active Colloids in Three Dimensions

The phase diagram shown and the synthesis protocol for the 3D systems of active colloidal particles were developed by the group of C. Patrick Royall. The author synthesised new Janus particles using a similar method and contributed to improving reproducibility by measuring the thickness of the applied metal layer thickness. The experiments to demonstrate activity were developed, performed, and analysed by the author.

Chapter 1.5 already introduced the concept of active matter. The term refers to a class of systems in which energy is consumed at the level of the constituent particles. At the microscopic level, energy is continuously injected into the system, which can lead to collective behaviour such as swarming, flocking, and spontaneous flows. These systems of self-propelled units exist far from equilibrium and, unlike passive systems in equilibrium with a heat bath, cannot be described by classical equilibrium statistical mechanics [60, 62, 63].

Examples of active matter can be found in a wide variety of systems, from biological examples such as bacterial colonies [64, 65], cell tissues [66, 67] or flocks of animals [68], to synthetic implementations in the form of robotic swarms [229, 230], vibrated grains [231] or colloidal systems [57–60]. The latter occupy a special position in the landscape of systems to be investigated because they are particularly versatile and also controllable [57]. Interactions between the individual micrometre-sized particles can be modified at will [78] and modelled in computer simulations [232]. Furthermore, unlike other synthetic active matter systems, colloidal particles can be produced and studied in large quantities.

Such large-scale systems are ideal for investigating phase behaviour or other collective phenomena.

The phase behaviour of passive colloids has been examined in detail in the previous chapters, and it has become clear that these systems can self-assemble into a wide variety of crystalline structures [15, 16, 44, 78]. A major open question therefore concerns the complex phase behaviour that results from a combination of colloidal self-assembly and activity [62, 69]. In previous studies, interesting phenomena in active colloids have already been observed using mainly computer simulations, such as living crystals [233] or mobility-induced phase separation [234, 235]. Interestingly, previous experimental work was mainly limited to quasi-2D systems.

Here we want to explain in detail the synthesis of a 3D model system consisting of active colloids and describe its phase behaviour. The Janus particles are self-propelled by induced-charge electrophoresis [103, 236–238]. Dielectric particles-one hemisphere of which is coated with a thin metal layer-are placed in an alternating electric field and therefore exhibit activity in the plane perpendicular to the direction of the external field. In addition, dipole-dipole interactions are induced, similar to the model systems discussed in the previous chapters. The particles exhibit anisotropic interactions and attract each other when aligned with the field and repel each other when perpendicular to it. The dipole strength and activity of the particles can be tuned by the strength and frequency of the electric field [48, 107].

The system has already been extensively studied in 2D, but previous publications have shown that the 3D system offers a variety of more exotic phases, ranging from travelling strings to dynamic labyrinths and active crystals [237, 239–244].

In the following, the 3D model system is described in more detail, explaining the rich phase behaviour by summarising previous work [105, 106, 245]. Then, a new protocol for sample preparation improved by the author is discussed. This includes all the technical steps, from the synthesis of monolayers with high area fraction, to the coating of dielectric particles with a thin metal layer, to solvent composition. For the first time, we were able to precisely measure the thickness of the deposited metal layer, which determines the activity of the sample. This represents a major step forward in the comparability and reproducibility of these experiments. At the end, an example data set showing activity in the sample is presented. We were able to measure the propulsion speed and persistence length of the active particles. In addition, we are currently working on systems with high volume fractions to analyse the connection between structural properties and the nucleation mechanism in more detail.

8.1 Experimental System

The system under investigation consists of self-produced Janus particles, the synthesis of which will be described in detail later in this chapter. The colloids are self-propelled by induced-charge electrophoresis and exhibit activity in the plane perpendicular to the electric field [103, 236–238]. The activity can be adjusted as desired via the field strength. In addition, the particles interact via a dipole-dipole interaction due to the alternating external field, comparable to the passive systems that were part of the previous chapters [48, 107].

In the work of Sakai and Royall [105], silica particles with a diameter of $\sigma = 1.5$ μm were used, which were labelled with rhodamine dye to make them visible by confocal microscopy. One hemisphere of the silica spheres is covered with a 3 nm-thick layer of chromium. A thicker layer means more activity, but for the imaging process, it must be ensured that the particles remain transparent. This limits the maximum layer thickness of the metal. A 15 nm silica layer is then deposited on top of the metal [246].

The particles are dispersed in a mixture of milliQ water and DMSO with a volume ratio of 7:10. The solvent and particles are refractive-index matched, but not density-matched. In samples with a high volume fraction, sedimentation can be neglected because the effect is compensated by the activity and crowding effects.

In dilute systems with a low volume fraction, the approximation is not valid [106] and, in contrast to previous studies, a different model system was used. It consists of polystyrene particles with a diameter of $\sigma = 1$ μm, also stained with rhodamine. Here, 5 nm of aluminium is deposited to one hemisphere of the particles, followed by 5 nm of silica. The solvent is produced with a volume ratio of 1:1, which allows the density to be matched. However, this comes at the expense of refractive index matching, which is why the imaging properties are significantly worse and particles cannot be tracked reliably.

The samples for medium and large volume fractions, consisting of silica spheres, and the samples for small volume fractions ($\phi < 0.05$), polystyrene particles, are loaded into a sample cell consisting of two ITO-coated cover slips. The cell design is similar to the samples used for the investigation of passive dipolar colloids [78]. A more detailed image of the capillary is shown in Fig. 7.3, but in this case, smaller spacer particles are used and the sample has dimensions of approximately 40 μm in the direction of the electric field. The two cover slips are connected to a signal generator and an alternating field with a frequency of 5 kHz is applied. The strength of the electric field can be

adjusted to change the strength of the dipole interactions of the particles.

Three-dimensional images of the samples were then captured using a Leica TCS SP8 confocal microscope. From the microscopy images, particle positions can be extracted [247] and the particle-resolved data used to analyse the structure of the sample. Based on these images, it was possible to produce a detailed phase diagram of the active 3D systems [105].

8.2 Phase Behaviour of Active Colloids in 3D

The phase behaviour was already introduced in detail in Chapter 1.5.4. Here we would just like to give a brief reminder. The phase behaviour is determined by the interplay of activity, volume fraction, and dipolar interactions, leading to regimes where one of these factors dominates.

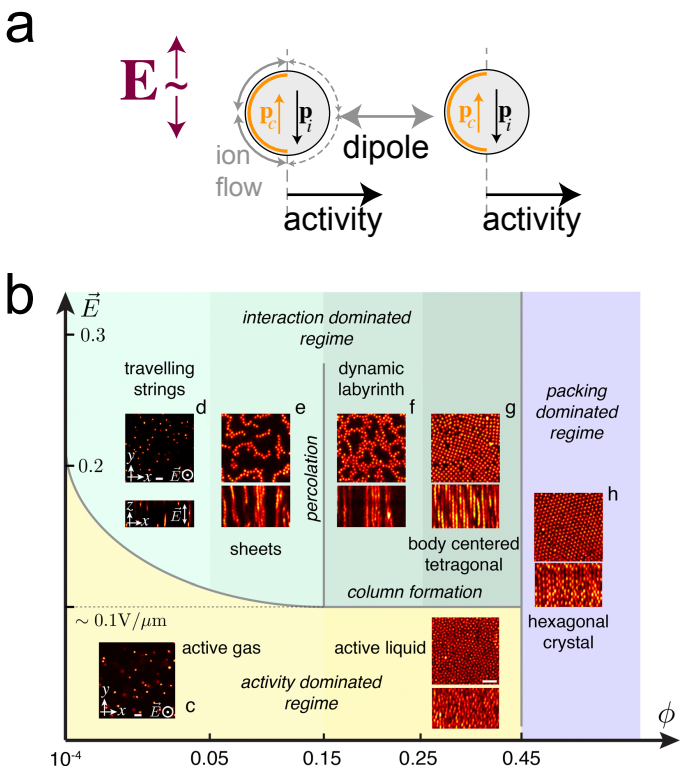

Figure 8.1: Phase diagram of active particles in 3D (a) The alternating electric field $\vec{E}$ induces activity and dipole-dipole interactions between the particles in different directions. (b) The phase diagram shows different regimes (c–h) dominated by activity, dipolar strength, or volume fraction, leading to the self-assembly of a variety of different structures and crystal polymorphs [245]. Reproduced from [105].

At low volume fractions and weak dipole strength, the systems form a 3D "active gas" (Fig. 8.1(c)), with particle motion active in the xy-plane and diffusive along z. Increasing the volume fraction at low field strength produces an active liquid, where dynamics remain dominated by activity.

With stronger fields, particles align into parallel strings (8.1(d)), which span the capillary height and move collectively in the plane. These structures travel more slowly than individual particles due to force compensation and possibly wall-induced hydrodynamics. At slightly higher volume fractions ($\phi \approx 0.01$), strings merge into sheets, which at $\phi \approx 0.15$ further assemble into a dynamic, labyrinth-like network (8.1(e)) that continuously reorganises. Although inherently three-dimensional, these structures are quasi-2D, with anisotropy set by the field direction. In this regime, dipolar interactions dominate the structures.

At still higher packing fractions, structural order becomes favourable. Around $\phi \approx 0.3$ and strong dipolar interactions, the system nucleates into body-centred tetragonal crystals, as also observed in passive systems. At $\phi \approx 0.45$, FCC and HCP crystals with hexagonal symmetry form, again consistent with passive behaviour [48, 107].

8.3 Janus Particle Synthesis and Sample Preparation

In the following, we will describe how the Janus particles and the test cell itself are manufactured. The following work was carried out by the author in order to produce systems similar to those just introduced. The synthesis of Janus particles and the verification of their activity will be demonstrated in detail here.

First, we describe how monolayers of silica particles can be produced before the coating. This is followed by a description of the deposition method and how the thickness of the deposited layers can be measured. Finally, we present an example measurement demonstrating the activity of the self-produced Janus particles.

8.3.1 Monolayer and Coating

For the synthesis of Janus particles, we follow protocols from previous work investigating similar systems [105, 238, 245]. The silica spheres (Ksiker Biotech) with a diameter of 1.5 μm are labelled with a dye (excitation: 485 nm and emission: 510 nm) so that they can be imaged with the confocal microscope. The aim of the synthesis is to produce Janus particles consisting of dielectric silica spheres, one hemisphere of which is coated as evenly as possible with a thin metal layer, in our case chromium, followed by a layer of silica.

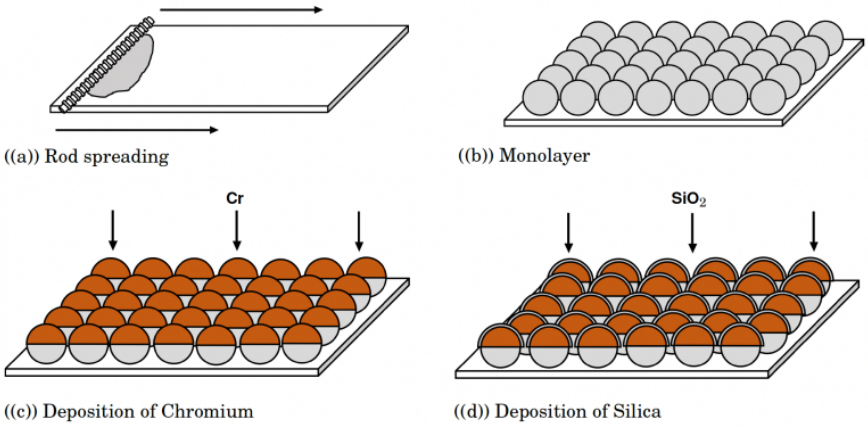

Figure 8.2: Schematic representation of synthesis steps for Janus particles. One hemisphere of dielectric particles gets covered by thin metal layer. (a) Produce Monolayer of Particles with a rod spreader. (b) Monolayer of silica particles before deposition. (c) Monolayer after Chromium depositions. (d) Monolayer after silica deposition. Reproduced from [104]

The first step is to produce monolayers of the uncoated raw particles. The aim here is to achieve the highest possible area fraction without the particles overlapping or forming aggregates, which could lead to heterogeneous coating of the base layer. As described in [104], the particles, which are delivered dispersed in an aqueous solution, are transferred to propan-1-ol. The lower surface tension of the solvent prevents effects such as coffee ring formation, in which regions with a high volume of sample form on the glass surface, where the particles aggregate in 3D structures and destroy the perfect monolayer. By weighing, a sample with a volume fraction of approximately $\phi = 0.07$ is prepared, and 20 μL is dispensed on a microscope slide. We use a rod spreader to distribute the sample droplet evenly over the entire surface and produce a homogeneous monolayer. This step is visualised in Fig. 8.2(a). The monolayer can be imaged using bright-field (Fig. 8.3(a)) and confocal microscopy (Fig. 8.3(b)) to ensure that there is indeed only a single layer on the glass surface. If the volume fraction of the sample is too high, it can be further diluted until a perfect monolayer is achieved. On the other hand, we want to have the highest possible area fraction in order to be able to coat as many particles as possible in a single deposition run. It is also important that the glass slides are thoroughly cleaned before use. To do this, they are sonicated in milliQ water, rinsed with propan-1-ol and then dried. Dust and other imperfections can lead to heterogeneous nucleation and instability of the sample later on.

Now the particles are ready for coating, in our case using a sputtering machine with plasma deposition. This involves generating a plasma between the target, in our case metal (chromium) and silica, and the substrate (monolayer of silica particles). Positive ions are accelerated towards the

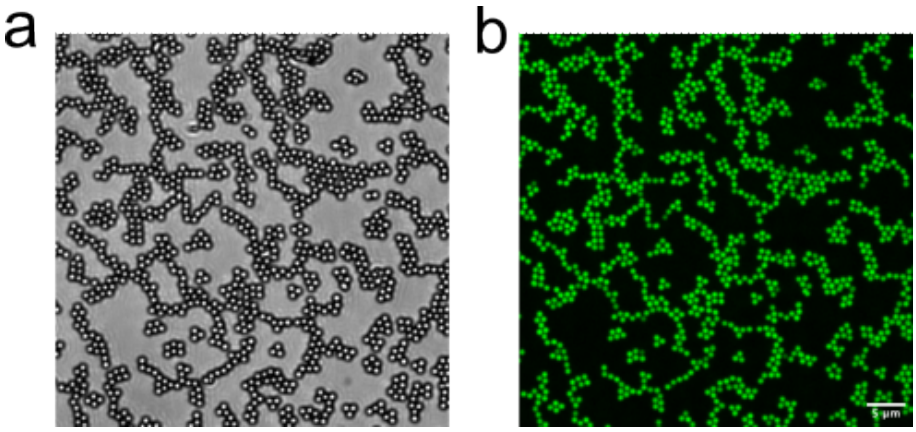

Figure 8.3: Monolayer of silica particles, imaged with bright field microscopy (a) and fluorescent confocal microscopy (b).

target, which releases atoms that travel through the vacuum forming a thin film on the monolayer. The thickness of the applied layer could be determined from previous coating processes. In our case, a chromium layer of approximately 3 nm and a silica layer of 15 nm were to be deposited.

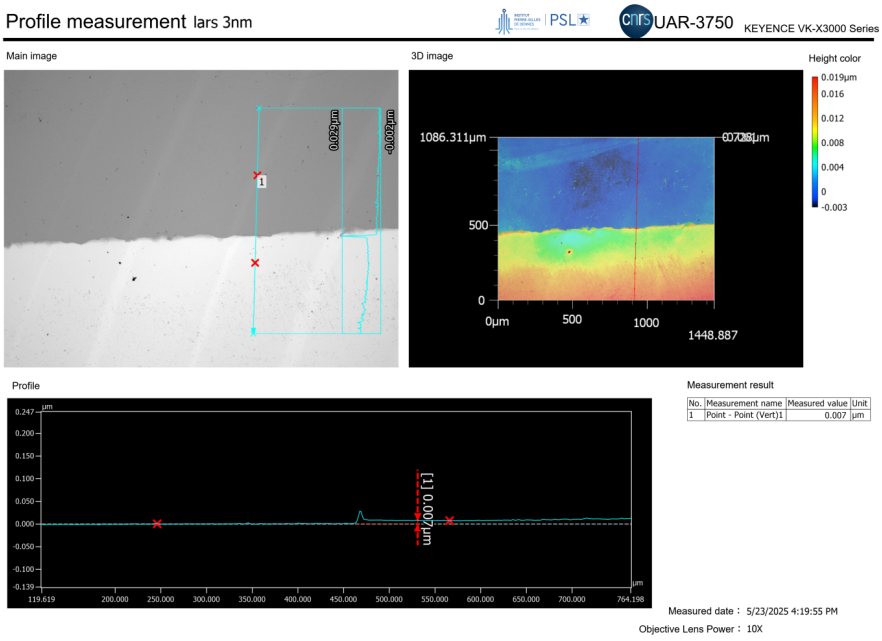

Figure 8.4: Result of the measurement with the profilometer. The thickness of the applied metal layer is approximately 7 nm. The sample on which the measurement was performed was produced using a microscope slide covered halfway with adhesive tape, which was coated with metal in a vacuum chamber together with the silica particles. After removing the adhesive tape, the height between the treated and untreated areas on the microscope slide can be measured.

To obtain an estimate of the layer thickness, we coated a control glass slide, half of which was covered with adhesive tape. After removing the adhesive tape, a profilometer (Keyence VK-X3000) was used to determine the height difference between the coated and uncoated regions on the glass slide. Figure 8.4 shows the result of the measurement, which determined a layer thickness of 7 nm

for chromium. A thick metal layer reduces the signal strength that can be recorded by the confocal microscope, which makes it difficult to track the particle positions. On the other hand, a thin chromium layer could show patchy patterns, which prevents the Janus particles from being active.

8.3.2 Solvent and Sample Cell

In the next step, the coated monolayers are carefully washed with propan-1-ol and then separated from the glass surface by sonication in ethanol for 30 minutes. The sample was then sonicated for another 60 minutes to dissolve particle aggregates. One problem we encountered during the synthesis protocol was that the silica particles stuck to the glass slide after sputtering. Figure 8.5 shows a monolayer with some particles remaining after the sonication step. With extended sonication time and mechanical action, the proportion of detached particles could be increased.

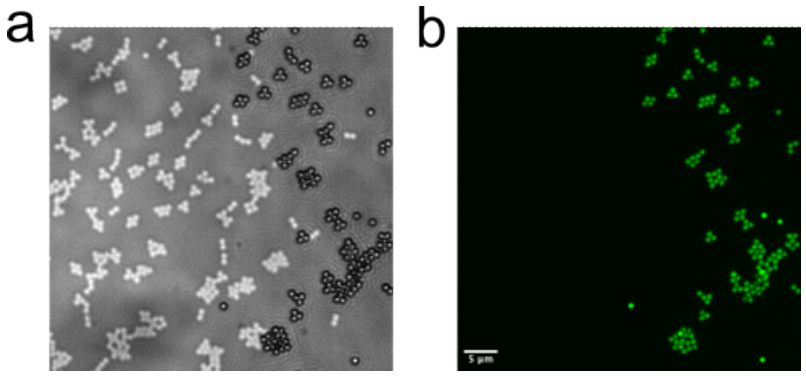

Figure 8.5: Monolayer of coated silica particles on the microscopy slide after sonication. (a) Bright-field microscopic images shows particles still stuck to the glass surface on the right and bright regions where no metal was deposited, corresponding to where particles were located before sonication on the left. (b) Confocal microscope image shows particles that are still stuck on the glass surface.

As described above, the Janus particles are to be analysed in 3D using confocal microscopy in order to draw conclusions about the structure of the system from the particle-resolved data. For this purpose, the particles and solvent must be index matched. We use a mixture of milliQ water and DMSO with a volume ratio of 7:10. The sample is then placed in a self-build capillary consisting of two parallel ITO-coated cover slips. The setup is identical to the sample cells we used for the analysis of dipolar colloids.

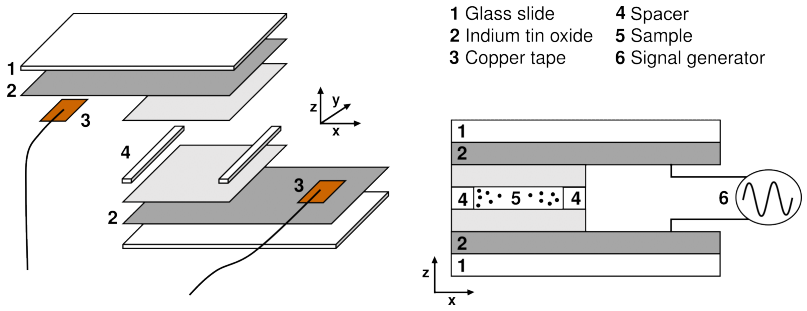

Figure 8.6: Schematic representation of the sample structure. Particles are loaded to a self-build capillary consisting of two ITO-coated cover slips, connected to a signal generator to introduce an AC electric field in the sample.

8.3.3 Active Janus Particles

Once the Janus particles have been synthesised and dispersed in the correct solvent, they can be made active in the self-built capillary under the influence of the electric field and imaged using confocal microscopy. In the following, we demonstrate that the synthesised particles are indeed self-propelled. Therefore, the passive and active parts of a particle's trajectory are examined separately by calculating the MSD. In addition, the propulsion velocity and persistence length of the active particles were determined.

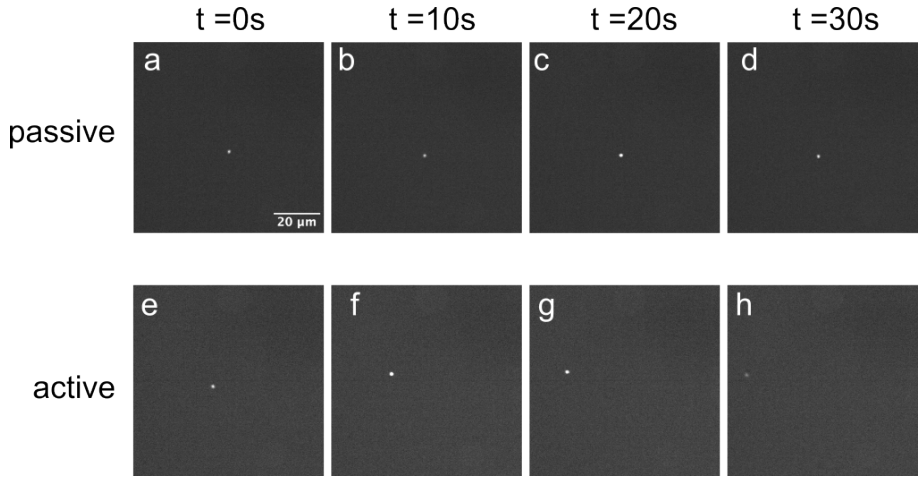

Figure 8.7: Image sequence of example measurements of passive and active particles. (a-d) No field was applied and the particles undergo pure Brownian motion. (e-h) External field applied and particles are self-propelled. For (h) the particles moves out of the focal plane due to activity.

Figure 8.7 shows the image sequence of an example experiment to illustrate the activity of the Janus particles. We created a very dilute sample in which the particles sediment to the bottom of the capillary because they are not density-matched with the solvent. Confocal images of the quasi-2D system were taken with a frame duration of 1 s. A total of 64 images were captured. Figure 8.7(a-d) show the particle image without an external field. Only small fluctuations in the

position can be observed. For Fig. 8.7(e-h) the alternating field was applied and the particle the particle became self-propelled. Due to rotational diffusion the particle moves out of the focal plane by the end of the measurement (Fig. 8.7(h)).

Using the Python package "Trackpy", the coordinates of the particle could be determined in each frame and linked into trajectories. At the beginning of the measurement, no external field was induced, and the diffusive nature of the passive Janus particle's movement can be seen from the red line in Fig. 8.8(a). Points represent the position of the particle in each frame. The inset shows a zoomed-in view of the movement without an alternating electric field. After 32 frames, the electric field was switched on at a frequency of 5 kHz, and the Janus particle immediately showed activity in the xy-plane (blue part of the trajectory). This sample measurement shows that the self-produced samples indeed show activity at the particle level and that our synthesis was successful.

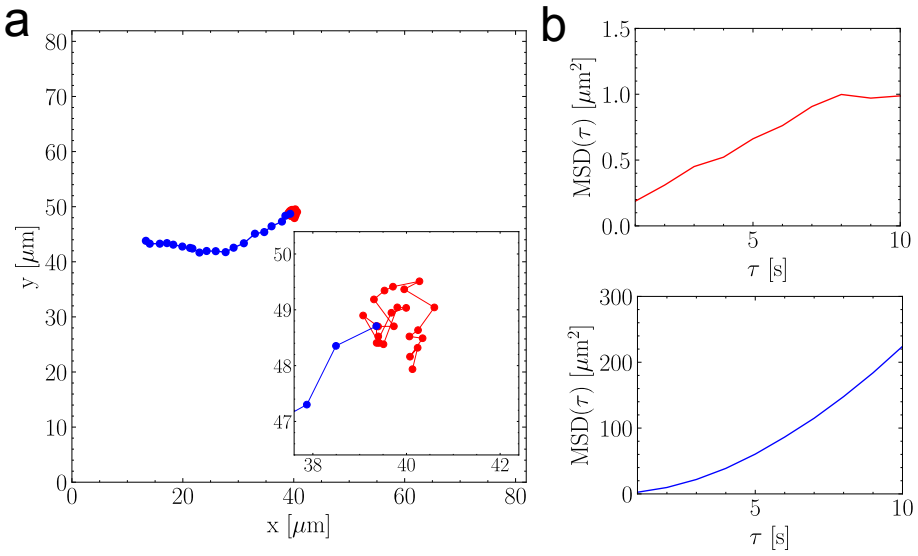

Figure 8.8: Trajectory of passive and active Janus particle. (a) Red line shows the trajectory without the external electric field. The particle shows pure diffusive motion. Once the electric field is applied, the particle is self-propelled (blue line). The inset shows a zoomed-in picture of the diffusive motion. (b) MSD calculated for the passive (red) and active (blue) motion separately.

From the single particle trajectory we were able to characterise the different forms of motion. From the single particle trajectory data, we were able to analyse the two regimes of motion separately. Figure 8.8(b) shows the MSDs for passive (top) and active (bottom) motion. The quantitative difference is clearly visible. We also compared the average velocity of the particles. For passive motion, we found $v_p = 0.38$ μm/s and for active motion $v_a = 1.52$ μm/s. Finally, we looked at rotational diffusion and found that, as expected, the orientation of the particle is completely decorrelated in the passive case. For the active trajectory with electric field, we were able to determine a persistence length of $l_p = v_a/D_r = 43.7$ μm. We determined the rotational diffusion

coefficient by fitting an exponential function to the orientation autocorrelation function.

8.4 Conclusion

In this chapter, we have presented an example system for colloidal active matter. In contrast to many previous studies, which mainly investigate quasi-2D systems, this is a 3D system in which Janus particles, self-propelled by induced-charge electrophoresis, exhibit activity in the plane perpendicular to the direction of the AC electric field. We have provided an overview of the phase behaviour of such systems based on the results of previous studies [105] and described the experimental setup in detail.

We were able to realise the experimental system and successfully produced self-propelled Janus particles. In contrast to previous studies, we were able to precisely determine the thickness of the deposited layer, thereby ensuring a homogeneous coverage of the hemisphere. In the past, the reproducibility of experiments was limited because the activity of the samples varied greatly between different manufacturing cycles. By quantifying the layer thickness, experiments can be compared with a previously unattainable level of precision. Then we showed that the produced particles actually exhibit activity in the appropriate solvent and capillaries. We have carried out an example measurement that clearly shows the transition between passive and active movement of the particles when an electric field is applied. From this measurement, we were able to calculate single-particle MSDs and the persistence length of the active particle.

In conclusion, we provide a solid foundation for further investigations of this interesting model system, such as the underlying mechanisms of the known phase transitions and the structure of the liquid phase in detail.

Chapter 9

Conclusions

The overall aim of this work was to gain a better understanding of the underlying mechanisms of nucleation and crystallisation in colloidal model systems. Using confocal microscopy, we are able to produce particle-resolved data and reveal otherwise hidden structural changes associated with the phase transitions of the systems under investigation. This thesis was motivated by the lack of ability to reliably and quantitatively predict nucleation in various systems, from atomic to molecular to colloidal, which is particularly evident in the so-called hard sphere nucleation discrepancy, where nucleation rates from experiments vary by more than 10 orders of magnitude from predictions from computer simulations.

First, the role of colloidal systems in the world of soft matter physics was described and the simplest and most studied system of hard spheres was introduced. In particular, the realisation of colloidal hard spheres in experiments and the interaction potentials of real particles, characterised by a certain degree of softness, were discussed. This was followed by a description of the equilibrium phase behaviour and the influence of polydispersity on the phase diagram. Subsequently, the nature of the dipolar interactions induced by an external alternating electric field was described in detail, as was the resulting phase behaviour, which is characterised by a variety of crystal structures, namely face-centred cubic (FCC), hexagonal close-packed (HCP), body-centred cubic (BCC), body-centred tetragonal (BCT) and body-centred orthorhombic (BCO). Then, the model system of active colloids, which exhibit a similar dipolar interaction to passive particles but are active in the plane perpendicular to the electric field, was introduced. Following the description of active Brownian motion, the phase diagram was explained, which shows various exotic structures, such as a stable, continuously changing labyrinth or travelling strings. Finally, nucleation, i.e. the formation of an

ordered solid from a disordered phase, was introduced, and classical nucleation theory was explained as a model for describing this process. In this context, heterogeneous nucleation and Ostwald's rule of stages were also explained, and it was described how nucleation rates can be measured in light scattering experiments.

The following chapter described the methods used, with special focus on sample preparation and imaging techniques. We explained how density and refractive index matched samples with specific volume fractions can be produced and which capillaries were used to obtain the best possible images with the confocal microscope. The working principle of confocal microscopy was explained in detail before the different approaches of laser scanning and spinning disk confocal microscopy were described in terms of their advantages and disadvantages. Laser scanning was used to examine hard spheres and dipolar particles, which require images of the highest quality to enable reliable particle tracking, i.e. the determination of particle coordinates based on the intensity distribution in the 3D confocal images. For the macroscopic sedimenting samples, on the other hand, the faster image acquisition of the spinning disk confocal microscope was advantageous for capturing confocal microscope multiscale images, i.e. stitched macroscopic images from individual images with microscopic resolution, in a short time. This was followed by a description of common computer simulation methods, such as molecular dynamics simulations (MD), event-driven molecular dynamics simulations (EDMD), and the Monte Carlo method (MC), with a focus on which approaches are best suited for what kind of systems and how nucleation processes can be studied using rare-event sampling. Finally, various observables were introduced that describe the structure of the systems under investigation. In addition to the radial distribution function, i.e. pair correlations, which in principle are also accessible for light scattering experiments, the higher-order correlations accessible from particle-resolved data were explained. To identify higher-order structures, the topological cluster classification algorithm (TCC) was described, which uses Voronoi tessellation and the determination of shortest path networks to identify particle clusters. As it turns out, these minimum-energy clusters play a key role in nucleation processes. At this point, the bond-orientational order parameter, used to detect solid-like structures, was also introduced, which was used to determine crystalline environments and identify pre-critical nuclei.

After a detailed introduction and description of the methods, the results of this thesis were presented in the following chapters. First, the newly developed deep learning routine "Colloidoscope" was presented, which is based on a 3D residual U-net, trained on simulated data configurations convolved with realistic point spread functions and noise to mimic the experimental conditions. It was shown that, compared to conventional methods, in this case, compared to "Trackpy", "Colloidoscope"

tracks more particles with higher localisation accuracy, especially for dense systems with a low signal-to-noise ratio, while avoiding false positive identifications. The output of "Colloidoscope" was validated using simulated data, experimental measurements and the analysis of higher-order structures, demonstrating that this approach produces high-quality particle coordinates with fewer parameter adjustments, enabling more reliable investigation of structural changes in colloidal systems.

In chapters 4 and 5, we revisited the long-standing hard sphere nucleation discrepancy, which can be seen between predictions from computer simulations and light scattering experiments and spans over more than ten orders of magnitude. First, by comparing the radial distribution function and the population of higher-order structures, we mapped the state point of the experiments onto the large-scale computer simulations with unprecedented precision. We then found good agreement between the free energy of formation of pre-critical nuclei between experiments and computer simulations, which leads to the disappearance of the discrepancy. This demonstrates that particle-resolved studies provide a reliable framework for investigating nucleation. Future work with smaller particles or advanced imaging techniques may allow us to probe the discrepancy regime in even greater detail. After we could not find any evidence of the discrepancy from the particle-resolved data, the origin of the discrepancy was investigated. To this end, the determination of the effective volume fraction in the light scattering experiments, which is based on the Paulin-Ackerson method, was investigated. We reproduced the Paulin–Ackerson experiments with confocal microscopy and showed that large crystal nuclei form in the sedimenting liquid on the same timescale as the crystal sediment. By analysing multiscale images with a deep learning routine, we measured the crystal fraction in the liquid, calculated the resulting bias in the effective volume fraction, and found it to be close to the bias needed to compensate the nucleation rate discrepancy. Further measurements at different state points, along with more robust image analysis, will be important to confirm this effect and test its generality.

We then turned our attention to dipolar colloids. We were able to directly capture Ostwald's rule of stages in a colloidal model system with particle-resolved data. In our central measurement, we observe a heterogeneously nucleated HCP crystal, which subsequently melts and is replaced by a thermodynamically stable BCT crystal. The melting process can be explained by the simultaneous nucleation of the BCT nucleus elsewhere in the sample and the accompanying drop in fluid volume fraction, which destabilises the HCP crystal. Analysis of the equation of state suggests that there is a volume fraction regime in which BCT grows while HCP is unstable. Further investigation of this regime using computer simulations would be helpful in explaining the phenomenon in more detail

and supporting our hypothesis. Furthermore, we investigated the structure of the fluid directly surrounding the crystal nuclei and found that, with increased dipolar strength, clusters are favoured, which are compatible with the BCT crystal. Particle-resolved volume fractions further showed that stable BCT crystals are surrounded by denser and more uniform fluids than metastable HCP nuclei. Further experiments with different volume fractions, which examine the fluid environments of HCP and BCT nuclei more closely, would be desirable. There may be structural configurations in the fluid that can be associated with the polymorph selection in the system.

We also looked at optimising crystallisation in dipolar systems by tuning the time dependence of the dipolar interaction strength. First, we mapped the volume fraction and dipolar interaction between experiments and computer simulations by comparing radial distribution functions, population of higher-order clusters, and the string fluid order parameter. We assessed the quality of crystallisation based on the population of crystalline particles, the size of the largest crystal nuclei and the total number of crystal nuclei in the system. Across all protocols, we identified an optimal range of the dipole interaction strength near the liquid–BCT phase boundary. In particular, fluctuating fields between moderate and high values produced the largest and most defect-free crystal domains, highlighting the trade-off between order and mobility. Analysis with the TCC confirmed an increase in BCT-compatible structures during assembly and showed that the protocol shape strongly affects the evolution of local order. At the moment, the protocols are being reproduced using computer simulations to substantiate the experimental results. Further steps would include investigating additional protocols and quantifying the effects of ordering and mobility to reliably predict the quality of crystallisation.

Finally, we investigated the known phase behaviour of the three-dimensional active colloidal model system based on Janus particles driven by induced-charge electrophoresis, described the synthesis of the Janus particles in detail, and demonstrated their activity in specially designed sample cells. A key advance is the precise measurement of the deposited metal layer thickness, which ensures reproducibility across samples and allows the degree of activity to be controlled. We verified that the synthesised particles are self-propelled, showing clear transitions between passive Brownian motion and active motion under an external electric field. From a single-particle trajectory, we extracted the propulsion velocity, MSD, and persistence length.

While this thesis offers new insights into the underlying processes of nucleation, Ostwald's rule of stages, polymorphic selection and active matter, it also opens several promising directions for future research. Extensive studies of crystal nucleation, perhaps even time-resolved ones, in

sedimenting samples using computer simulations and experiments could provide further insights into the crystallisation process and sedimentation of crystal nuclei. Investigations of dipolar systems have also raised open questions. A detailed analysis of the relationship between the structure of the liquid and the formation of different polymorphs may provide further insights into the mechanisms of nucleation. The optimisation experiments were carried out at relatively high dipolar interaction strengths, which led to the instantaneous formation of strings that subsequently assembled into BCT crystals. Due to the symmetry breaking caused by the direction of the electric field, this process can be regarded as a quasi-2D transition. It can be assumed that homogeneous nucleation of the BCT crystal can be observed at lower interaction strengths. Experiments in this regime could provide insights into the role of precursors in BCT nucleation. Finally, the establishment of reproducible 3D active Janus particles provides a powerful experimental platform for probing non-equilibrium phase transitions, collective dynamics, and the role of activity in nucleation. Currently, the particles exhibit activity in a plane perpendicular to the electric field. It is tempting to consider an experimental realisation of 3D systems of Janus particles exhibiting activity in all dimensions. The development of a new sample cell that allows two electric fields perpendicular to each other to be induced simultaneously would be a possible step in this direction.

Bibliography

[1] G. C. Sosso et al. “Crystal Nucleation in Liquids: Open Questions and Future Challenges in Molecular Dynamics Simulations”. In: *Chemical Reviews* 116 (2016), pp. 7078–7116.

[2] H. Lee and J. Romero. “Climate Change 2023 Synthesis Report IPCC, 2023: Sections. In: Climate Change 2023: Synthesis Report. Contribution of Working Groups I, II and III to the Sixth Assessment Report of the Intergovernmental Panel on Climate Change”. In: *Phys. Rev. Lett.* (2023), pp. 35–115.

[3] R. P. Sear. “Nucleation: Theory and Applications to Protein Solutions and Colloidal Suspensions”. In: *J. Phys.: Condens. Matter* 19 (2007), p. 033101.

[4] “XIII. The supposed effect of boiling upon water, in disposing it to freeze more readily, ascertained by experiments. By Joseph Black, M.D. Professor of Chemistry at Edinburgh, in a letter to Sir John Pringle, Bart. F. R. S”. In: *Philosophical Transactions of the Royal Society of London* 65 (Dec. 1775), pp. 124–128.

[5] J. C. Fisher, J. H. Hollomon, and D. Turnbull. “Rate of Nucleation of Solid Particles in a Subcooled Liquid”. In: *Science* 109.2825 (Feb. 1949), pp. 168–169.

[6] Katarina E. Blow, David Quigley, and Gabriele C. Sosso. “The seven deadly sins: When computing crystal nucleation rates, the devil is in the details”. In: *The Journal of Chemical Physics* 155.4 (July 2021), p. 040901.

[7] A. J. Amaya and B. E. Wyslouzil. “Ice nucleation rates near 225K”. In: *Journal of Chemical Physics* 148 (2018), p. 084501.

[8] D. A. Knopf and P. A. Alpert. “Atmospheric ice nucleation”. In: *Nature Rev. Phys.* 5 (1986), pp. 203–207.

[9] H. Niu, Y. I. Yang, and M. Parrinello. “Temperature dependence of homogeneous nucleation in ice”. In: *Physical Review Letters* 122 (2019), p. 245501.

[10] Jorge R Espinosa et al. “Seeding Approach to Crystal Nucleation”. In: *J. Chem. Phys.* 144.3 (2016), p. 034501.

[11] A. Haji-Akbari and P. Debenedetti. “Direct calculation of ice homogeneous nucleation rate for a molecular model of water”. In: 112 (2015), pp. 10582–10588.

[12] Jörg Behler. “Perspective: Machine learning potentials for atomistic simulations”. In: *The Journal of chemical physics* 145.17 (2016). Publisher: AIP Publishing.

[13] V.L. Deringer, M.L. Caro, and G. Csányi. “Machine learning interatomic potentials as emerging tools for materials science”. In: *Advanced Materials* 31 (2019), p. 1902765.

[14] Albert P Bartók et al. “Machine learning unifies the modeling of materials and molecules”. In: *Science advances* 3.12 (2017). Publisher: American Association for the Advancement of Science, e1701816.

[15] R. Evans, D. Frenkel, and M. Dijkstra M. “From Simple Liquids to Colloids and Soft Matter”. In: *Physics Today* 72 (2019), p. 38.

[16] C. P. Royall et al. “Colloidal Hard Spheres: Triumphs, Challenges and Mysteries”. In: *Rev. Mod. Phys.* 96 (2024), p. 040450034501.

[17] U. Gasser. “Crystallization in Three- and Two-Dimensional Colloidal Suspensions”. In: *J. Phys.: Condens. Matter* 21 (2009), p. 203101.

[18] U. Gasser. “Real-Space Imaging of Nucleation and Growth in Colloidal Crystallization”. In: *Science* 292.5515 (Apr. 2001), pp. 258–262.

[19] JR Savage and AD Dinsmore. “Experimental Evidence for Two-Step Nucleation in Colloidal Crystallization”. In: *Phys. Rev. Lett.* 102.19 (2009), p. 198302.

[20] Stefan Auer and Daan Frenkel. “Quantitative Prediction of Crystal-Nucleation Rates for Spherical Colloids: A Computational Approach”. In: *Annual review of physical chemistry* 55 (2004), pp. 333–361.

[21] Thomas Palberg. “Crystallization Kinetics of Colloidal Model Suspensions: Recent Achievements and New Perspectives”. In: *J. Phys.: Condens. Matter* 26.33 (Aug. 2014), p. 333101.

[22] L. Filion et al. “Crystal Nucleation of Hard Spheres Using Molecular Dynamics, Umbrella Sampling, and Forward Flux Sampling: A Comparison of Simulation Techniques”. In: *J. Chem. Phys.* 133 (2010), p. 244115.

[23] W. C. K. Poon, E. R. Weeks, and C. P. Royall. “On Measuring Colloidal Volume Fractions”. In: *Soft Matter* 8 (2012), pp. 21–30.

[24] C. P. Royall, W. C. K. Poon, and E. R. Weeks. “In Search of Colloidal Hard Spheres”. In: *Soft Matter* 9 (2013), pp. 17–27.

[25] Michio Tateno et al. “Influence of Hydrodynamic Interactions on Colloidal Crystallization”. In: *Phys. Rev. Lett.* 123.25 (Dec. 2019), p. 258002.

[26] Jorge R Espinosa et al. “Heterogeneous versus Homogeneous Crystal Nucleation of Hard Spheres”. In: *Soft Matter* 15.47 (2019), pp. 9625–9631.

[27] Nicholas Wood et al. “Coupling of Sedimentation and Liquid Structure: Influence on Hard Sphere Nucleation”. In: *J. Chem. Phys.* 149.20 (Nov. 2018), p. 204506.

[28] Wilkin Wöhler and Tanja Schilling. “Hard Sphere Crystal Nucleation Rates: Reconciliation of Simulation and Experiment”. In: *Phys. Rev. Lett.* 128.23 (2022), p. 238001.

[29] Klaus Schätzel and Bruce J Ackerson. “Density Fluctuations during Crystallization of Colloids”. In: *Phys. Rev. E* 48.5 (1993), p. 3766.

[30] Y. He et al. “Dynamics of Crystallization in Hard-Sphere Suspensions”. In: *Phys. Rev. E* 54.5 (1996), p. 5286.

[31] Chr Sinn et al. “Solidification Kinetics of Hard-Sphere Colloidal Suspensions”. In: *Trends in Colloid and Interface Science XV* (2001), pp. 266–275.

[32] JL Harland et al. “Observation of Accelerated Nucleation in Dense Colloidal Fluids of Hard Sphere Particles”. In: *Phys. Rev. Lett.* 75.19 (1995), p. 3572.

[33] Sara Iacopini, Thomas Palberg, and Hans Joachim Schöpe. “Crystallization Kinetics of Polydisperse Hard-Sphere-like Microgel Colloids: Ripening Dominated Crystal Growth above Melting”. In: *J. Chem. Phys.* 130.8 (2009), p. 084502.

[34] Jade Taffs et al. “Structure and Kinetics in the Freezing of Nearly Hard Spheres”. In: *Soft Matter* 9 (2013), pp. 297–305.

[35] Markus Franke, Sebastian Golde, and Hans Joachim Schöpe. “Solidification of a Colloidal Hard Sphere like Model System Approaching and Crossing the Glass Transition”. In: *Soft Matter* 10.29 (2014), pp. 5380–5389.

[36] S. Auer and D. Frenkel. “Prediction of Absolute Crystal Nucleation Rate in Hard-Sphere Colloids”. In: *Nature* 409 (2001), pp. 1020–1023.

[37] Stefan Auer and Daan Frenkel. “Suppression of Crystal Nucleation in Polydisperse Colloids Due to Increase of the Surface Free Energy”. In: *Nature* 413.6857 (2001), pp. 711–713.

[38] L. Filion et al. “Simulation of Nucleation in Almost Hard-Sphere Colloids: The Discrepancy between Experiment and Simulation Persists”. In: *J. Chem. Phys.* 134.13 (Apr. 2011), p. 134901.

[39] Tanja Schilling et al. “Crystallization in Suspensions of Hard Spheres: A Monte Carlo and Molecular Dynamics Simulation Study”. In: *Journal of Physics: Condensed Matter* 23.19 (2011), p. 194120.

[40] Giulia Fiorucci et al. “The Effect of Hydrodynamics on the Crystal Nucleation of Nearly Hard Spheres”. In: *J. Chem. Phys.* 152.6 (2020), p. 064903.

[41] L. Kürten et al. “The Energy Barrier of Precritical Nuclei in Hard Spheres Is Consistent with Predictions”. In: *ArXiV* (2025), p. 2503.17270.

[42] S. Kale et al. “Approaching the Hard Sphere Limit in Colloids Suitable for Confocal Microscopy - the End of a Decade Lasting Quest”. In: *Soft Matter* (2023).

[43] S. E. Paulin and B. J. Ackerson. “Observation of a Phase Transition in the Sedimentation Velocity of Hard Spheres”. In: *Phys. Rev. Lett.* 64 (1990), pp. 2663–2666.

[44] A. Ivlev et al. *Complex Plasmas and Colloidal Dispersions: Particle-Resolved Studies of Classical Liquids and Solids*. Singapore: World Scientific Publishing Co., Singapore Scientific, 2012.

[45] Bhuvnesh Bharti and Orlin D. Velev. “Assembly of Reconfigurable Colloidal Structures by Multidirectional Field-Induced Interactions”. In: *Langmuir* 31.29 (July 2015), pp. 7897–7908.

[46] Joe G. Donaldson, Per Linse, and Sofia S. Kantorovich. “How cube-like must magnetic nanoparticles be to modify their self-assembly?” In: *Nanoscale* 9.19 (2017), pp. 6448–6462.

[47] Ekaterina V. Novak et al. “The structure of clusters formed by Stockmayer supracolloidal magnetic polymers”. In: *The European Physical Journal E* 42.12 (Dec. 2019), p. 158.

[48] Anand Yethiraj and Alfons Van Blaaderen. “A Colloidal Model System with an Interaction Tunable from Hard Sphere to Soft and Dipolar”. In: *Nature* 421.6922 (Jan. 2003), pp. 513–517.

[49] M. Klokkenburg et al. “Dipolar structures in magnetite ferrofluids studied with small-angle neutron scattering with and without applied magnetic field”. In: *Physical Review E* 75.5 (May 2007), p. 051408.

[50] A. Wiedenmann et al. “Low-temperature dynamics of magnetic colloids studied by time-resolved small-angle neutron scattering”. In: *Physical Review B* 77.18 (May 2008), p. 184417.

[51] A. P. Hynninen and M. Dijkstra. “Phase Diagram of Dipolar Hard and Soft Spheres: Manipulation of Colloidal Crystal Structures by an External Field”. In: *Physical Review Letters* 94.13 (Apr. 2005), p. 138303.

[52] W. Gispen et al. “Crystal Polymorph Selection Mechanism of Hard Spheres Hidden in the Fluid”. In: *ACS Nano* 17 (2023), pp. 8807–8814.

[53] W. Ostwald. “Studien Über Die Bildung Und Umwandlung Fester Körper: 1. Abhandlung: Übersättigung Und Überkaltung”. In: *Zeitschrift für Physikalische Chemie* 22U.1 (Feb. 1, 1897), pp. 289–330.

[54] Daphne Klotsa and Robert L. Jack. “Predicting the Self-Assembly of a Model Colloidal Crystal”. In: *Soft Matter* 7.13 (2011), p. 6294.

[55] Daphne Klotsa and Robert L. Jack. “Controlling Crystal Self-Assembly Using a Real-Time Feedback Scheme”. In: *The Journal of Chemical Physics* 138.9 (Mar. 7, 2013).

[56] Stephen Whitelam and Robert L. Jack. “The Statistical Mechanics of Dynamic Pathways to Self-Assembly”. In: *Annu. Rev. Phys. Chem.* 66.1 (Apr. 2015), pp. 143–163.

[57] Kyle J.M. Bishop, Sibani Lisa Biswal, and Bhuvnesh Bharti. “Active Colloids as Models, Materials, and Machines”. In: *Annual Review of Chemical and Biomolecular Engineering* 14.1 (June 2023), pp. 1–30.

[58] D. Needleman and Z. Dogic. “Active matter at the interface between materials science and cell biology”. In: *Nat. Rev. Mater* 2.9 (2017), p. 17048.

[59] M. F. Hagan and A. Baskaran. “Emergent self-organization in active materials”. In: *Curr. Op. Cell Biol.* 38 (2016), pp. 74–80.

[60] M. C. Marchetti et al. “Hydrodynamics of Soft Active Matter”. In: *Rev. Mod. Phys.* 85.3 (July 2013), pp. 1143–1189.

[61] David Richard, Hartmut Löwen, and Thomas Speck. “Nucleation pathway and kinetics of phase-separating active Brownian particles”. In: *Soft Matter* 12.24 (2016), pp. 5257–5264.

[62] C. Bechinger et al. “Active Particles in Complex and Crowded Environments”. In: *Rev. Mod. Phys.* 88 (2016), p. 045006.

[63] S. Ramaswamy. “The Mechanics and Statistics of Active Matter”. In: *Annu. Rev. Condens. Matter Phys* 1 (2010), p. 323.

[64] Mark J. Bowick et al. “Symmetry, Thermodynamics, and Topology in Active Matter”. In: *Physical Review X* 12.1 (Feb. 2022), p. 010501.

[65] J. Schwarz-Linek et al. “Phase separation and rotor self-assembly in active particle suspensions”. In: *Proc. Natl. Acad. Sci.* 109.11 (Mar. 2012). ISBN: 1091-6490 (Electronic)$\backslash$n0027-8424 (Linking) _eprint: arXiv:1404.2263v1, pp. 4052–4057.

[66] M. Czajkowski et al. “Hydrodynamics of shape-driven rigidity transitions in motile tissues”. In: *Soft Matter* 14.27 (2018). Publisher: The Royal Society of Chemistry, pp. 5628–5642.

[67] V. Petrolli et al. “Confinement-Induced Transition between Wavelike Collective Cell Migration Modes”. In: *Phys. Rev. Lett.* 122.16 (Apr. 2019). Publisher: American Physical Society, p. 168101.

[68] A Attanasi et al. “Collective behaviour without collective order in wild swarms of midges”. In: *PLoS Comput. Biol.* 10.7 (July 2014). Publisher: Public Library of Science, e1003697–e1003697.

[69] S. A. Mallory, C. Valeriani, and A. Cacciuto. “An Active Approach to Colloidal Self-Assembly”. In: *Annual Review of Physical Chemistry* 69.1 (2018), pp. 59–79.

[70] Sidney R. Nagel. “Experimental soft-matter science”. In: *Reviews of Modern Physics* 89.2 (Apr. 2017), p. 025002.

[71] O. Dauchot, F. Ladieu, and Royall C. P. “The Glass Transition in Molecules, Colloids and Grains: Universality and Specificity”. In: *accepted in Comptes Rendus. Physique, online at arXiv* 2211.03158 (2022).

[72] Wilson Poon. “Colloids as Big Atoms”. In: *Science* 304.5672 (May 2004), pp. 830–831.

[73] J. W. Vanderhoff et al. “Some Factors Involved in the Preparation of Uniform Particle Latices”. In: *J Poly. Sci.* 20 (1956), pp. 225–234.

[74] T. F. Tadros. *Formulation Science and Technology*. De Gruyter, 2018.

[75] F. Charles Frank. “Supercooling of Liquids”. In: *Proc. R. Soc. A.* 215 (1952), pp. 43–46.

[76] C. Likos. “Effective interactions in soft condensed matter physics”. In: *Phys. Rep.* 348 (2001), pp. 267–439.

[77] R. P. A. Dullens et al. “Monodisperse Core-Shell Poly(Methyl Methacrylate) Latex Colloids”. In: *Langmuir* 19 (2003), pp. 5963–5966.

[78] X. Wu et al. “Tuning Higher Order Structure in Colloidal Fluids”. In: *Soft Matter* 21 (2025), pp. 2787–2802.

[79] Nigel B. Wilding and Peter Sollich. “Phase Behavior of Polydisperse Spheres: Simulation Strategies and an Application to the Freezing Transition”. In: *J. Chem. Phys.* 133.22 (Dec. 2010), p. 224102.

[80] B. J. Alder and T. E. Wainwright. “Phase Transition for a Hard Sphere System”. In: *J. Chem. Phys.* 27 (1957), pp. 1208–1209.

[81] W. W. Wood and J. D. Jacobson. “Preliminary Results from a Recalculation of the Monte Carlo Equation of State of Hard Spheres”. In: *J. Chem. Phys.* 27 (1957), pp. 1207–1208.

[82] P. N. Pusey and W. Van Megen. “Phase Behaviour of Concentrated Suspensions of Nearly Hard Colloidal Spheres”. In: *Nature* 320 (1986), pp. 340–342.

[83] Norman F. Carnahan and Kenneth E. Starling. “Equation of State for Nonattracting Rigid Spheres”. In: *J. Chem. Phys.* 51.2 (July 1969), pp. 635–636.

[84] R. Hall K. “Another Hard-Sphere Equation of State”. In: *J. Chem. Phys.* 57 (1972), p. 2225.

[85] Peter Sollich and Nigel B. Wilding. “Crystalline Phases of Polydisperse Spheres”. In: *Phys. Rev. Lett.* 104.11 (Mar. 2010), p. 118302.

[86] David A. Kofke and Peter G. Bolhuis. “Freezing of Polydisperse Hard Spheres”. In: *Phys. Rev. E* 59.1 (Jan. 1999), pp. 618–622.

[87] M Fasolo and Peter Sollich. “Fractionation Effects in Phase Equilibria of Polydisperse Hard-Sphere Colloids”. In: *Phys. Rev. E* 70 (2004), p. 041410.

[88] M. A. Rutgers et al. “Measurement of the Hard-Sphere Equation of State Using Screened Charged Polystyrene Colloids”. In: *Phys. Rev. B* 53.9 (Mar. 1996), pp. 5043–5046.

[89] W. Russel, D. Saville, and W. Schowalter. *Colloidal Dispersions*. Cambridge: Cambridge Univ. Press, 1989.

[90] Antti-Pekka Hynninen and Marjolein Dijkstra. “Phase Diagrams of Hard-Core Repulsive Yukawa Particles”. In: *Phys. Rev. E* 68.2 (2003), p. 021407.

[91] Ramin Golestanian and Sriram Ramaswamy. “Active Matter”. In: *The European Physical Journal E* 36.6 (June 2013), 67, epje/i2013–13067–2.

[92] T. J. Pedley and J. O. Kessler. “Hydrodynamic Phenomena in Suspensions of Swimming Microorganisms”. In: *Annual Review of Fluid Mechanics* 24.1 (Jan. 1992), pp. 313–358.

[93] Michael Sinhuber and Nicholas T. Ouellette. “Phase Coexistence in Insect Swarms”. In: *Physical Review Letters* 119.17 (Oct. 2017), p. 178003.

[94] Lutz Schimansky-Geier et al. “Structure formation by active Brownian particles”. In: *Physics Letters A* 207.3-4 (Oct. 1995), pp. 140–146.

[95] Frank Schweitzer, Werner Ebeling, and Benno Tilch. “Complex Motion of Brownian Particles with Energy Depots”. In: *Physical Review Letters* 80.23 (June 1998), pp. 5044–5047.

[96] Jonathan R. Howse et al. “Self-Motile Colloidal Particles: From Directed Propulsion to Random Walk”. In: *Physical Review Letters* 99.4 (July 2007), p. 048102.

[97] Xu Zheng et al. “Non-Gaussian statistics for the motion of self-propelled Janus particles: Experiment versus theory”. In: *Physical Review E* 88.3 (Sept. 2013), p. 032304.

[98] F. C. Walsh. “Janus particles: features, synthesis and potential uses, including surface functionalisation”. In: *Transactions of the IMF* 102.1 (Jan. 2024), pp. 4–8.

[99] Shan Jiang and Steve Granick. “Preface – An Introduction to Janus Particles”. In: *Janus particle synthesis, self-assembly and applications*. Ed. by Shan Jiang and Steve Granick. The Royal Society of Chemistry, Oct. 2012, pp. 5–14.

[100] C Casagrande et al. ““Janus Beads”: Realization and Behaviour at Water/Oil Interfaces”. In: *Europhysics Letters (EPL)* 9.3 (June 1989), pp. 251–255.

[101] Pierre-Gilles de Gennes. *Soft Matter (Nobel Lecture)*. Nobel Lecture. 1991.

[102] Walter F. Paxton et al. “Catalytic Nanomotors: Autonomous Movement of Striped Nanorods”. In: *Journal of the American Chemical Society* 126.41 (Oct. 2004), pp. 13424–13431.

[103] S. Gangwal et al. “Induced-Charge Electrophoresis of Metallodielectric Particles”. In: *Phys. Rev. Lett.* 100.5 (2008), p. 058302.

[104] Katherine Skipper. “Dipolar colloids: Higher-order structure, activity and phase behaviour”. PhD thesis. University of Bristol, Sept. 2023.

[105] Nariaki Sakaï et al. “Dipolar colloids in three dimensions: non-equilibrium structure and re-entrant dynamics”. In: *Soft Matter* 21.26 (2025), pp. 5204–5213.

[106] Xichen Chao et al. “Traveling Strings of Active Dipolar Colloids”. In: *Physical Review Letters* 134.1 (Jan. 2025), p. 018302.

[107] A. Yethiraj. “Tunable Colloids: Comtrol of Phase Transitons with Tunable Interatctions”. In: *Soft Matter* 3 (2007), pp. 1–19.

[108] J.W. Gibbs. In: 3 (1878), p. 108.

[109] Stefan Auer and Daan Frenkel. “Numerical Prediction of Absolute Crystallization Rates in Hard-Sphere Colloids”. In: *J. Chem. Phys.* 120.6 (2004), pp. 3015–3029.

[110] Vitaly I Kalikmanov. “Classical Nucleation Theory”. In: *Nucleation Theory*. Springer, 2012, pp. 17–41.

[111] M. Volmer and A. Weber. “Keimbildung in Übersättigten Gebilden”. In: *Z. Phys. Chem.* 119 (1926), p. 227.

[112] R. Becker and W. Doring. “Kinetische Behandlung Der Keimbildung in Übersättigten Dämpfen”. In: *Ann. Phys.* 24 (1935), p. 719.

[113] P. Debenedetti. *Metastable Liquids*. Princeton University, Princeton, NJ, 1996.

[114] John Russo and Hajime Tanaka. “Crystal Nucleation as the Ordering of Multiple Order Parameters”. In: *J. Chem. Phys.* 145.21 (2016), p. 211801.

[115] Swetlana Jungblut and Christoph Dellago. “Pathways to Self-Organization: Crystallization via Nucleation and Growth”. In: *The European Physical Journal E* 39.8 (2016), pp. 1–38.

[116] John Russo and Hajime Tanaka. “Nonclassical Pathways of Crystallization in Colloidal Systems”. In: *MRS Bulletin* 41.5 (2016), pp. 369–374.

[117] Tanja Schilling et al. “Precursor-Mediated Crystallization Process in Suspensions of Hard Spheres”. In: *Phys. Rev. Lett.* 105.2 (2010), p. 025701.

[118] J. Russo and H. Tanaka. “The Microscopic Pathway to Crystallization in Supercooled Liquids”. In: *Sci. Rep.* 2 (2012), p. 505.

[119] David Richard and Thomas Speck. “Crystallization of Hard Spheres Revisited. I. Extracting Kinetics and Free Energy Landscape from Forward Flux Sampling”. In: *J. Chem. Phys.* 148.12 (2018), p. 124110.

[120] Anja Kuhnhold et al. “Derivation of an Exact, Nonequilibrium Framework for Nucleation: Nucleation Is a Priori Neither Diffusive nor Markovian”. In: *Phys. Rev. E* 100.5 (2019), p. 052140.

[121] Camilla Beneduce et al. “Falsifiability Test for Classical Nucleation Theory”. In: *Physical Review Letters* 134.14 (Apr. 2025), p. 148201.

[122] Willem Gispen and Marjolein Dijkstra. “Finding the differences: Classical nucleation perspective on homogeneous melting and freezing of hard spheres”. In: *The Journal of Chemical Physics* 160.14 (Apr. 2024), p. 141102.

[123] Sung-Yoon Chung et al. “Multiphase transformation and Ostwald’s rule of stages during crystallization of a metal phosphate”. In: *Nature Physics* 5.1 (Jan. 2009), pp. 68–73.

[124] Conrado José Aparicio Bádenas and Maria Pau Ginebra Molins. *Biomineralization and biomaterials: fundamentals and applications*. Woodhead publishing series in biomaterials 104. Amsterdam Paris: Woodhead publishing, 2016.

[125] Klaus Schätzel and Bruce J Ackerson. “Observation of Density Fluctuations”. In: *Phys. Rev. Lett.* 68.3 (1992), p. 337.

[126] P.N. Pusey. *Introduction to Scattering Experiments. Neutrons, X-rays and Light: Scattering Methods Applied to Soft Condensed Matter*. 2002.

[127] J Il Langford and AJC Wilson. "Scherrer after sixty years: a survey and some new results in the determination of crystallite size". In: *Journal of applied crystallography* 11.2 (1978). Publisher: International Union of Crystallography, pp. 102–113.

[128] Johannes Möller et al. "Crystal Nucleation in Supercooled Atomic Liquids". In: *Phys. Rev. Lett.* 132.20 (May 2024), p. 206102.

[129] Anders Nilsson. "Origin of the anomalous properties in supercooled water based on experimental probing inside "no-man's land"". In: *Journal of Non-Crystalline Solids: X* 14 (June 2022), p. 100095.

[130] J. A. Sellberg et al. "Ultrafast X-ray probing of water structure below the homogeneous ice nucleation temperature". In: *Nature* 510.7505 (June 2014), pp. 381–384.

[131] J. L. Harland and W. van Megen. "Crystallization Kinetics of Suspensions of Hard Colloidal Spheres". In: *Phys. Rev. E.* 55 (1997), pp. 3054–3067.

[132] G. Bosma et al. "Preparation of Monodisperse, Fluorescent PMMA-latex Colloids by Dispersion Polymerization". In: *J. Coll. Interf. Sci.* 245.2 (Jan. 2002), pp. 292–300.

[133] Vasili Baranau and Ulrich Tallarek. "Random-close packing limits for monodisperse and polydisperse hard spheres". In: *Soft Matter* 10.21 (2014), p. 3826.

[134] A. Kose et al. "Direct Observation of Ordered Latex Suspension by Metallurgical Microscope". In: *J. Coll. Interf. Sci.* (1973).

[135] Akira Kose and Sei Hachisu. "Ordered Structure in Weakly Flocculated Monodisperse Latex". In: *Journal of Colloid and Interface Science* 55.3 (1976), pp. 487–498.

[136] S. Okamoto and S. Hachisu. "Ordered Structure in Monodisperse Gold Sol". In: *J. Coll. Interf. Sci.* 62 (1977), pp. 172–181.

[137] John Oreopoulos, Richard Berman, and Mark Browne. "Spinning-disk confocal microscopy". In: *Methods in Cell Biology*. Vol. 123. Elsevier, 2014, pp. 153–175.

[138] J. C. Crocker and D. G. Grier. "Methods of Digital Video Microscopy for Colloidal Studies". In: *J. Coll. Interf. Sci.* 179 (1995), pp. 298–310.

[139] Daniel B. Allan et al. *soft-matter/trackpy: Trackpy v0.4.2*. Oct. 2019.

[140] John C. Crocker and David G. Grier. "Microscopic measurement of the pair interaction potential of charge-stabilized colloid". In: *Physical Review Letters* 73.2 (July 1994), pp. 352–355.

[141] William W. Wood. “Note on the Free Volume Equation of State for Hard Spheres”. In: *J. Chem. Phys.* 20.8 (1952), pp. 1334–1334.

[142] D. Frenkel and B. Smit. *Understanding Molecular Simulation: From Algorithms to Applications*. 2nd ed. Elsevier, 2002.

[143] Dennis C Rapaport. *The Art of Molecular Dynamics Simulation*. Cambridge university press, 2004.

[144] Michael P. Allen and Dominic J. Tildesley. *Computer Simulation of Liquids*. 2nd ed. Oxford University PressOxford, June 22, 2017.

[145] Aidan P Thompson et al. “LAMMPS-a Flexible Simulation Tool for Particle-Based Materials Modeling at the Atomic, Meso, and Continuum Scales”. In: *Computer Physics Communications* 271 (2022), p. 108171.

[146] Joshua A Anderson et al. “Massively Parallel Monte Carlo for Many-Particle Simulations on GPUs”. In: *J. Comput. Phys.* 254 (2013), pp. 27–38.

[147] Joshua A Anderson, Jens Glaser, and Sharon C Glotzer. “HOOMD-blue: A Python Package for High-Performance Molecular Dynamics and Hard Particle Monte Carlo Simulations”. In: *Computational Materials Science* 173 (2020), p. 109363.

[148] B Cichocki and K Hinsen. “Dynamic Computer Simulation of Concentrated Hard Sphere Suspensions: I. Simulation Technique and Mean Square Displacement Data”. In: *Physica A: Statistical Mechanics and its Applications* 166.3 (1990), pp. 473–491.

[149] E Sanz and D Marenduzzo. “Dynamic Monte Carlo versus Brownian Dynamics: A Comparison for Self-Diffusion and Crystallization in Colloidal Fluids”. In: *J. Chem. Phys.* 132.19 (2010), p. 194102.

[150] J. S. Van Duijneveldt and D. Frenkel. “Computer simulation study of free energy barriers in crystal nucleation”. In: *The Journal of Chemical Physics* 96.6 (Mar. 1992), pp. 4655–4668.

[151] Glenn M Torrie and John P Valleau. “Nonphysical Sampling Distributions in Monte Carlo Free-Energy Estimation: Umbrella Sampling”. In: *J. Comput. Phys.* 23.2 (1977), pp. 187–199.

[152] Johannes Kästner. “Umbrella Sampling”. In: *Wiley Interdisciplinary Reviews: Computational Molecular Science* 1.6 (2011), pp. 932–942.

[153] R. P. Feynman. *Statistical Mechanics*. Westview press, 1998.

[154] David Chandler. *Introduction to modern statistical mechanics*. New York: Oxford University Press, 1987.

[155] Harry L. Frisch, Joel L. Lebowitz, and Stuart A. Rice. "*The Equilibrium Theory of Classical Fluids*". In: *Physics Today* 18.5 (May 1965), pp. 78–80.

[156] M López De Haro and M Robles. "The structure factor and equation of state of hard-sphere fluids". In: *Journal of Physics: Condensed Matter* 16.22 (June 2004), S2089–S2096.

[157] M. S. Wertheim. "Exact Solution of the Percus-Yevick Integral Equation for Hard Spheres". In: *Phys. Rev. Lett.* 10.8 (1963), p. 321.

[158] Masaharu Tanemura et al. "Geometrical Analysis of Crystallization of the Soft-Core Model". In: *Prog. Theo. Phys.* 58.4 (Oct. 1977), pp. 1079–1095.

[159] C. Patrick Royall, Stephen R. Williams, and Hajime Tanaka. "Vitrification and Gelation in Sticky Spheres". In: *J. Chem. Phys.* 148.4 (Jan. 2018), p. 044501.

[160] J. D. Honeycutt and H. C. Andersen. "Molecular dynamics study of melting and freezing of small Lennard-Jones clusters". In: *J. Phys. Chem.* 91 (1987), pp. 4950–4963.

[161] P. J. Steinhardt, David R. Nelson, and M. Ronchetti. "Bond-Orientational Order In Liquids and Glasses". In: *Phys. Rev. B* 28 (1983), pp. 784–805.

[162] A. Malins et al. "Identification of Structure in Condensed Matter with the Topological Cluster Classification". In: *J. Chem. Phys.* (2013), p. 21.

[163] K. Skipper, F. J. Moore, and C. P. Royall. "Identification and Classification of Clusters of Dipolar Colloids in an External Field". In: *Journal of Chemical Physics* 161 (2024), p. 144308.

[164] Jade Taffs and C. P. Royall. "The Role of Fivefold Symmetry in Suppressing Crystallization". In: *Nature communications* 7.1 (2016), pp. 1–7.

[165] A. Malins et al. "Lifetimes and Lengthscales of Structural Motifs in a Model Glassformer". In: *Faraday Discuss.* 167 (2013), p. 405.

[166] D. S. Franzblau. "Computation of ring statistics for network models of solids". In: *Phys. Rev. B* 44.10 (Sept. 1991), pp. 4925–4930.

[167] Joshua F. Robinson et al. "Morphometric Approach to Many-Body Correlations in Hard Spheres". In: *Phys. Rev. Lett.* 122.6 (Feb. 2019), p. 068004.

[168] Alex Malins et al. "Identification of Long-Lived Clusters and Their Link to Slow Dynamics in a Model Glass Former". In: *J. Chem. Phys.* 138.12 (Mar. 2013), 12A535.

[169] Pieter-Reináten Wolde et al. "Simulation of Homogeneous Crystal Nucleation Close to Coexistence". In: *Faraday discussions* 104 (1996), pp. 93–110.

[170] Georges Voronoi. “Nouvelles applications des paramètres continus à la théorie des formes quadratiques. Premier mémoire. Sur quelques propriétés des formes quadratiques positives parfaites.” In: *Journal für die reine und angewandte Mathematik (Crelles Journal)* 1908.133 (Jan. 1908), pp. 97–102.

[171] J.L Finney. “A procedure for the construction of Voronoi polyhedra”. In: *Journal of Computational Physics* 32.1 (July 1979), pp. 137–143.

[172] Jacobus A van Meel et al. “A Parameter-Free, Solid-Angle Based, Nearest-Neighbor Algorithm”. In: *The Journal of chemical physics* 136.23 (2012).

[173] A. Kawafi. “Machine Learning for 3D Bioimage Analysis”. PhD thesis. University of Bristol, 2023.

[174] Abdelwahab Kawafi et al. “Colloidoscope: Detecting Dense Colloids in 3D with Deep Learning”. In: *Soft Matter* (2025).

[175] G L Hunter and E R Weeks. “The Physics of the Colloidal Glass Transition”. In: *Rep Prog Phys* (2012), p. 31.

[176] Maximilian Robert Bailey, Fabio Grillo, and Lucio Isa. “Tracking Janus Microswimmers in 3D with Machine Learning”. In: *Soft Matter* 18 (2022), p. 7291.

[177] Jay M. Newby et al. “Convolutional Neural Networks Automate Detection for Tracking of Submicron-Scale Particles in 2D and 3D”. In: *Proceedings of the National Academy of Sciences* 115.36 (Sept. 4, 2018), pp. 9026–9031.

[178] Benjamin Midtvedt et al. “Quantitative Digital Microscopy with Deep Learning”. In: *Applied Physics Reviews* 8.1 (Mar. 1, 2021), p. 011310.

[179] Benjamin Midtvedt et al. “Single-Shot Self-Supervised Object Detection in Microscopy”. In: *Nature Communications* 13.1 (Dec. 5, 2022), p. 7492.

[180] Abolfazl Zargari et al. “Enhanced Cell Segmentation with Limited Training Datasets Using Cycle Generative Adversarial Networks”. In: *iScience* 27.5 (May 2024), p. 109740.

[181] Matthew Bierbaum et al. “Light Microscopy at Maximal Precision”. In: *Phys. Rev. X* 7.4 (Oct. 2017), p. 041007.

[182] Özgün Çiçek et al. “3D U-Net: Learning Dense Volumetric Segmentation from Sparse Annotation”. In: *Medical Image Computing and Computer-Assisted Intervention – MICCAI 2016*. Ed. by Sebastien Ourselin et al. Vol. 9901. Cham: Springer International Publishing, 2016, pp. 424–432.

[183] Joshua A. Anderson, M. Eric Irrgang, and Sharon C. Glotzer. “Scalable Metropolis Monte Carlo for Simulation of Hard Shapes”. In: *Computer Physics Communications* 204 (July 2016), pp. 21–30.

[184] Bo Zhang, Josiane Zerubia, and Jean-Christophe Olivo-Marin. “Gaussian Approximations of Fluorescence Microscope Point-Spread Function Models”. In: *Applied Optics* 46.10 (Apr. 1, 2007), p. 1819.

[185] Ken Perlin. “An Image Synthesizer”. In: *ACM SIGGRAPH Computer Graphics* 19.3 (July 1985), pp. 287–296.

[186] Aiden Nibali et al. *Numerical Coordinate Regression with Convolutional Neural Networks*. Version 2. 2018. (Visited on 08/31/2025). Pre-published.

[187] J.-P. Hansen and I.R. McDonald. *Theory of Simple Liquids*. 4th ed. Academic, London, 2013.

[188] Lars Kürten et al. *The Free-Energy Barrier of Precritical Nuclei in Hard Spheres Is Consistent with Predictions*. June 3, 2025. (Visited on 07/25/2025). Pre-published.

[189] R. Pinchaipat et al. “Experimental Evidence for a Structural-Dynamical Transition in Trajectory Space”. In: *Phys. Rev. Lett.* 119.2 (July 2017), p. 028004.

[190] A. R. Finney and M. Salvalaglio. “Molecular Simulation Approaches to Study Crystal Nucleation from Solutions: Theoretical Considerations and Computational Challenges”. In: *WIREs Comput. Mol. Sci.* (2023), e1697.

[191] A. Z. Panagiotopoulos. “Simulations of activities, solubilities, transport properties, and nucleation rates for aqueous electrolyte solutions”. In: *Journal of Chemical Physics* 153 (2020), p. 010903.

[192] C. P. Lamas et al. “Homogeneous nucleation of NaCl in supersaturated solutions”. In: *Physical Chemistry Chemical Physics* 23 (2021), p. 26843.

[193] Rosalind J Allen, Chantal Valeriani, and Pieter Rein Ten Wolde. “Forward Flux Sampling for Rare Event Simulations”. In: *Journal of physics: Condensed matter* 21.46 (2009), p. 463102.

[194] Peter G Bolhuis and David WH Swenson. “Transition Path Sampling as Markov Chain Monte Carlo of Trajectories: Recent Algorithms, Software, Applications, and Future Outlook”. In: *Advanced Theory and Simulations* 4.4 (2021), p. 2000237.

[195] P. Tan, N. Xu, and L. Xu. “Visualizing Kinetic Pathways of Homogeneous Nucleation in Colloidal Crystallization”. In: *Nature Physics* 10.1 (2014), pp. 73–79.

[196] Stefan Auer and Daan Frenkel. “Crystallization of Weakly Charged Colloidal Spheres: A Numerical Study”. In: *J. Phys.: Condens. Matter* 14.33 (Aug. 2002), pp. 7667–7680.

[197] Stefania Ketzetzi, John Russo, and Daniel Bonn. “Crystal Nucleation in Sedimenting Colloidal Suspensions”. In: *J. Chem. Phys.* 148.6 (2018), p. 064901.

[198] John Russo et al. “The Interplay of Sedimentation and Crystallization in Hard-Sphere Suspensions”. In: *Soft Matter* 9.30 (2013), p. 7369.

[199] Frank Smallenburg. “Efficient Event-Driven Simulations of Hard Spheres”. In: *The European Physical Journal E* 45.3 (2022), pp. 1–10.

[200] J. A. Barker and D. Henderson. “What Is "Liquid"? Understanding the States of Matter”. In: *Rev. Mod. Phys.* 48 (1976), pp. 587–671.

[201] James E. Hallett, Francesco Turci, and C. Patrick Royall. “Local Structure in Deeply Supercooled Liquids Exhibits Growing Lengthscales and Dynamical Correlations”. In: *Nat Commun* 9.1 (Dec. 2018), p. 3272.

[202] PN Pusey et al. “Hard Spheres: Crystallization and Glass Formation”. In: *Philosophical Transactions of the Royal Society A: Mathematical, Physical and Engineering Sciences* 367.1909 (2009), pp. 4993–5011.

[203] C. P. Royall, R. van Roij, and A. Van Blaaderen. “Extended Sedimentation Profiles in Charged Colloids: The Gravitational Length, Entropy, and Electrostatics”. In: *Journal of Physics: Condensed Matter* 17 (2005), pp. 2315–2326.

[204] Kengo Ichiki and Hisao Hayakawa. “Dynamical Simulation of Fluidized Beds: Hydrodynamically Interacting Granular Particles”. In: *Physical Review E* 52.1 (July 1, 1995), pp. 658–670.

[205] P. G. Debenedetti et al. “Special Topic Preface: Nucelation–Current Understanding Approaching 150 Years after Gibbs”. In: *Journal of Chemical Physics* 160 (2024), p. 100401.

[206] John Bauer et al. “Ritonavir: An Extraordinary Example of Conformational Polymorphism”. In: *Pharmaceutical Research* 18.6 (June 2001), pp. 859–866.

[207] K. Sandomirski, H. Allahyarov E.Loewen, and S. U. Egelhaaf. “Heterogeneous Crystallization of Hard-Sphere Colloids near a Wall”. In: *Soft Matter* 7 (2011), p. 8050.

[208] A. M. Alsayed et al. “Premelting at Defects within Bulk Colloidal Crystals”. In: *Science* 309 (2005), pp. 1207–1210.

[209] F. Turci and C. P. Royall. “Crystallisation Driven by Sedimentation: A Particle Resolved Study”. In: *J. Stat. Mech.: Theory and Experiment* (2016), p. 084004.

[210] Fabio Leoni and John Russo. “Nonclassical Nucleation Pathways in Stacking-Disordered Crystals”. In: *Physical Review X* 11.3 (2021), p. 031006.

[211] S. Arai and H. Tanaka. “Surface-Assisted Single-Crystal Formation of Charged Colloids”. In: *Nature Phys.* 13 (2017), pp. 503–510.

[212] Hideyo Tsurusawa et al. “Formation of Porous Crystals via Viscoelastic Phase Separation.” In: *Nature Materials* 16 (2017), p. 1022.

[213] Anand Yethiraj et al. “Nature of an Electric-Field-Induced Colloidal Martensitic Transition”. In: *Physical Review Letters* 92 (2004), p. 058301.

[214] P. S. Mohanty et al. “Mutiple Path-Dependent Routes for Phase-Transition Kinetics in Thermoresponsive and Field-Responsive Ultrasoft Colloids”. In: *Physical Review X* 5 (2015), p. 011030.

[215] Andrew I Campbell and Paul Bartlett. “Fluorescent Hard-Sphere Polymer Colloids for Confocal Microscopy”. In: *Journal of Colloid and Interface Science* 256.2 (2002), pp. 325–330.

[216] A. Donovan. “Arrest in Colloids with Competing Attractive and Repulsive Interactions”. PhD thesis. University of Bristol, 2006.

[217] M.E. Leunissen. “Manipulating Colloids with Charge and Electric Fields”. PhD thesis. Utrecht Universiteit, 2006.

[218] Fausto Martelli et al. “Connection between Liquid and Non-Crystalline Solid Phases in Water”. In: *The Journal of Chemical Physics* 153.10 (Sept. 14, 2020), p. 104503.

[219] Steve Plimpton. “Fast Parallel Algorithms for Short-Range Molecular Dynamics”. In: *J. Comp. Phys.* 117.1 (1995), pp. 1–19.

[220] J. D. Weeks, D. Chandler, and H. C. Andersen. “Role of Repulsive Forces in Determining the Equilibrium Structure of Simple Liquids”. In: *Journal of Chemical Physics* 54.12 (Jan. 1971), p. 5237.

[221] Zoltan K. Nagy and Richard D. Braatz. “Advances and New Directions in Crystallization Control”. In: *Annual Review of Chemical and Biomolecular Engineering* 3.1 (July 2012), pp. 55–75.

[222] Youngjo Kim et al. “Modeling of Nucleation, Growth, and Dissolution of Paracetamol in Ethanol Solution for Unseeded Batch Cooling Crystallization with Temperature-Cycling Strategy”. In: *Industrial & Engineering Chemistry Research* 62.6 (Feb. 2023), pp. 2866–2881.

[223] Richard D. Braatz. “Advanced control of crystallization processes”. In: *Annual Reviews in Control* 26.1 (Jan. 2002), pp. 87–99.

[224] Christopher J. Fullerton and Robert L. Jack. “Optimising self-assembly through time-dependent interactions”. In: *The Journal of Chemical Physics* 145.24 (Dec. 2016), p. 244505.

[225] C. Patrick Royall and Alex Malins. “The role of quench rate in colloidal gels”. In: *Faraday Discussions* 158 (2012), p. 301.

[226] M. T. Sullivan et al. “An Electric Bottle for Colloids”. In: *Physical Review Letters* 96.1 (Jan. 2006), p. 015703.

[227] Mirjam E. Leunissen and Alfons Van Blaaderen. “Concentrating Colloids with Electric Field Gradients. II. Phase Transitions and Crystal Buckling of Long-Ranged Repulsive Charged Spheres in an Electric Bottle”. In: *The Journal of Chemical Physics* 128.16 (Apr. 28, 2008).

[228] C. Patrick Royall and Stephen R. Williams. “The Role of Local Structure in Dynamical Arrest”. In: *Physics Reports* 560 (Feb. 2015), pp. 1–75.

[229] Michael Rubenstein, Alejandro Cornejo, and Radhika Nagpal. “Programmable self-assembly in a thousand-robot swarm”. In: *Science* 345.6198 (Aug. 2014), pp. 795–799.

[230] Justin Werfel, Kirstin Petersen, and Radhika Nagpal. “Designing Collective Behavior in a Termite-Inspired Robot Construction Team”. In: *Science* 343.6172 (Feb. 2014), pp. 754–758.

[231] J. Deseigne, O. Dauchot, and H. Chaté. “Collective Motion of Vibrated Polar Disks”. In: *Phys. Rev. Lett.* 105.9 (Aug. 2010). Publisher: American Physical Society, p. 098001.

[232] Andreas Zöttl and Holger Stark. “Modeling Active Colloids: From Active Brownian Particles to Hydrodynamic and Chemical Fields”. In: *Annual Review of Condensed Matter Physics* 14.1 (Mar. 2023), pp. 109–127.

[233] Jeremie Palacci et al. “Living Crystals of Light-Activated Colloidal Surfers”. In: *Science* 339.6122 (2013). ISBN: 1095-9203 (Electronic) 0036-8075 (Linking), pp. 936–940.

[234] Michael E. Cates and Julien Tailleur. “Motility-Induced Phase Separation”. In: *Annu. Rev. Condens. Matter Phys.* 6.1 (Mar. 2015), pp. 219–244.

[235] I. Buttinoni et al. “Dynamical Clustering and Phase Separation in Suspensions of Self-Propelled Colloidal Particles”. In: *Phys. Rev. Lett.* 110.23 (June 2013). ISBN: 0031-9007 _eprint: 1305.4185, p. 238301.

[236] Todd M. Squires and Martin Z. Bazant. “Breaking symmetries in induced-charge electro-osmosis and electrophoresis”. In: *Journal of Fluid Mechanics* 560 (Aug. 2006), pp. 65–101.

[237] Daiki Nishiguchi and Masaki Sano. “Mesoscopic turbulence and local order in Janus particles self-propelling under an ac electric field”. In: *Physical Review E* 92.5 (Nov. 2015), p. 052309.

[238] Jing Yan et al. “Reconfiguring active particles by electrostatic imbalance”. In: *Nature Materials* 15.10 (Oct. 2016), pp. 1095–1099.

[239] J. Stenhammar et al. “Phase behaviour of active Brownian particles: The role of dimensionality”. In: *Soft Matter* 10.10 (2014), pp. 1489–1499.

[240] Ahmad K Omar et al. “Phase Diagram of Active Brownian Spheres: Crystallization and the Metastability of Motility-Induced Phase Separation”. In: *Phys. Rev. Lett.* 126.18 (2021), p. 188002.

[241] Francesco Turci and Nigel B. Wilding. “Phase Separation and Multibody Effects in Three-Dimensional Active Brownian Particles”. In: *Physical Review Letters* 126.3 (Jan. 2021), p. 038002.

[242] Fergus Moore et al. “Active Brownian particles in random and porous environments”. In: *The Journal of Chemical Physics* 158.10 (Mar. 2023), p. 104907.

[243] Fergus J. Moore et al. “Crystallisation and polymorph selection in active Brownian particles”. In: *The European Physical Journal E* 44.9 (Sept. 2021), p. 121.

[244] V. Prymidis, H. Sielcken, and L. Filion. “Self-assembly of active attractive spheres”. In: *Soft Matter* 11 (2015), pp. 4158–4166.

[245] N. Sakaï and C. P. Royall. “Active Dipolar Colloids in Three Dimensions: Strings, Sheets, Labyrinthine Textures and Crystals”. In: *ArXiV* (2020), p. 2010.03925.

[246] C. Graf et al. “A General Method To Coat Colloidal Particles with Silica”. In: *Langmuir* 19.17 (2003), pp. 6693–6700.

[247] Mathieu Leocmach and Hajime Tanaka. “A Novel Particle Tracking Method with Individual Particle Size Measurement and Its Application to Ordering in Glassy Hard Sphere Colloids”. In: *Soft Matter* 9 (10.1039/C2SM27107A 2013), pp. 1447–1457.

RÉSUMÉ

Comprendre la nucléation des cristaux est d'une importance profonde tant pour des raisons fondamentales que technologiques. Dans le matériau le plus simple connu pour s'auto-assembler afin de former un cristal, les sphères dures, les prédictions les plus avancées et les mesures expérimentales des taux de nucléation diffèrent de plus de dix ordres de grandeur. En plus de remettre en question notre compréhension de la cristallisation, cela complique les tentatives d'utiliser l'auto-assemblage pour réaliser de nouveaux matériaux. Nous proposons ici une approche combinant expérience et simulation informatique pour relever les défis liés à la nucléation et à la réalisation de structures cristallines dans les colloïdes. Nous abordons la divergence de nucléation grâce à deux développements, basés sur des études en espace réel de colloïdes par microscopie confocale. Premièrement, nous considérons la barrière de nucléation en mesurant l'énergie libre de formation des noyaux pré-critiques, dont la fréquence d'apparition est suffisamment élevée pour être accessible expérimentalement grâce à la microscopie confocale. Deuxièmement, nous visons à cartographier les points d'état entre expérience et simulation avec une précision jusqu'ici inégalée. Pour ce faire, nous améliorons le suivi des particules avec des méthodes récemment développées intégrant l'apprentissage automatique et utilisons des fonctions de corrélation d'ordre supérieur, plus sensibles à la fraction volumique que les fonctions de corrélation par paires. Avec notre méthode, les barrières de nucléation présentent un accord raisonnable, ce qui conduit à la disparition de la divergence. De plus, à partir des données de microscopie confocale de prélèvements en sédimentation, nous avons constaté que les échelles de temps concurrentes de la sédimentation et de la cristallisation dans les expériences basées sur la méthode de Paulin-Ackerson, couramment utilisée pour déterminer le point d'état dans les expériences de diffusion de la lumière, pourraient conduire à une surestimation systématique de la fraction volumique et donc à l'apparition de la divergence. Enfin, nous étudions la nucléation cristalline dans un autre système modèle, les colloïdes dipolaires, dans lesquels les interactions dipolaires sont induites par un champ électrique externe. Le champ électrique peut être utilisé pour ajuster facilement l'intensité de l'interaction dipolaire, permettant l'étude de la sélection polymorphe et de la règle des étapes d'Ostwald. Ce qui est particulièrement intéressant ici est la formation d'un cristal métastable hexagonal compact (HCP). Celui-ci fond ensuite, après quoi un cristal BCT (la phase stable) se forme. Les mécanismes sous-jacents et la connexion avec la structure du fluide sont en cours d'investigation. De plus, les possibilités d'optimisation de la nucléation cristalline dans les systèmes dipolaires sont analysées en appliquant différents protocoles pour l'intensité de l'interaction dipolaire. Nous constatons que certains protocoles favorisent un assemblage plus rapide de domaines cristallins plus larges.

MOTS CLÉS

Matière condensée, Colloïdes, Nucléation

ABSTRACT

Understanding crystal nucleation is of profound importance for both fundamental and technological reasons. In the simplest known material that self-assembles to form a crystal—hard spheres—the most advanced predictions and experimental measurements of nucleation rates differ by more than ten orders of magnitude. In addition to challenging our understanding of crystallization, this complicates efforts to use self-assembly to create new materials. Here, we propose an approach combining experiment and computer simulation to address the challenges related to nucleation and the formation of crystalline structures in colloids. We address the nucleation discrepancy through two developments, based on real-space studies of colloids using confocal microscopy. First, we consider the nucleation barrier by measuring the free energy of formation of pre-critical nuclei, whose occurrence frequency is high enough to be experimentally accessible using confocal microscopy. Second, we aim to map state points between experiment and simulation with previously unmatched precision. To do this, we improve particle tracking using recently developed methods integrating machine learning, and we employ higher-order correlation functions, which are more sensitive to volume fraction than pair correlation functions. With our method, the nucleation barriers show reasonable agreement, leading to the disappearance of the discrepancy. Moreover, from confocal microscopy data of sedimenting samples, we found that the competing time scales of sedimentation and crystallization in experiments based on the Paulin-Ackerson method-commonly used to determine the state point in light scattering experiments-could lead to a systematic overestimation of the volume fraction, and thus to the appearance of the discrepancy. Finally, we study crystal nucleation in another model system: dipolar colloids, in which dipolar interactions are induced by an external electric field. The electric field can be used to easily tune the strength of the dipolar interaction, allowing the study of polymorph selection and Ostwald's step rule. Particularly interesting here is the formation of a metastable hexagonal close-packed (HCP) crystal. This then melts, after which a BCT (the stable phase) crystal forms. The underlying mechanisms and the connection with the structure of the fluid are currently under investigation. Additionally, the possibilities for optimizing crystal nucleation in dipolar systems are analysed by applying different protocols for the dipolar interaction strength. We find that certain protocols promote faster assembly of larger crystalline domains.

KEYWORDS

Condensed matter, Colloids, Nucleation